UNIVERSITY OF COPENHAGEN
FACULTY OF SCIENCE

TU Graz

Nanna Bach-Møller, BSc BSc cand.scient.

Exoplanet atmospheres in high-energy radiative environments

DOCTORAL THESIS
to achieve the university degree of
Doktor der Naturwissenschaften at Graz University of Technology
and
Doctor of Philosophy at University of Copenhagen

submitted to
Graz University of Technology
and
PhD School of the Faculty of Science, University of Copenhagen

Supervisors
Univ.-Prof. Dr.rer.nat. Christiane Helling,
Institute of Theoretical and Computational Physics, Graz University of Technology
and
Prof. Uffe Gråe Jørgensen
Niels Bohr Institute, Faculty of Science, University of Copenhagen

Graz, June 2024

Abstract

Exoplanets are found in a multitude of different environments resulting in a widely different influx of high-energy radiation on the planets. High-energy radiation such as X-ray and UV radiation (XUV), stellar energetic particles (SEP), and galactic cosmic rays (GCR) are known to impact planet atmospheres through processes such as photochemical reactions, ionization, heating, and ion-induced nucleation of cloud particles. In order to understand our observations of exoplanet atmospheres we therefore need to understand how the radiative environment of a planet might affect its atmosphere.

The first part of this project aims to explore how high-energy radiation affects the aggregation and charging of mineral cloud particles.
We present experiments conducted in an atmosphere chamber on SiO_2 particles. The particles were exposed to gamma radiation under varying humidity. The aggregation and charging state of the particles were studied with a Scanning Mobility Particle Sizer.
We find that the SiO_2 particles cluster to form larger aggregates, and that this aggregation is inhibited by gamma radiation. We find that gamma radiation shifts the charging of the particles to become more negative, by increasing the charging state of negatively charged particles. We find these trends to be present in both low- and high-humidity environments.
We suggest that the overall effect of gamma radiation could favor the formation of a high number of small particles over a lower number of larger particles.

The second part of this project aims to explore how the high-energy radiative environment affects the complex chemistry of exoplanet atmospheres.
We present a series of models run for the disequilibrium chemistry of close-in gas giants using a 1D photo-chemistry and diffusion code in conjunction with a chemical kinetic network. The input radiation was varied for (1) XUV radiation

representative of seven different main-sequence host stars (M- to O-type), (2) SEP representative for M-, K-, and G-type host star, and (3) GCR representative of different galactic environments.
We find that XUV radiation is the most important type of high-energy radiation for determining the relative concentration of most atmospheric species. We find that SEP and GCR can significantly impact the concentration of hydrocarbons (for SEP) and ions (for both) in the deeper atmospheres (from $\sim 10^{-3}$ to 10^{-5} bar and $> 10^{-1}$ bar respectively). In a case study on the warm-Saturn HATS-6b orbiting an M-dwarf host, we find that SEP can significantly impact observationally interesting species such as CH_4 and HCN.
We intend to continue our study on radiative environments by identifying observable molecular tracers for the different types of high-energy radiation.

In summary, we find that high-energy radiation can affect cloud formation and the chemical composition of an atmosphere, including the concentrations of observationally interesting species. This highlights the importance of considering high-energy radiation in our analysis of atmosphere observations.

Resumé

Exoplaneter findes i et utal af forskellige miljøer hvilket medfører store forskelle i deres influks a højenergistråling. Det vides at højenergistråling såsom X-ray og UV stråling, stellare energiske partikler (SEP), og galaktisk kosmisk stråling (GCR) kan påvirke planetatmosfærer igennem processer såsom fotokemiske processer, ionisering, opvarmning, og ion-induceret dannelse af skypartikler. For at forstå vores observationer af exoplanetatmosfærer bliver vi derfor nødt til at forstå hvordan strålingsmiljøet kan påvirke en planets atmosfære.

Den første del af dette projekt har til formål at undersøge, hvordan højenergistråling påvirker aggregeringen og ladningen af minerale skypartikler.
Vi præsenterer eksperimenter udført i et atmosfærekammer på SiO_2 partikler. Partiklerne blev udsat for gammastråling under varierende luftfugtighed. Partiklernes aggregerings- og ladetilstand blev undersøgt med en Scanning Mobility Particle Sizer.
Vi finder frem til, at SiO_2-partiklerne sætter sig sammen og danner større aggregater, og at denne aggregering hæmmes af gammastråling. Vi finder frem til, at gammastråling gør partiklernes ladning mere negativ ved at forøge ladetilstanden af negativt ladede partikler. Vi finder at disse tendenser gør sig gældende i miljøer med både lav og høj luftfugtighed.
Vi tror, at den samlede effekt af gammastråling muligvis favorisere dannelsen af et højt antal små partikler frem for et lavere antal større partikler.

Den anden del af dette projekt har til formål at udforske, hvordan det højenergetiske strålingsmiljø påvirker den komplekse atmosfærekemi på exoplaneter.
Vi præsenterer en serie af modeller over uligevægtskemien af gas-planeter der er simuleret ved hjælp af en 1D fotokemi- og diffusionskode i kombination med et kemiske kinetiske netværk. Bestrålingen af planeten blev varieret for (1) XUV-stråling, der repræsenterer syv forskellige værtsstjerner i hovedserien (M- til O-

type), (2) SEP, der repræsenterer værtstjerner af M-, K- og G-typen, og (3) GCR, der repræsenterer forskellige galaktiske miljøer.
Vi finder, at XUV-stråling er den type højenergi-stråling der har den største indflydense på den relative koncentration af de fleste atmosfæriske molekyler. Vi finder frem til, at SEP og GCR kan påvirke koncentrationen af kulbrinter (for SEP) og ioner (for begge) især i de dybere lag af atmosfæren (fra $\sim 10^{-3}$ til 10^{-5} bar og $> 10^{-1}$ bar henholdsvis). I et case-study af den varme-Saturn, HATS-6b, der kredser om en M-dværg stjerner, finder vi frem til, at SEP kan have en markant inflydelse på potnetielt observerbare molekyler, såsom CH_4 og HCN.
Vi planlægger at fortsætte vores undersøgelse af strålingsmiljøer ved at identificere observerbare molekyler der kan agere som indikatorer for de forskellige typer højenergistråling.

Kort fortalt finder vi, at højenergistråling kan påvirke skydannelse og den kemiske sammensætning af en atmosfære, herunder også koncentrationerne af observerbare molekyler. Dette understreger vigtigheden af at overveje højenergistråling når vi analyserer atmosfæreobservationer.

Zusammenfassung

Exoplaneten können in vielen verschiedenen Strahlungsumgebungen gefunden werden, mit unterschiedlichem Einfluss von hochenergetischer Strahlung auf diese Planeten. Hochenergetische Strahlungen wie zum Beispiel Röntgen- und UV-Strahlung (XUV), stellar energetische Teilchen (SEP) und galaktische kosmische Strahlung (GCR) können die Atmosphären von Planeten mittels Prozessen wie zum Beispiel, photochemische Reaktionen, Ionisation, Erhitzung und Ionen induzierte Nukleation von Wolkenteilchen, beeinflussen. Um unsere Beobachtungen von Atmosphären von Exoplaneten zu verstehen, müssen wir somit verstehen, welchen Einfluss die Strahlungsumgebung auf die Atmosphären dieser Exoplaneten hat.

Der erste Teil dieses Projekts untersucht, wie hochenergetische Strahlung die Aggregation und das Aufladen von mineralischen Wolkenteilchen beeinflusst.
Wir präsentieren die Resultate von Experimenten, welche in einer Atmosphärenkammer an SiO2 Teilchen durchgeführt wurden. Diese Teilchen wurden Gammastrahlung, unter verschiedenen Luftfeuchtigkeitsbedingungen, ausgesetzt. Die Aggregation und der Ladezustand der Teilchen wurden mit einem Scanning Mobility Particle Sizer (SMPS) untersucht.
Wir zeigen, dass die SiO2 Teilchen sich in größeren Aggregaten anhäufen und dass die Gammastrahlung diese Aggregation inhibiert. Wir zeigen, dass die Gammastrahlung den Aufladeprozess der Teilchen verändert und diese Teilchen negativer auflädt, indem sie den Ladezustand der negativen Teilchen erhöht. Diese Trends können sowohl in Messungen mit niedriger als auch hoher Luftfeuchtigkeit gefunden werden.
Wir postulieren, dass der Einfluss von Gammastrahlung zu einer Bildung von mehreren, kleineren Teilchen führen könnte, verglichen mit einer Bildung von wenigen, größeren Teilchen.

Der zweite Teil dieses Projekts untersucht den Einfluss von hochenergetischen

Strahlungsumgebungen auf die Chemie innerhalb der Atmosphären von Exoplaneten.
Wir präsentieren eine Reihe an Simulationen der Ungleichgewichtschemie von Gasgiganten, welche mittels einer Kombination von einem 1D Photochemie und Diffusionscode mit einem kinetischen chemischen Ratennetzwerk, erstellt worden. Die Eingangsstrahlung wurde auf mehrere Weisen variiert, die XUV Strahlung wurde so variiert, dass sie sieben verschiedene Hauptreihensterne (M- bis O-Sterne) repräsentiert, die SEP Strahlung wurde so variiert, dass sie M-, K- und G-Sterne repräsentiert und die GCR Strahlung repräsentiert verschiedene galaktische Umgebungen.
Wir zeigen, dass die XUV Strahlung der wichtigste Strahlungstyp unter den hochenergetischen Strahlungen ist, um die relative Konzentration der meisten chemischen Spezies in der Atmosphäre zu bestimmen. Wir zeigen, dass die SEP und GCR Strahlung starken Einfluss auf die Konzentration von Kohlenwasserstoffen (SEP) und Ionen (SEP und GCR) in tieferen Atmosphärenschichten hat (von ca. $\sim 10^{-3}$ bis 10^{-5} bar für Kohlenwasserstoffe und $> 10^{-1}$ bar für Ionen). In einer Fallstudie des Saturn ähnlichen Planeten HATS-6b, welcher einen M-Zwerg umkreist, zeigen wir, dass die SEP Strahlung einen starken Einfluss auf die für Beobachtungen interessanten chemischen Spezies wie zum Beispiel CH_4 und HCN hat.
Wir wollen unsere Studien von Strahlungsumgebungen fortsetzen, indem wir molekulare Tracer für verschieden hochenergetische Strahlungsumgebungen finden wollen.

Zusammenfassend können wir sagen, dass hochenergetische Strahlung die Wolkenbildung und die chemische Zusammenstellung von Atmosphären beeinflusst. Dies gilt insbesondere auch für chemische Spezies, welche für astronomische Beobachtungen interessant sind. Dies zeigt, wie wichtig es ist, hochenergetische Strahlung in der Analyse von Beobachtungen von Atmosphären zu berücksichtigen.

Acknowledgements

Doing a PhD is hard, and it is sometimes hard in ways I had not predicted going into it. I honestly do not think I could have done even half of this without the support from the lovely people around me, and you all deserve my gratitude.

To my family. You have given me a curiosity of the world and shown me that I can do anything I put my mind to, even if that is to look for dragons in space. You are, without a doubt, the best family anyone could ever wish for. Thank you so much for creating an environment where I *always* know that I am loved and supported. You all mean so incredibly much to me and I have missed you horribly.

Frederik, min engel. Thank you for always being an amazing person and partner. Thank you for loving me through this chaos I have put the both of us through and for telling me when I'm an idiot to others or to myself. I love you.

To Sidse, Mads, Jacilyn, and Andrew. I feel so lucky to have you in my life. Thank you for always being there with me despite the distances, and for sharing the ups and downs. I look forward to all of the wonderful experiences we will have together in the future.

To my supervisors. Uffe, you have been such an important part of my journey in astrophysics, and I cannot thank you enough for taking me under your wing. Martin, it has been absolutely lovely working with you. Thank you for your guidance and patience in letting me mess with your lab, and for checking in on me whenever you knew I was struggling. Christiane, thank you for giving me this opportunity and for always being willing to listen even when we disagreed.

To the ESRs of the CHAMELEON network. Thank you for just being an awesome group of people. It's been a pleasure working with you, and I'm excited to follow all the great things you are gonna achieve in the future.

To all of the lovely people at IWF and UCPH. Thank you so much for all the times we have shared with laughs, and cake, and dinners, and drinks. In an environment where everyone was busy, you always found time for each other. I feel lucky to have spent the past few years with you. Especially thank you to Patrick and Nidhi for all the help you have given me and for answering my endless questions, and to Thorsten for being a huge support when I first arrived in Graz and for translating my abstract.

Helena, Domling, Baby David, JP, Sven. I don't even know where to start. Thank you so so much for making my time in Graz something I will look back on fondly. Thank you for having the weirdest conversations with me, and drinking tea on my couch, and hiding stuff in my office, and scaring the shit out of me on a regular basis. Thank you for being there for me when things were hard, and when it was Tuesday and the week had been long, and when I decided to explode one of my organs. Just thank you. I honestly don't know what to do without you moving forward. May you always wear red, speak your beautiful minds, and tell stupid inappropriate jokes.

Many of the topics in this work were entirely new to me, and it has often been necessary for me to reach out to ask for help. In doing so it has been a pleasure to experience how kind, helpful, and patient people have been! I would like to thank Dr. Luca Fossati for his extreme patience in explaining stellar winds to me, and Prof. Dr. Astrid Veronig for making me realize that I can't actually use stellar winds in my work. I would like to thank Prof. Lidia Oskinova (Potsdam University) for her guidance on spectra, and for providing an X-ray spectrum of an O-type star, and Dr. Fernando Cruz Aguirre for sharing his SED of an F-type star with me.

Finally, a thank you to my assessment committee; Prof. Birgitta Schultze-Bernhardt, Prof. Jes Jørgensen, and Prof. Liv Hornekær. I hope you will enjoy reading my thesis, and I look forward to hearing your thoughts on it!

Funding

Nanna Bach-Møller is part of the CHAMELEON MC ITN which received funding from the European Union's Horizon 2020 research and innovation programme under the Marie Sklodowska-Curie grant agreement no. 860470.

Publications

Published work included in this thesis

Nanna Bach-Møller, Christiane Helling, Uffe G. Jørgensen, Martin B. Enghoff
Aggregation and charging of mineral cloud particles under high-energy irradiation
Published by the American Astronomical Society, 8th of February 2024
Bach-Møller et al. (2024)

Pre-published work included in this thesis

Sven Kiefer, **Nanna Bach-Møller**, David A. Lewis, Dominic Samra, Aaron D. Schneider, Flavia Amadio, Helena Lecoq-Molinos, Ludmila Carone, Leen Decin, Uffe G. Jørgensen, Christiane Helling
Under the magnifying glass: A combined 3D model applied to cloudy warm Saturn type exoplanets around M-dwarfs
Submitted to Astronomy and Astrophysics, 17th of June 2024
Kiefer et al. (2024)

Work not included in this thesis

The list below shows publications I co-author through my involvement with the MiNDSTEp consortium where I have participated in microlensing and transit observations.

- Satoh, Y. K., Koshimoto, N., Bennett, D. P., Sumi, T., Rattenbury, N. J., Suzuki, D., ... & MiNDSTEp Collaboration. (2023). *OGLE-2019-BLG-0825: Constraints on the Source System and Effect on Binary-lens Parameters Arising from a Five-day Xallarap Effect in a Candidate Planetary Microlensing Event*. The Astronomical Journal
- Kelley, M. S., Farnham, T. L., Li, J. Y., Bodewits, D., Snodgrass, C., Allen, J., ... & MiNDSTEp Collaboration. (2021). *Six outbursts of comet 46P/Wirtanen*. The Planetary Science Journal
- Southworth, J., Barker, A. J., Hinse, T. C., Jongen, Y., Dominik, M., Jørgensen, U. G., ... (2022). *A search for transit timing variations in the HATS-18 planetary system*. Monthly Notices of the Royal Astronomical Society
- Herald, A., Udalski, A., Bozza, V., Rota, P., Bond, I. A., Yee, J. C., ... & MiNDSTEp Consortium (2022). *Precision measurement of a brown dwarf mass in a binary system in the microlensing event-OGLE-2019-BLG-0033/MOA-2019-BLG-035*. Astronomy & Astrophysics

Contents

1

Introduction

- on exoplanets and radiative environments

"This space we declare to be infinite; since neither reason, convenience, possibility, sense-perception nor nature assign to it a limit. In it are an infinity of worlds of the same kind as our own"
– Giordano Bruno, 1584

For as long as we know, humans have suspected the existence of other worlds among the stars. One of the first recordings of this suspicion can be found in the book *De l'infinito universo e mondi* (On the Infinite Universe and Worlds) by the Italian philosopher and astronomer Giordano Bruno from 1584 Maor (2013). Bruno was a supporter of the, then novel, Copernican model that stated that the sun did not revolve around the Earth, as previously believed, but rather that the Earth and the other planets of the Solar System revolve around the Sun. Bruno took this notion one step further and proposed that our Sun might just be one of the infinity of stars in space, and that each of these stars might have their own planets revolving around them, forming systems similar to the Solar System.

Today, these planets are known as *exoplanets*.

You would think that having 400 years to get used to the thought would have prepared the scientific community for the first exoplanet observation in 1992. But despite countless theories and multiple suspected previous observations, the observation of two planets around the star PSR B1257+12 still came as a shock. Not because of the planets, but because of the environment they were found in. PSR B1257+12 is a pulsar; an extremely energetic and rapidly rotating neutron star, that is formed when the core of a massive star collapses during a supernova. When scientists had speculated about exoplanets, they had envisioned planetary systems very similar to the Solar System, but already from this first discovery it was clear that planets might be found in environments distinctly different from ours.

This chapter provides an introduction to the topic of exoplanets and some of the environments they can be found in. We especially focus on the different types of high-energy radiation found in the environment, and how these can affect the chemistry of exoplanet atmospheres. Sec. 1.1 describes the diversity of exoplanets, and how they differ from the Solar System planets. Sec. 1.2 describes exoplanet atmospheres, how they can be observed and modelled, and some of the important processes taking place. Sec. 1.3 describes the high-energy environments of exoplanets especially focusing on the XUV radiation and energetic particles of their host stars, as well as the galactic cosmic rays from outside the systems. Sec. 1.4 reviews some of the previous studies done on the effect of high-energy radiation on exoplanet atmospheres. And finally, Sec. 1.5 describes the aim of this thesis and which research questions we have centered our work around, as well as the general layout of the thesis.

Declaration: Section 1.2.3 on cloud formation is adapted from the publication Bach-Møller et al. (2024), titled "*Aggregation and charging of mineral cloud particles under high-energy irradiation*". I (author) am the first author on this publication and the text included in Sec. 1.2.3 is written by me.

1.1 Exoplanets

Exoplanet research has evolved in the 30 years since the first discovery, and now more than 6800* planets have been discovered, many of them in systems quite

*`https://exoplanet.eu/` accessed 08.07.2024

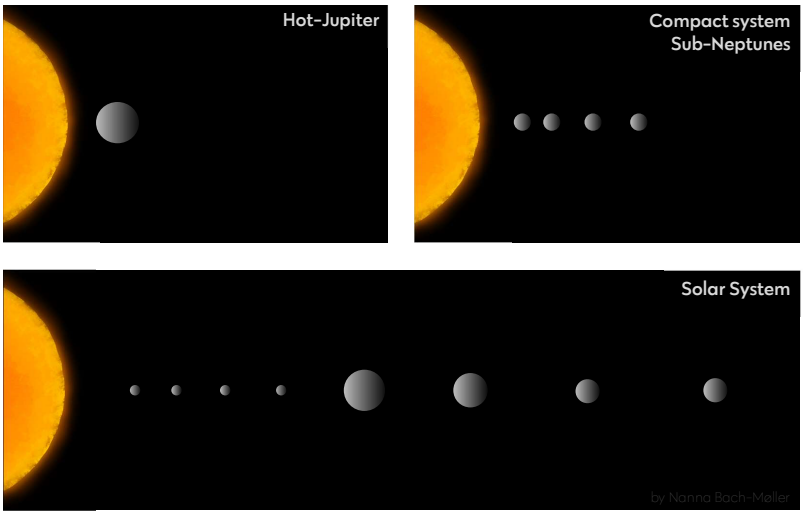

Figure 1.1: Illustration of some of the different types of planetary systems described in the text. Sizes and distances not to scale. Made by author.

different from ours.

We now recognize some of the characteristic features of the Solar System. The Solar System has a main sequence G-type star. This means we have a relatively calm medium-sized star with a long life-span, which we will get into more detail about in Sec. 1.3.1. We have eight planets, that all have almost circular orbits, and semi-major axes of $\sim$0.5 to 30 AU. We have four small terrestrial planets in the inner Solar System, and four larger gas giants in the outer Solar System. The Solar System is currently located in one of the galaxy's spiral arms, $\sim$8kpc from the galactic center, where we are moving through a cloud of warm low-density gas (the Local Interstellar Cloud) inside a bubble with even lower density (the Local Bubble).

Exoplanets have been discovered around a wide range of main sequence host stars, from the dim, flaring M-dwarfs to the bright, hot B-type stars (Janson et al., 2021). We have found both terrestrial planets and gas giants similar to those in the Solar System, but we have also found planet types that are not found in the Solar System, and the systems often have very different constellations from what we are used to.

Hot-Jupiters

Most of the early detections were of a planet type we do not have in the Solar System: Hot-Jupiters. Hot-Jupiters are gas giants that orbit extremely close to their stars, often with periods of hours to days (Dawson & Johnson, 2018), and often as the only planet we have discovered in their system. The close proximity to the star can heat these planets up to a few 1000 K, and due to the gravity of the host star many hot-Jupiters are tidally locked, with one side always facing the star (the day-side or substellar point) and the other side always facing away (the night-side or antistellar point). As we will see in later chapters this extreme difference in irradiation of each side of the planet can lead to a dichotomy in the chemistry of the atmospheres, where the substellar point is highly ionized and cloud free while the antistellar point might be cool enough to allow for complex molecules and clouds to form (e.g. Helling et al. (2019a, 2021)). In many cases these temperature differences can also drive extreme weather patterns with strong zonal jets forming along the equator (e.g. Baeyens et al. (2021)).
As mentioned, one of the characteristics of the Solar System is the distribution of smaller planets in the inner system, and larger planets further out, and hence we have no close-in gas giants. It is yet uncertain exactly how common hot-Jupiters are (Yee et al., 2021) since we are aware that many of our detection methods are strongly biased for hot-Jupiters.

Detection methods

When we observe exoplanets we mainly do so by observing the radiation coming from their host star. This is necessary because planets are only a fraction of the size of their host star, and since planets do not have fusion in their cores they do not emit the same amounts of radiation as stars. In most cases, it is therefore impossible for our instruments to isolate the radiation from a planet from that of its host star.
Currently, the two primary methods for detecting exoplanets are the Radial Velocity (RV) method and the Transit method.

The RV method detects exoplanets based on the pull they have on their host stars. When a planet orbits its host star, in fact, they both orbit a common center of mass, and the star therefore moves slightly back and forth in tune with the planet. This movement can be detected as a Doppler shift in the radiation from the star, and the mass and period of the planet can be determined from this Doppler shift.

Since the gravity of the planet will strongly influence the movement of the star, it is much easier to detect close-in giant planets, than smaller planets or planets further out.

The Transit method is the most successful detection method so far, and utilizes the shadow a planet casts toward us as it moves in front of its star. When observing the radiation of a host star, the presence of a planet in our line of sight will cause a dip in the light curve observed from the star. From this dip, or *transit*, the size and period of the planet can be determined. Since the depth of the transit will depend on the size of the planet, and we need multiple observations of the transit to verify the detection, larger planets and planets that transit more often due to the smaller orbit are easier to detect and verify.

General population

As a result of these detection biases, the fraction of hot-Jupiters in the observed population of planets is not representative of the fraction of hot-Jupiters in the true planet population. As our detection methods have improved, a higher fraction of small planets and planets further out has been revealed, and we now believe that only $\sim$ 0.4 % of FGK stars (see Sec. 1.3.1) host hot-Jupiters (Yee et al., 2021), making them a rare breed. Instead other planets and systems have proven to be abundant.

The most common type of planet observed are the so-called sub-Neptunes, and these are also planets that are not found in the Solar System. Sub-Neptunes are of a size between Earth and Neptune, and $>$ 50 % of G-type stars are expected to host Sub-Neptunes (reviewed in Bean et al. (2021)). Sub-Neptunes can be separated into two categories: mini-Neptunes that have a radii of > 2 $R_\oplus$ and super-Earth that have a radii of < 1.5 $R_\oplus$. The exact formation path of these two categories is yet unknown, but it is expected that they are both Earth-like in their composition, but while the mini-Neptunes have maintained the primary atmospheres of H and He (explained further in Sec. 1.2), the super-Earths have been stripped of their atmospheres by the radiation from the host star and energy in the planet core.

Where the Solar Systems has eight planets somewhat ordered by size, most exoplanet systems seem to be smaller, rarely with more than four planets, and seemingly with an average around 2.5 planets per system (Jurić & Tremaine, 2008; Bach-Møller & Jørgensen, 2020). The larger systems discovered, rarely follow the same size pattern as the Solar System, and many consist of planets all of the same

size, in very compact orbits (Weiss et al., 2022; Goldberg & Batygin, 2022), or they show an "anti-ordered" system, with the largest planets close to the star, and smaller planets further out (Mishra et al., 2021, 2023a,b). The final architecture of the system is believed to be decided by a combination between the mass and lifetime of the protoplanetary disk the planets are formed from, and interactions between the planets, causing them to migrate, collide, or be completely ejected from the system (Mishra et al., 2023b).

1.2 Exoplanet atmospheres

When we observe planets directly, what we observe is usually their atmospheres, or in many cases, the outer part of the atmospheres. Atmospheres are gaseous layers at the boundary between an object such as a planet, moon, or star, and the surrounding space. Most larger objects in the Solar System have an atmosphere, and we expect the same to be true for exoplanet systems.

All planets are formed with an atmosphere mainly consisting of H and He from the protoplanetary disk and gas giants keep this primary atmosphere. If a planet is too small, however, its gravity will not be able to maintain molecules as small as H and He, so the primary atmosphere will be lost to space due to the radiation and wind from the host star. In many cases a new, secondary atmosphere will build up on the planet as heavier gasses such as H_2O, CO_2, and N_2 are released from the planetary mantle, as is the case for most of the terrestrial Solar System planets. The final composition of the atmosphere will depend on the local composition of the protoplanetary disk for gas giants, the composition and redox state of the mantle for terrestrial planets (Deng et al., 2020; Ortenzi et al., 2020), and on the physical and chemical processes of the atmosphere.

Even through observations rarely allow us to look deeper than the upper part of the atmosphere, they can still give us an insight into key information such as the current climate and energy balance, and the planet formation and evolution paths. Since a potential biosphere on the planet would most likely reside in its atmosphere, understanding the atmosphere is also crucial to evaluate a planets habitability and search for biosignatures.

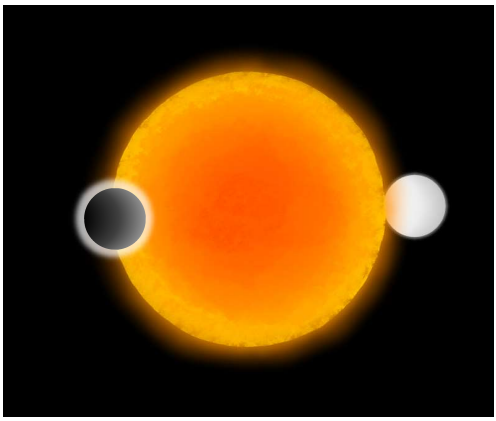

Figure 1.2: Illustration of a planet transiting its host star. On the left: Planet is passing in front of the star as observed from Earth (transit, primary eclipse). Light from the host star passes through the atmosphere of the planet. On the right: Planet is passing behind the star (secondary eclipse). Light from the host star is reflected from the atmosphere, and can be observed with the thermal emission from the planet. Made by author.

1.2.1 Atmosphere observations

Many atmospheres in the Solar System have been studied extensively either using telescopes or through direct measurements by space crafts. Exoplanet atmospheres are naturally more difficult to observe, and in many cases like the planets themselves, the atmospheres must be observed indirectly.

One of the main observation techniques for exoplanet atmospheres is **transmission spectroscopy**. Transmission spectroscopy is based on the transit method and uses the idea that the transit depth is wavelength dependent. By observing the planet as it passes in front of the star, we will see the light that passes through the atmosphere around the edge of the planet (see Fig. 1.2, left). Depending on which wavelength the planet is observed in, the atmosphere will be more or less opaque, and it will therefore appear smaller or larger. This is due to the fact that different atoms and molecules absorb light at different wavelengths, and the opacity of the atmosphere will therefore depend on its chemical composition. By observing a transit at a range of different wavelengths we can hereby create a transmission spectrum that will show absorption features for the atmospheric species. Since the atmosphere we observe is the edge of the planet disk, transmission spectroscopy will give us information about the so-called terminator regions, that make up the transition from the day side to the night side. For tidally locked planets these regions might be very different from the day- and night side, while for freely rotating planets such as the ones in the Solar System, the terminator regions can be representative for the entire planet.

A different approach is to observe the **emitted and reflected light** from a planet. This can be done when the planet is close to its second eclipse and moves behind the star (see Fig. 1.2, right). At this point we can observe the light that is emitted from the day side of the planet, as well as the radiation from the host star that is reflected from the planet. Since the radiation from the planet is observed together with the radiation from the host star, we need to compare the flux from the system during and just before the secondary eclipse to distinguish the contribution from the star and the planet. Since the light from the star will always be reflected from the day side of the planet and this side usually also has stronger emission these observations give us information about the day side of the planet.

Together, the transmission spectroscopy and emission/reflection observations can give us an insight into the composition of the atmosphere at different depths, its effective temperature and temperature profile, the albedo, and potential global variations. In order to interpret the observation, however, we need a thorough understanding of atmospheric structures and chemistry - an understanding we largely get through atmosphere modelling.

1.2.2 Atmosphere models

Atmosphere models reproduce the evolution or final state of an atmosphere based on numerical calculations of the known physical and chemical processes taking place. This is usually done by solving sets of ordinary and partial differential equations iteratively until the model has converged to describe a steady state solution for the atmosphere.
By modelling the physics and chemistry of the atmosphere we can reproduce the spectra of the modelled planet and compare it to actual observations (e.g. Mollière et al. (2019)). This not only gives us insight into the atmospheric processes, but also helps us analyze our observed spectra and interpret what they can tell us about the planet we are observing.

Atmosphere modelling is a constant compromise between accuracy and computational efficiency, and as such the strength and limitations of a model often lies in the approximations used during the computations.
One of the defining qualities of an atmosphere model is the number of dimensions it covers. Atmosphere models generally divide the atmospheres into units or boxes, in which the conditions are assumed to be homogeneous. These boxes

are either assumed to be isolated, or they can exchange gas, particles, or energy with the surroundings. The dimensions of the model are increased by stacking the units in one, two, or three directions.
1D models usually divide the atmosphere into units or layers stacked vertically through the atmospheric column. 1D models are especially suited to look at the effect of radiation at the top of the atmosphere through radiative transfer, ionization, or photochemistry, as well as the effect of surface interactions such as outgassing (e.g. Kasting et al. (1993); Kopparapu et al. (2013); Gustafsson et al. (2008)). These models also allow for the study of complex chemistry and they are often used for disequilibrium chemistry and cloud formation (e.g. Rimmer & Helling (2016a); Rimmer & Rugheimer (2019); Helling (2022); Samra et al. (2023)).
3D models, or general circulation models (GCMs), divide the atmosphere into a global grid based on longitude, latitude, and altitude. GCMs are especially suited to look at global dynamics and climate, as well as global variations in temperatures, winds, and chemistry (e.g. Schneider et al. (2022b); Carone et al. (2020); Mayne et al. (2014); Showman et al. (2009) or further examples in e.g. Wolf et al. (2019)). For planets with significant global variation, such as tidally locked planets GCMs can reproduce the day/night side differences as well as the transport between them. While GCMs are more accurate for modelling the planet as a whole, they are also very computationally heavy, and often better suited for modelling short-term processes than long-term evolution. GCMs are rarely used with complex processes such as disequilibrium chemistry and cloud formation (this is discussed further in Chapter 4 over Kiefer et al. (submitted 2024)).

Many physical processes of the atmosphere are driven by the effect of stellar radiation and transfer of energy. These processes are accounted for through the absorption, scattering, and emission of radiation, surface fluxes, radiative transfer and convection. In some cases complex processes like condensation, cloud formation, and lightning are also included. By simulating the physical processes we gain an insight into e.g. the temperature profiles and dynamics of the atmosphere.
The atmospheric chemistry is mainly driven by the temperature, pressure, and external radiation. The chemical composition can be modelled from an initial element composition either assuming equilibrium or disequilibrium chemistry. Assuming equilibrium is the least computationally heavy and can give a first approximation of the gas composition of the atmosphere based on the minimization of Gibbs Free energy (e.g. Woitke et al. (2018)). In most cases it will be more ac-

curate to assume the atmosphere to be in chemical disequilibrium, in which case and the chemical composition can be computed by running a chemical kinetics network (e.g. Rimmer & Helling (2016a); Tsai et al. (2017); Lee et al. (2023)). The network contains a list of chemical reactions with their respective reaction rates, and the final composition is found by running these reactions iteratively and following the evolution. Calculating the disequilibrium chemistry allows us to include processes such as photochemistry and ionization due to external radiation, or outgassing from the surface.

1.2.3 Cloud formation

One of the great advancement in exoplanet atmosphere research in recent years, is the recognition of the critical role cloud formation plays in the energy balance and chemistry of atmospheres. Exoplanets, as well as many Solar System objects, display a wide variety of cloud particles that differ greatly from the cloud formation observed on Earth. In addition to the various water, ammonia, and condensed hydrocarbon clouds, that are among the many cloud types observed in the atmospheres of Solar System objects (e.g. Baines et al. (2009); Brooke et al. (1998); Brown et al. (2002); Gao et al. (2021); Ohno et al. (2021); Rages & Pollack (1992); Romani & Atreya (1988); Sagan et al. (1992); Sromovsky et al. (2011); Wong et al. (2017)), studies predict a wide range of mineral clouds in warmer exoplanet atmospheres (e.g. Gao et al. (2021); Helling (2020, 2022); Marley et al. (1999); Seager & Sasselov (2000)), which is believed to greatly influence our observations of these planets (Gao et al., 2021; Helling, 2022).

Cloud particles are formed through the condensation of supersaturated gas onto a seed particle also known as a *cloud condensation nuclei* (CCN). On terrestrial planets, such as Earth, CCNs can been ejected directly from the surface through e.g. sandstorms, volcanic eruptions, or as spray from surface oceans Helling (2019). Alternatively CNN can be formed directly from the gas phase through nucleation, which makes up for $\sim$ 45 % of CNN on Earth (Merikanto et al., 2009), and is the sole source of CNN for gas giants. Nucleation describes the gas-to-particle transition where gas molecules form clusters that grow to become solid particles. Studies have found that nucleation can take place for a number of species such as H_2SO_4 (Svensmark et al., 2013), titanium oxides such as TiO_2 (e.g. Sindel et al. (2022)), silicon oxides such as SiO (Bromley et al., 2016), vanadium oxides (Lecoq-Molinos et al., 2024), and a number of other metal oxides (see reviews in Sindel et al. (2022); Lecoq-Molinos et al. (2024)).

1.3 Exoplanet environments

The exoplanets and their systems are not the only factors that differ from the Solar System, also the radiative environments surrounding the planets differ. The radiative environment of a planet is primarily determined by two factors: radiation from the host star and external radiation from outside the system. In this section I will describe these two factors, especially focusing on high-energy radiation; the topic of this thesis.

1.3.1 Host stars

A planetary system is born when a molecular cloud collapses due to gravity to form a protoplanetary disk. As gas and dust accretes onto the center of the disk a protostar is formed, while smaller perturbations further out in the disk initiate the formation of the planets.
At some point the protostar can accrete enough material that the gravitational pressure heats up the core to temperatures of 10^7 K. At these temperature, fusion of H to ^{2}H and He can begin, and the newly formed star enters the main-sequence where it will spend most of its lifetime, until the core runs out of H and the star will enter the final stages of its evolution.

Main sequence stars are distributed into seven categories depending on their mass, temperatures and spectral features. These categories are shown in Fig. 1.3.

As can be seen from Fig. 1.3 the effective temperatures of main sequence stars vary from 2000 K for the red dwarf stars to $\sim$ 60,000 K for the hot O-type stars. The temperature is determined by the amount of energy produced in the core, and since a higher mass leads to a higher internal pressure which in turn increases the fusion processes, we get a correlation between the stellar mass and temperature. The temperature of the star is directly reflected in its electromagnetic radiation thereby its color. The majority of a stars electromagnetic radiation is emitted from the stellar photosphere (see Fig. 1.4) that has been heated to the effective temperature. This radiation can be described as a blackbody that is characterized by a temperature-dependent energy distribution. As the energy distribution is shifted towards shorter wavelengths for higher temperatures, we see a shift towards blue for the hot, high-mass stars, while the cool low-mass stars (the M-dwarfs or red dwarfs) are red.

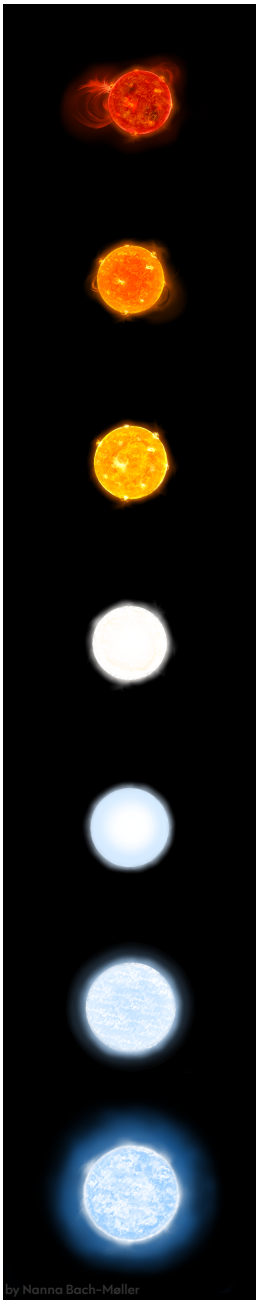

M-dwarf	T = 2000 K - 3500 K M < 0.6 $M_\odot$ $t_{MS} \approx 10^{11}$ yr	Cool, low-mass stars with high activity. ~ 76 % of all MS stars
K-dwarf	T = 3500 K - 5000 K M ≈ 0.6 - 0.9 $M_\odot$ $t_{MS} \approx 0.5 \cdot 10^{11}$ yr	Medium-small stars with magnetic activity. ~ 12 % of all MS stars
G-type	T = 5000 K - 6000 K M ≈ 0.9 - 1.1 $M_\odot$ $t_{MS} \approx 10^{10}$ yr	Solar-like stars. Medium size, active. ~ 8 % of all MS stars
F-type	T = 6000 K - 7500 K M ≈ 1.1 - 1.6 $M_\odot$ $t_{MS} \approx 0.5 \cdot 10^{10}$ yr	Medium size stars with low activity. ~ 3 % of all MS stars
A-type	T = 7500 K - 10,000 K M ≈ 1.6 - 3.0 $M_\odot$ $t_{MS} \approx 10^{9}$ yr	High-mass stars with no magnatic activity. ~ 0.6 % of all MS stars
B-type	T = 10,000 K - 30,000 K M ≈ 3.0 - 18 $M_\odot$ $t_{MS} \approx 10^{8}$ yr	High-mass stars with no magnatic activity. ~ 0.13 % of all MS stars
O-type	T = 30,000 K - 60,000 K M > 18 $M_\odot$ $t_{MS} \approx 10^{7}$ yr	Hot, massive stars with strong stellar winds. < 0.01 % of all MS stars

Figure 1.3: Types of main sequence stars, listed with their respective effective temperatures, radii, and life-time on the main sequence (t_{MS}). Illustration by author.

Convective zones and stellar activity

The mass is also the determining factor for the inner structure of the star, including the convective zones. The energy produced through fusion in the stellar core is transported through the envelope of the star until it reaches the surface and is released as radiation. Depending on the conditions, this energy transport happens primarily through either radiation or convection. Convection occurs in conditions where a parcel of gas moving up through the medium will continue to do so because the cooling of the parcel is slower than the cooling of the surrounding medium. These conditions are usually met in cooler and denser environments, or in environments with steep temperature gradients. In environments with smaller temperature gradients, such as many hotter stars, the energy transport will happen primarily through radiation.

In low-mass stars, the envelope surrounding the core have such low temperatures and high densities that the opacity becomes too high for the gas to be radiatively dominated. This means that the energy produced through fusion in the core cannot be transported through radiation alone, and convection will occur (reviewed by Maciel (2016)). For the smallest stars with $M < 0.2\ M_{\odot}$, the temperatures are low enough for this convective layer to reach all the way to the center of the star. For slightly larger stars, like the Sun, with $M \leqslant 1\ M_{\odot}$ the region around the core is hot enough to be radiative, but further out the temperatures cool enough for neutral H to be present which significantly increases the opacity, forming a deep convective envelope.
For more massive stars with $M > 1\ M_{\odot}$ the temperatures are high enough for H to be ionized and the envelope of the star remains radiative. At approximately the same mass threshold ($M > 1\ M_{\odot}$) the core becomes hot enough for the fusion of H to happen through the carbon-nitrogen-oxygen (CNO) cycle rather than the proton-proton (p-p) chain. In contrast to the p-p chain, the CNO is highly temperature-dependent and a steep temperature gradient is formed in the core, which causes the core to become convective. The size of this inner convective core will increase with the mass of the star, and for the stars of $20\ M_{\odot}$ the convective core can make up to 50% of the stellar mass.

Stellar convection can have an immense impact on exoplanet companions and on the system as a whole, through the formation of stellar magnetic fields. Studies have found that stellar magnetic fields are generated through turbulence in the outer convective zones of lower mass stars (reviewed by e.g. Berdyugina (2005)).

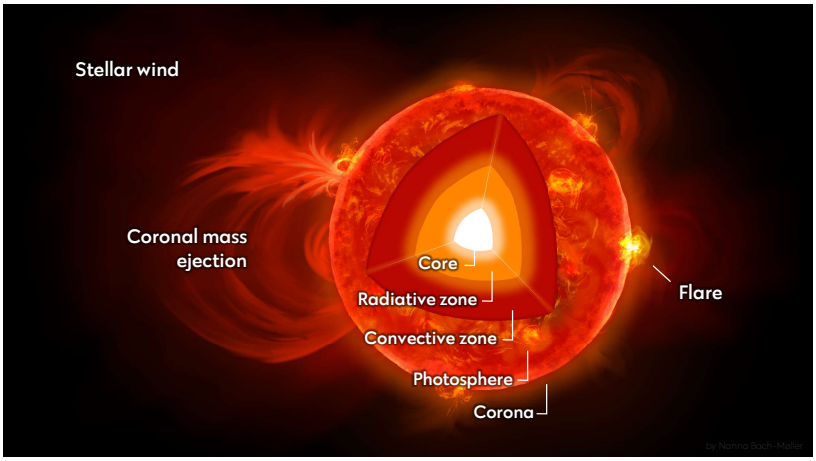

Figure 1.4: Illustration of internal structure and magnetic activity of M-dwarf star. Made by author.

Combining these magnetic fields with differential rotation causes the stars to become magnetically active, and leads to phenomenons such as stellar flares and coronal mass ejections (CMEs). Both flares and CMEs are eruptions in the stellar due to a build up of magnetic energy as magnetic fields explosively realign Reames (2020). In the case of flares, this heats up the corona, chromosphere, and photosphere to $> 10^7$ K, releasing a flash of radiation. In the case of CMEs the eruption of magnetic energy ejects large filaments of plasma from the corona and release them into space. In both cases this will lead to the release of high-energy radiation in the form of energetic particles (as will be described later) and photons in the XUV and X-ray regime emitted by the heated gas.

The correlation between rotation and magnetic activity was first suggested by Skumanich (1972) and has since been observed by numerous studies where the highest activities have been found for cool stars with rapid rotations (reviewed by Berdyugina (2005)). Among young stars we generally see higher rotation rates for high-mass compared to low-mass stars, but since the rotational damping is mass dependent, M- and K-dwarfs maintain their rotation for much longer than the massive stars (see review on stellar rotational evolution in (Bouvier et al., 2014)). Since both the existence of an outer convective zone and the long term rotation rate is mass dependent, the magnetic activity is also highly dependent on mass, with smaller stars generally having higher activities (e.g. Johnstone (2016); Berdyugina (2005); Astudillo-Defru et al. (2017)). The magnetic activity of younger stars is also generally higher due to their higher rotation rates.

Stellar models of intermediate-mass stars (F5- to B5-type stars) have found that the depth of the outer convective zone decreases with increasing effect temperatures, until it completely disappears at $T_{eff} \approx 8500$ K (the temperature of A-type stars) (e.g. Bohn (1984); Christensen-Dalsgaard & Aguirre (2018); Kupka & Montgomery (2002). This trend is supported by observations showing that very few massive stars are X-ray sources, indicating that these do not have flares and CMEs (as reviewed by Fossati et al. (2018) and Kowalski (2024)). Few signs of magnetic activity have been recorded for massive stars (F-B), and in these cases the activity is hypothesized to originate from a temporary "magnetic rejuvenation" caused by e.g. the star swallowing a planet or brown-dwarf companion, or the star passing through the Hertzsprung Gap as it leaves the main sequence (reviewed by Kowalski (2024)).

Electromagnetic radiation

As explained previously, the majority of the electromagnetic radiation observed from stars originates from the heated photosphere and can be described by a blackbody spectrum. This radiation is mainly dominating in the infrared, visible, and ultraviolet wavelength ranges. The far ultraviolet (FUV), extreme ultraviolet (XUV), and X-ray are dominated by radiation from the corona (see Fig. 1.4 and the chromosphere (thin layer between photosphere and corona). While the heating of the photosphere is directly related to the temperature, and thereby mass, of the star, the heating of the chromosphere and corona is less understood, but it has been found to be related to the magnetic field (reviewed in Johnstone (2016)).

While hot massive stars are strong sources in the longer wavelengths most of them are generally weak in the short wavelengths due to their lack of magnetic activity. The exception from this is the OB-type stars (O-stars and the most massive B-stars) that have long been known to emit X-ray radiation Seward et al. (1979); Harnden et al. (1979). The X-ray survey ROSAT All Sky Survey discovered a large number of OB-stars, marking these as X-ray sources, and X-ray emission is now believed to be an integral part of the stellar winds of OB-stars (see review in Oskinova et al. (2006)). Due to their extreme luminosity, stars with masses of $> M_{\odot}$ have strong radiatively-driven stellar winds Oskinova (2016) and perturbations in these hot stellar winds lead to the release of X-ray radiation independent of magnetic activity.

Stellar energetic particles

In addition to high-energy photons, magnetic activity also leads to the release of energetic particles. Stellar energetic particles (SEP), also known as stellar cosmic rays, are high-energy particles such as protons, electrons and heavier ions that have been accelerated from the surface of the star and are transported along the magnetic field lines into the surrounding system (Wild et al., 1963; Reames, 2013; Rodgers-Lee et al., 2020). SEP events can be divided into two categories depending on the process that accelerates the particles: 1) The gradual SEP events are caused by CMEs, where particles are accelerated by the shock front caused as plasma is ejected from the stellar corona (Zank et al., 2000; Li et al., 2012). Gradual SEP events release particles with energies of $>$1 GeV for a duration of $>$ 1 day and in the solar system they account for the majority of SEPs reaching Earth (e.g. Rodgers-Lee et al. (2021a)). 2) The impulsive SEP events are associated with stellar flares, where particles are believed to be accelerated in the region where magnetic re-connection takes place (e.g. Firoz et al. (2022)). Impulsive SEP events release particles with energies of $\sim$10 MeV (Kallenrode, 2003) for a duration of minutes to hours (e.g. Firoz et al. (2022); Doyle et al. (2018); Reep & Knizhnik (2019)) and while they result in lower particle fluxes than the gradual events, they are much more frequent.

The magnetic field events releasing SEP are some of the same events that heat up the corona to release X-ray, and SEP events have been found to correlate with X-ray flares. Herbst et al. (2019a) has studied this correlation for G-, K-, and M-dwarf stars and derived a peak size distribution that allows us to estimate SEP proton fluxes based on X-ray flare intensities. This will be further explored in Chapter 3.

Both the electromagnetic radiation, the stellar energetic particles, and the background stellar winds of the host star can significantly impact the atmospheres of surrounding exoplanets through photochemical reactions and inization. We will explore this impact in Sec. 1.4, but first we will look at our last source of high-energy radiation, the galactic cosmic rays, as well as how the exoplanet atmospheres are structured, modelled, and observed.

1.3.2 Galactic environment

The host stars are not the only source of high energy radiation, exoplanets are also irradiated by galactic cosmic rays (GCR) from outside the system. GCR are particles such as protons and He that have been accelerated through diffusive shock acceleration at supernova remnants (reviewed by Jasinski et al. (2020)). This acceleration brings the particles to energies of 1 to $\sim 10^8$ MeV (Patrignani et al., 2016; Bazilevskaya et al., 2008) and releases them into the interstellar medium (ISM). In addition to this, GCR of even higher energies are entering from outside the galaxy and observations of GCR in the Solar System indicate that their kinetic energy spectrum extends up to $\sim 10^{14}$ MeV Armillotta et al. (2022). It has been found the GCR in the solar system neighborhood form a homogeneous background or "sea" of GCR, and it is believed that this homogeneous GCR sea is the same throughout the entire outer galactic disk Strong et al. (2007) at galactocentric distances of > 8 kpc. This is due to the fact that the lifetime of the GCR accelerators is generally shorter than the GCR retention time in the ISM (Aharonian et al., 2020). The spectrum of this GCR sea is described by the Local Interstellar Spectrum (LIS) around the Solar System and has been measured by Voyager 1 and 2 (Cummings et al., 2016) as this mission left our heliosphere. The GCR flux spectrum for LIS can be seen in Fig. 1.5. In this comprehensive homogeneous sea the GCR density might vary on smaller scales, e.g. in close proximity to acceleration regions or giant molecular clouds (reviewed in Jasinski et al. (2020)), where especially the lower energy particles of $< 10^4$ MeV are affected. Within the galactocentric distances of 8 kpc (approximately corresponding to the Solar Systems location), the GCR density increases as the density of star forming regions and thereby accelerators increase (Guo & Yuan, 2018; Acero et al., 2016).

The amount of GCR reaching a planet is only partly decided by the GCR density of the galactic environment. The rest is determined by the modulation of the GCR through the astrosphere and magnetic field of the planet. The astrosphere (or heliosphere for the sun) is a "bubble" created by the stellar wind that encompasses the system and makes up the distinction between the system and the surrounding ISM. Magnetic fields from the star are transported with the stellar winds creating a magnetic field for the astrosphere itself (Herbst et al., 2022; Alfvén, 1942). As GCR encounter the astrosphere it is modulated through processes such as diffusion, convection, and adiabatic deceleration Ferreira & Potgieter (2004). This modulation breaks the GCR, thereby shielding the inner system

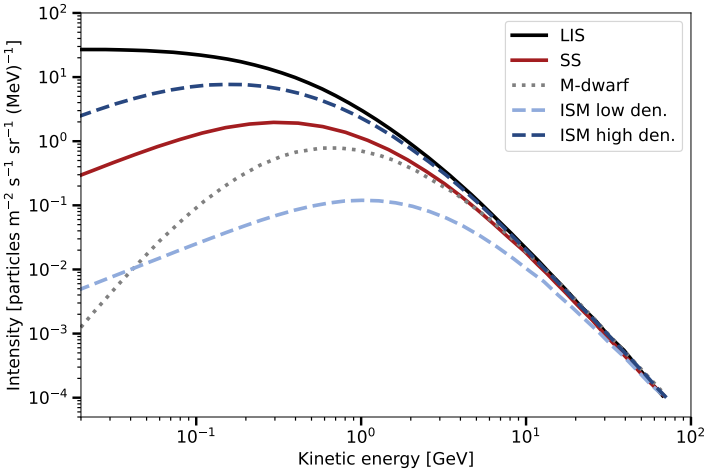

Figure 1.5: GCR proton fluxes at different locations. LIS: Local Interstellar Spectrum. SS: Flux at 1 AU in the Solar System. M-dwarf: Flux at 0.1 AU after modulation by the M-dwarf GJ411 Mesquita et al. (2021b). ISM low/high dens.: Flux at 1 AU after modulation my the solar system heliosphere that has extended into or been compressed by a different density ISM. The profiles for LIS, SS, and ISM low/high dens. are all obtained from Jasinski et al. (2020).

and the planets in it from the GCR irradiation. Since stronger stellar activity leads to stronger stellar winds (Vidotto et al., 2014), active low-mass stars will shield their system more from incoming GCR than the more massive inactive stars, and so does the strong winds of the OB-stars. The modulation of GCR through astrospheres has been extensively studied both for the evolving sun (e.g. Rodgers-Lee et al. (2020, 2021a); Svensmark (2006); Parker (1965); Jokipii (1971); Potgieter (2013), Sun-like stars Rodgers-Lee et al. (2021a,b), M-dwarfs (e.g. Herbst et al. (2020); Mesquita et al. (2021a,b); Sadovski et al. (2018)), and O-type stars (Sadovski et al., 2018; Scherer et al., 2015), and all find that stellar winds can significantly modulate GCR in all cases with especially the low-energy GCR being affected by this modulation. We will therefore generally see a lower influx of GCR in systems with magnetically active stars such as young stars and low-mass stars. When Herbst et al. (2020) modelled the modulation of GCR through M-dwarf systems a using 3D magnetohydrodynamic-based model they found that even for active systems, the GCR influx could be substantial, and they stress that the impact of GCR on exoplanets should not be neglected in the context of habitability. The GCR spectra for the Solar System at 1 AU Jasinski et al. (2020) and for the M-dwarf star GJ411 at 0.1 AU can be seen in Fig. 1.5.

The astrosphere is not only dependent on the activity of the host star, but also on the galactic environment. The size and shape of the astrosphere depends on the pressure balance between the stellar wind and the gas in the surrounding ISM. As mentioned earlier, the Solar System is located in the low-density "Local Interstellar Cloud", and if it was moved to a more high-density medium the heliosphere would be compressed, leading to less modulation of the GCR that would reach the planets. The effect of the ISM on GCR modulation has been studied by Jasinski et al. (2020). They look at the Solar System and two M-dwarf systems (Kepler-20 and Kepler-88), and model their GCR modulation in two galactic environments: a partially ionized warm ISM, and a dense gas similar to what 23 Ori resides in. They find that these differences in the ISM can change the size of the heliosphere from 26 AU to 402 AU, and that it can lead to differences in the GCR densities both for the Solar System and M-dwarf systems of > 2 orders of magnitude for GCR with energies of 10-100 MeV, and an order of magnitude for energies of 10^3 MeV. The GCR proton fluxes for the extended and contracted hemispheres are seen in Fig. 1.5.

A series of studies (Rodgers-Lee et al., 2020, 2021b,a; Mesquita et al., 2021a,b; Rodgers-Lee et al., 2023) has looked at the effect of SEP and GCR in planetary systems, how they are modulated through the astrosphere, and how they change over time. Rodgers-Lee et al. (2020) studied the GCR intensity of the evolving Earth using a 1D GCR transport model, and confirmed a lower intensity of GCR in systems with younger stars with higher rotation rates. Rodgers-Lee et al. (2021a) compared the influx of SEP and GCR for exoplanets around Sun-like stars during the stellar evolution. They found that despite the decrease in stellar activity over time, SEP energies remained dominant over GCR energies. Looking at other nearby systems around solar-type stars Rodgers-Lee et al. (2021b) find that they have similar or lower GCR fluxes in the habitable zone compared to the solar system, indicating that this might be a general trend in solar-like astrospheres. Mesquita et al. (2021a,b) model the propagation of GCR through the astrospheres of M-dwarfs and find that the low-energy GCR fluxes in the habitable zone of these systems are generally significantly lower than for the Solar System while the high-energy GCR fluxes are more comparable. Rodgers-Lee et al. (2023) modelled the energetic particle transport through the system of the M-dwarf star, GJ 436. They find that at the distances of 0.01 - 0.2 AU (where the planet GJ 436 b is located) SEP dominates the ionization in the atmosphere and peaks at $\sim 10^{-3}$ bar while GCR dominates locally in the lower atmosphere ($< 10^2$ bar). Further out in the sys-

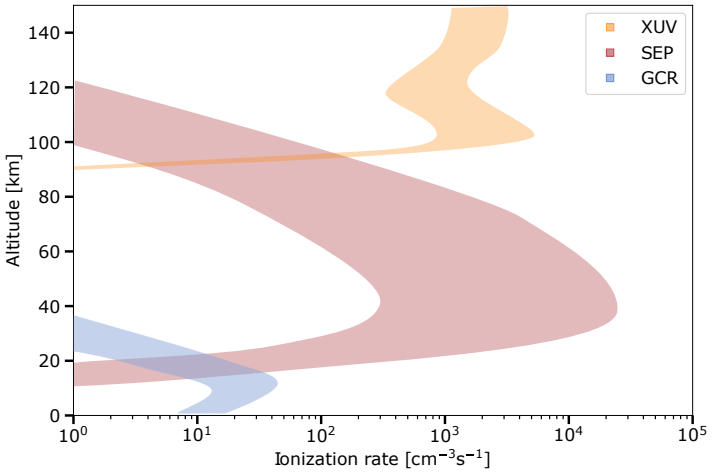

Figure 1.6: Ionization rates for XUV radiation, stellar energetic particles (SEP) and galactic cosmic rays (GCR) in Earth's atmosphere. Figure is modified from Mironova et al. (2015) and Baker et al. (2012)

tem, at 10 AU they find that the overall ionization from GCR equals that of SEP, indicating that the planets location in the system will affect its influx of energetic particles. Since exoplanets have been found in such a variety of environments, around all types of host stars and in many different parts of the galaxy, it is important for us to understand how these environments might affect them.

1.4 Effect of high-energy radiation on planetary atmospheres

High-energy particles have long been known to have a significant impact on Earth's atmosphere, where they affect e.g. the atmospheric chemistry, temperature, dynamics, cloud formation, and global electric circuit (see review in Mironova et al. (2015)). High-energy radiation is highly ionizing and different types of radiation dominate the ionization at different layers in the atmospheric column. Fig. 1.6 shows the ionization rates for XUV radiation, SEP, and GCR in Earth's atmosphere (the figure is adapted from Mironova et al. (2015)).

XUV radiation

As the figure shows, XUV radiation is the dominating ionization source in the upper atmosphere. While radiation at longer wavelengths, such as infrared and

visible, are the primary heat source in the deeper layers of the atmosphere, the shorter wavelengths of XUV radiation are absorbed in the upper atmosphere where they drive e.g. photochemical reactions and mass loss (e.g. Linsky (2014)). On Earth, XUV radiation is known to significantly affect the chemical composition of the atmosphere, and models predict a similar effect on exoplanets. XUV radiation at wavelengths below > 310 nm (and especially below > 170 nm) cause photodissociation of molecules such as H_2O, CO_2, and CH_4. These are all abundant and important molecules in the atmosphere, and their dissociation can lead to an increase in O (Linsky et al., 2014) and the highly reactive radical OH. Affecting these molecules can therefore have comprehensive effects on the chemistry of the atmosphere.

During the Early Release Science Program for the James Webb Space Telescope (JWST) (Stevenson et al., 2016; Bean et al., 2018), the hot-Jupiter WASP-39b was observed. The transmission spectrum of WASP-39b shows a clear absorption feature indicating the pretense of SO_2; an observation that could now be explained by atmospheric radiative–convective–thermochemical equilibrium models (Rustamkulov et al., 2023; Alderson et al., 2023). A follow-up investigation by Tsai et al. (2023) did a detailed study of the photochemistry of WASP-39b and found that the presence of SO_2 could be explained by photochemical reactions, and concluded that the sensitivity of SO_2 might make it suitable as a tracer of atmospheric properties. These studies underline the importance of XUV radiation and photochemistry in interpreting our observations.

One way to look at the effect of of XUV radiation on atmospheric chemistry is by producing grids of models over different host stellar types. Using a 1D model for thermal structures and photochemistry, Miguel & Kaltenegger (2013) modelled the disequilibrium chemistry of planets orbiting M, K, G, and F stars. They found that especially CH_4 and H_2O were sensitive to UV flux, and that H_2 was displaced with H as the most abundant gas species in the upper atmosphere for planets with high UV flux. A similar study was done by Baeyens et al. (2021, 2022), who combined a 3D GCM model with a pseudo-2D chemical kinetics code to build a grid of models for different effective temperatures (from 400 K to 2600 K) and different host stars of the types M, K, G, and F. Baeyens et al. (2022) found that photochemistry can significantly change the atmospheric composition and lead to the formation of important haze precursors such as HCN and C_2H_2. They note that the chemistry can be affected all the way down to pressures of several bar, and that

the products of photochemistry can be transported from the day side to the night side of tidally locked planets. Helling et al. (2023) build upon the grid by Baeyens et al. (2021) by combining profiles from their 3D GCM models with a kinetic cloud model to study the nucleation and evolution of cloud particles. They found that planets around K-dwarf hosts are generally faster rotators compared to planets around G-type stars, and that this rotation leads to larger cloud inhomogeneities. A study by Shulyak et al. (2020) looks at disequilibrium chemistry of a hot-Jupiter orbiting K, G, F, and A stars and find large changes in the mixing ratios of most chemical species orbiting the A-type host. They argue that these changes are due to the increased photochemistry induced by the strong XUV spectrum of A-stars.

High-energy radiation from the star can also lead to atmosphere loss, either due to an XUV driven expansion and heating of the thermosphere, due to photo-dissociation and subsequent H escape, or due to ionization and heating by the stellar wind (reviewed by e.g. Johnstone (2016)).

Stellar energetic particles

Deeper in Earth's atmosphere, below 100 km, SEP becomes the dominating source of ionization, (Fig. 1.6). As opposed to XUV radiation and GCR, SEP events are temporary and the SEP spectrum vary a lot: the range of SEP energies covers four orders of magnitude while the intensities covers eight orders of magnitude (Mironova et al., 2015). On Earth, SEP are known to increase the concentrations of NO_x in the upper atmosphere, that destroys O_3 as it is transported down to the ozone layer (Brasseur & Solomon, 2005). Studies have predicted that SEPs can also observably alter the climate and chemical composition of exoplanet atmospheres (e.g. Airapetian et al. (2020); Barth et al. (2021); Chadney et al. (2017); Venot et al. (2016); Herbst et al. (2023, 2019b)), and destroy potential ozone layers in Earth-like atmospheres (Segura et al., 2010). A study by Herbst et al. (2023) looked at the impact of SEP on planets in the M-dwarf system TRAPPIST-1. They found that strong SEP events could drastically increase the atmospheric ionization and cause substantial changes in the ion chemistry. When creating a synthetic spectrum for TRAPPIST-1e they found that SEP reduce the features for H_2O, CH_4, and O_3. Due to the importance of these molecules in biological processes, they stress that it is essential to include high-energy particles in atmosphere models to correctly asses biosignatures.

Galactic cosmic rays

At the lowest layers of Earth's atmosphere GCR dominates the ionization (Fig. 1.6). While the influx of GCR into the atmosphere is much lower than that of SEP, the energies of the particles are extremely high (up to 10^7 MeV compared to the $\sim 10^4$ MeV for SEP). When high-energy GCR enter into the atmosphere and collide with a nucleus of one of the gas atoms, it initiates a nuclear-electromagnetic-muon cascade (Mironova et al., 2015), that will propagate down the atmospheric column, and gradually increase the ionization, until it reaches a maximum in the lower atmosphere. A study by Rimmer & Helling (2013) on giant exoplanets and brown dwarfs found that the GCR ionization can extend all the way up to pressures of 10^{-4} bar, and that GCR can increase the ionization by more than three orders of magnitude in some parts of the atmosphere, indicating that GCR might play a significantly larger role for some exoplanets.

On Earth the GCR irradiation follows the solar activity cycle (Maurchev et al., 2024) as well as greater variations due to our location in the galaxy (Svensmark et al., 2021). Since low-energy GCR is modulated more by the stellar wind, the low-energy part of the GCR spectrum (10-500 MeV) varies significantly with the solar activity on tome scales from days to 10^6 yr, while the high-energy part ($>$ 500 MeV) varies on geological time scales (Svensmark et al., 2021). It should, however be noted that while the modulation of the solar wind is stronger for the low-energy GCR, it can effect GCR up to 10^4 MeV (Patrignani et al., 2016).

Habitability and cloud formation

Due to the long life-span of the low-mass stars, these stars make up the vast majority of all stars in the galaxy ($\sim$ 96%, see Fig. 1.3). This occurrence rate added to the long potential life of planets around these stars make them highly interesting in our search for habitable planets.

As we have seen in this section, high-energy radiation can have a significant impact on the habitablity of exoplanets, both through the chemistry and climate of the planets (e.g. Herbst et al. (2023)). This is further studied by Scheucher et al. (2020) looking at the habitability of Proxima Centauri b. Scheucher et al. (2020) finds that the breakdown of CH_4 by high-energy radiation might prevent an anti-greenhouseeffect, thereby affecting the energy balance and heating the planet into temperate climates which increases its habitability.

A study by Barth et al. (2021) combined climate simulations from 3D GCM runs with a chemical kinetic network to look at the effect of XUV, SEP, and GCR on the atmosphere of a hot-Jupiter planet (HD 189733b). They found that all three types of ionizing radiation led to an increase of key organic molecules such as HCN, CH_2O, and C_2H_4, thereby potentially making them available for the formation of life.

Ridgway et al. (2023) coupled a 3D GCM to a photochemical kinetics scheme to study the effect of stellar activity on terrestrial exoplanets. As opposed to the studies (e.g. Segura et al. (2010)) Ridgway et al. (2023) finds that flares can increase the amount of ozone in the atmosphere. They also find a significant increase in the levels of potential biosignatures such as N_2O, increasing the risk of false-positive detections. Finally they find that the changes in atmospheric composition due to flares might decrease the amount of UV radiation reaching the surface of the planet, thereby shielding potential life on the surface from this harmful radiation.

A comprehensive 3D modelling of the radiative environment of Proxima Centauri has been performed by Engelbrecht et al. (2024), where they study the transport of GCR and SEP in the system and their effect on the habitability of an Earth-like planet in the system. They report unexpectedly large GCR intensities at the planet orbit, and find that it couples to the stellar rotation rate. They propose stellar rotation rate as an observable constraint to exoplanetary habitability.

High-energy radiation has long been known to influence cloud formation through e.g. ion-induced nucleation, where the increase of ions help stabilize and promote the growth of molecular clusters (e.g. Svensmark et al. (2013, 2020); Wagner et al. (2017); Lee et al. (2019)). The previous studies of these effects will be discussed further in Chapter 2.

1.5 Aim of this work

The work presented in this thesis aims to expand on the previous studies described above and centers around the research question:
How does high-energy radiation affect exoplanet atmospheres?

We have approached this question from two different angles: 1) An experimental approach studying the behavior of mineral cloud particles under gamma radiation. 2) A modelling approach studying the disequilibrium chemistry in ex-

oplanet atmospheres under various degrees of XUV, SEP, and GCR.

Chapter 2 presents the experimental study on how high-energy radiation affects the aggregation and charging of mineral cloud particles. In this chapter we describe our experimental setup centered around an atmosphere chamber connected to a setup for aerosol production and instruments for measuring the size distribution and charging of the aerosols. The first part of the chapter describes a series of initial tests run on the setup, while the last part of the chapter describes the results of a published study on how gamma radiation affects SiO_2 particles.

Chapter 3 presents a modelling study on how the radiative environment of exoplanets affects the disequilibrium chemistry of their atmospheres. In the first part of the chapter we describe how the atmospheres are modelled using a chemical kinetics network coupled to a 1D photochemistry and diffusion code, and how XUV, SEP, and GCR are implemented into the code. In the second part of the chapter we describe the preparation and first results of an ongoing study where a test atmosphere is modelled for a range of XUV and, SEP, and GCR inputs to simulate planets in different radiative environments.

Chapter 4 presents a modelling study on how cloud formation can be implemented in GCM models in a post-processed manner using the warm Saturn, HATS-6b, orbiting an M-dwarf star as a case study. This chapter focuses on the disequilibrium chemistry of the planet atmosphere including the effect of XUV radiation and SEP.

Finally, Chapter 5 summarizes the results of the projects, and discusses potential future work.

2

High-energy radiation and mineral cloud particles

- An experimental approach

In this chapter, I present the work done in preparation for the publication Bach-Møller et al. (2024), titled "*Aggregation and charging of mineral cloud particles under high-energy irradiation*". This work utilizes an atmosphere chamber to investigate the aggregation and charging behaviors of SiO_2 particles when exposed to gamma irradiation.

The contributions to the work were as follows:

- I (first author) participated in project planning and instrument setup, conducted most of the experiments, and was primarily responsible for data analysis and writing the paper.

- Christiane Helling and Uffe Gråe Jørgensen participated in project planning, discussions, data analysis, and paper revisions.
- Martin Bødker Enghoff participated in project planning and instrument setup, conducted some of the experiments, supervised all lab work, contributed to discussions and data analysis, and provided comments and revisions to the paper.

This chapter is adapted from the publication but includes a more in-depth description of the setup and the results of several preliminary tests conducted to validate the setup. The introduction, parts of the methods, main results (Sec. 2.4.2), discussion, and conclusion are close to their original version from the publication.

2.1 Background and Aim

The effect of cosmic rays on cloud formation has been studied extensively for Earth's atmosphere, and it has been found that there is a significant correlation between the influx of high-energy particles and the degree of cloud formation (Dickinson, 1975; Svensmark & Friis-Christensen, 1997; Marsh & Svensmark, 2000; Svensmark et al., 2021). As high-energy particles reach the atmosphere, they form so called *cosmic ray showers*, where the particles interact with the gas and release of gamma rays resulting in an ionization of the gas. The increased presence of ions has been found to stabilize and promote the formation and growth of molecular clusters in Earth's atmosphere, leading to ion-induced nucleation of cloud particles (Svensmark et al., 2017; Lee et al., 2019; Wagner et al., 2017). A series of studies (Svensmark et al., 2013; Enghoff & Svensmark, 2017; Svensmark et al., 2020) have looked at ion-induced nucleation by imitating high-energy particles using gamma radiation. Svensmark et al. (2013) found that gamma irradiation increases the nucleation rate of H_2SO_4 clusters from the gas-phase, and induces the nucleated clusters to grow to 50 nm sizes. Using a similar experimental setup, Enghoff & Svensmark (2017) found that gamma radiation changes the charging state of the particle population and that particles react differently to gamma radiation depending on their size and polarization. Enghoff & Svensmark (2017) suggest that different ions participate in the charging of positively and negatively charged particles, and that the differences in the size and mobility of these ions affect the charging of the particles by the gamma irradiation.

The effect of high-energy radiation is also known to apply to particles very

different from the ones participating in Earth-like cloud formation (e.g. metallic nanoparticles (Abedini et al., 2013)), indicating a relevance to fields other than cloud formation. One such example is the study of interplanetary dust. Interplanetary dust has long played an important role in solar system space mission (Grün et al., 1992; Jorgensen et al., 2021), and an improved understanding of the effect of the radiation environment on particles could be highly beneficial for future solar system missions, such as Comet Intercepter (Snodgrass & Jones, 2019), and for our understanding of dust in planetary systems as a whole.

So far, the effect of high-energy particles on cloud formation has mostly been studied for the initial molecular nucleation from the gas-phase of volatile species characteristic to the atmosphere of Earth.
The aim of this study has been to explore the question of how high-energy radiation affects the aggregation and charging of already formed mineral cloud particles. The mineral cloud particles investigated in this study are SiO_2. SiO_2 is known to be relevant both as mineral cloud species on gaseous exoplanets, AGB Stars and Brown Dwarfs Lee et al. (2016); Helling et al. (2006), and as cloud condensation nuclei in Earth-like atmospheres.

The experimental setup used in this study is similar to the setups used previously by Enghoff & Svensmark (2017) and Motzkus et al. (2013), but differs by allowing the introduction of solid mineral particles into an atmosphere chamber. In Sec. 2.2 we present the experimental setup focusing on the most important instruments used in our experiments, and describe the theory behind the measurements and how the results are calculated. Since new additions have been made to the setup for this study, Sec. 2.3 presents a series of preliminary tests that have been done, and explain some of the choices that were made for the final experiments based on these tests. Finally, Sec. 2.4 presents a set of experiments done on the aggregation and charging of SiO_2 particles ($d \approx 50$ nm) the majority of which have been published in (Bach-Møller et al., 2024). In Sec. 2.5 we discuss and summarize the results.

2.2 Experimental setup and methods

The main purpose of the experiments in this study is to address the question of how mineral cloud particles are affected by high-energy radiation. To do this we release mineral particles suspended liquid solution and introduce them into an atmosphere chamber where they are irradiated with high-energy radiation under

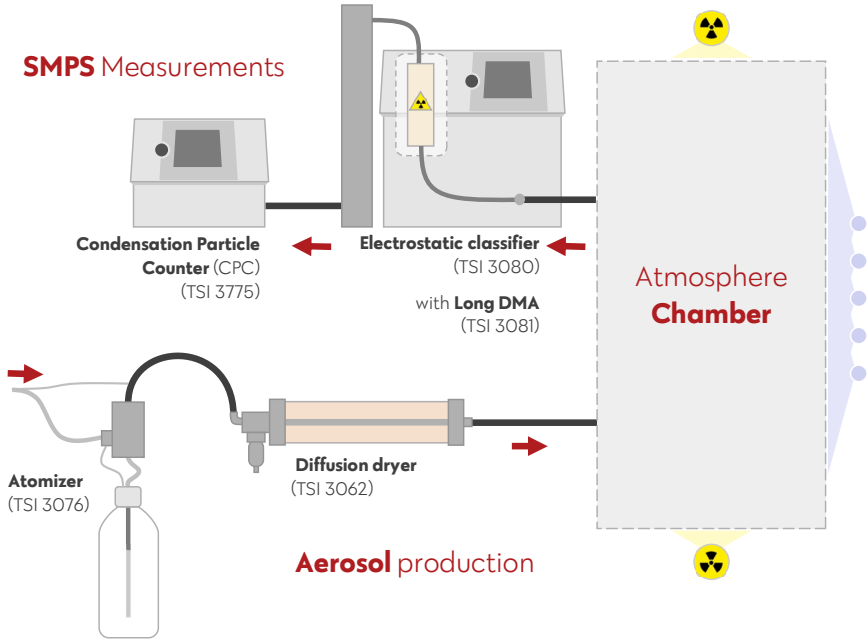

Figure 2.1: Experimental setup. The process begins with aerosol production (lower left), continues to the atmosphere chamber (right), and ends with measurements at the SMPS system (upper left). Arrows mark the airflow through the system.

different conditions. The effect of the high-energy radiation on the particle size and charging state is measured based on their mobility in a known electric field.

The experimental setup can be separated into three parts: a) The production of aerosols (bottom left in Fig. 2.1). b) The atmosphere chamber (right in Fig. 2.1). c) The measurements done with a Scanning Mobility Particle Sizer, SMPS (top left in Fig. 2.1).

Parts of the setup have been used in previous studies to measure the nucleation of particles from the gas-phase (Svensmark et al., 2013; Enghoff & Svensmark, 2017; Svensmark et al., 2017). In these previous experiments, a mixed gas composition of H_2O, O_3, and SO_2 was introduced into the chamber, where it would nucleate to form H_2SO_4 particles. The nucleation, growth, and charge of these newly formed particles was measured by the SMPS system. In this study, we have altered the setup in order to introduce already formed aerosols into the chamber, by implementing an atomizer and diffusion dryer to the inflow into the chamber. Similar instruments are used in other studies (Motzkus et al., 2013; Chien et al.,

2022; Massoudifarid et al., 2022) to observe e.g. SiO_2, NaCl. and the spread of virus aerosols, but they are new additions to our setup.

2.2.1 Aerosol production

The experiment is started by separating and releasing mineral particles from a liquid solution, to form non-interacting aerosols in an airflow with as low humidity as possible.

The mineral particles used in this study come from MSP NanoSilica™ Size Standards. The NanoSilica™ Size Standards are aqueous suspensions of amorphous SiO_2 particles with a highly uniform size distribution. In this study we have looked at two samples of particles with diameters of 20 nm and 50 nm respectively.

The samples are prepared by being lowered into a sonic bath to ensure separation of the particles in the suspension, before it is diluted in Milli-Q water (water that has been purified and deionized using a Millipore Milli-Q lab water system). The particle concentrations in the sample bottles and in the diluted aqueous suspension can be seen in table 2.1.

Sample	20 nm	50 nm
Concentration from producer	$4.6 \cdot 10^{15}\,\mathrm{ml}^{-1}$	$2.0 \cdot 10^{11}\,\mathrm{ml}^{-1}$
Concentration in atomizer*	$1.6 \cdot 10^{14}\,\mathrm{ml}^{-1}$	$7.1 \cdot 10^{9}\,\mathrm{ml}^{-1}$

Table 2.1: Concentration of SiO_2 particles used in experiments. * The concentrations given here are the standard concentrations of the sample added to the atomizer, and might differ between experiments.

The particles are released from the aqueous suspension using an atomizer (TSI 3076) as illustrated in Fig. 2.2. In the atomizer the liquid sample is exposed to a high-velocity jet of compressed air, which converts the liquid into an aerosol spray where the individual SiO_2 particles are moving, well separated, with the air flow. Larger droplets are removed from the air flow through impact with the wall opposite the jet, and will be drained as excess water. The atomizer can be run in two settings: 1) the recirculation mode where the excess water is returned to the sample bottle, and 2) the non-recirculation mode where the excess water is drained into a closed reservoir. The first option allows the experiment to run for a longer period of time compared to the second option by slowing down the rate at which the sample is used, but it also dilutes the sample partially over time. We have chosen to use the recirculation mode for this study, due to the extended

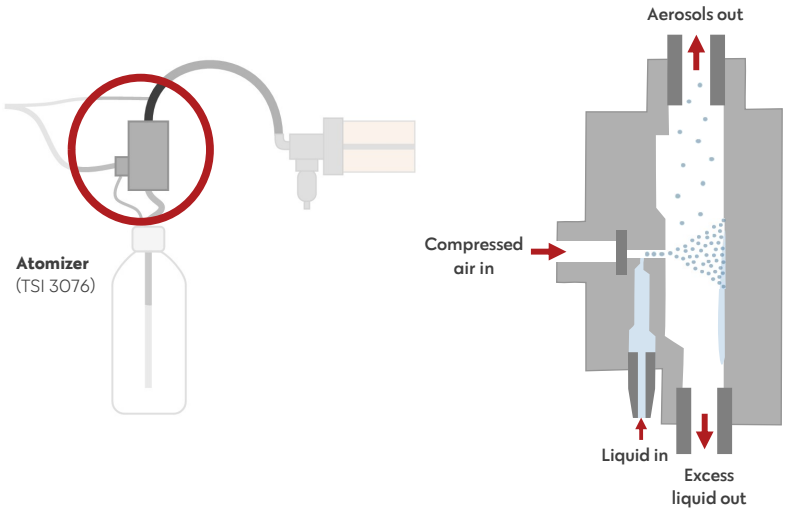

Figure 2.2: Illustration of atomizer (TSI 3076) showing the production of aerosols from a liquid solution using a jet of compressed air TSI Incorporated (2005).

experiment duration and the general recommendation from TSI to use the re-circulation for water-based solutions (TSI Incorporated, 2005). Using this setup our experiments can run for approximately five days before the sample runs out, which allows us to run multiple experiments before having to disturb the setup. The atomizer is operated using a flow of clean dry nitrogen at a rate of 3 L/min from a Parker Midigas 6 nitrogen generator with an O_2 content of 10 ppm at maximum. An additional flow of nitrogen of 1 L/min is added to the outflow of the atomizer.

The outflow from the atomizer has a relative humidity of RH $\approx$ 100% due to the liquid solution the particles are suspended in. In order to lower the humidity, the air flow is passed through a diffusion dryer (TSI 3062), resulting in a humidity of RH $\approx$ 60%. The diffusion dryer is designed to remove water from the sample with a minimal aerosol loss and can be seen illustrated in Fig. 2.3. At the inlet of the diffusion dryer the air flow passes through a water trap where larger droplets can be collected and drained. The flow then pass through a desiccant dryer that consists of two concentric cylinders: an outer acrylic cylinder and an inner wire screen cylinder with silica gel in-between. By allowing the airflow to pass through the inner wire screen cylinder while not getting into direct contact with the silica gel, the water vapour from the flow can diffuse through the wire screen with a minimal loss of particles.

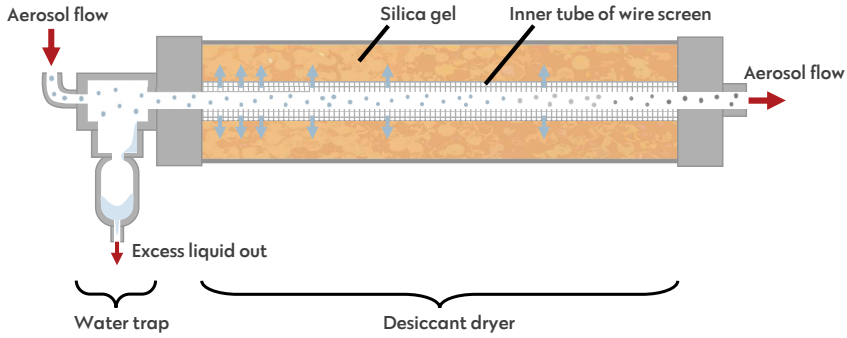

Figure 2.3: Illustration of atomizer (TSI 3076) showing the production of aerosols from a liquid solution using a jet of compressed air. TSI Incorporated (2005).

The humidity of the air flows and the effect of the diffusion dryer is tested in Sec. 2.3.

2.2.2 Atmosphere chamber

After the mineral particles have been released as aerosols and excess water vapor has been removed, the particles are introduced into an atmosphere chamber where the aggregation and irradiation of the particles can take place.

The atmosphere chamber is a 2 m × 2 m × 2 m cube made of electro-polished stainless steel with the exception of one side made of teflon to allow for experiments with UV from external lamps. All experiments in this study are conducted at approximate room temperature (around 21-23 °C) and slightly above atmospheric pressure (differential pressure of ∼0.2 mbar to the surroundings) to prevent the inflow of contaminating air from outside the chamber. In addition to the aerosol airflow, the pressure in the chamber is maintained by an additional airflow of 12 L/min clean nitrogen. Five UV lamps (253.7 nm) are placed along the teflon side of the chamber. Two gamma sources (caesium-137 sources with activities of 27 MBq) are located on opposite sides of the chamber. The level of irradiation can be controlled by varying the shielding of the radiation sources done by sheets of lead with thicknesses of 0.5, 1, and 2 cm respectively. Varying the shielding results in ion production rates in the chamber ranging from 16-200 $cm^{-3}s^{-1}$.

Introducing the particles into the chamber at a steady rate, it takes approximately 10 hours for the particle number density to reach a plateau, as shown in Fig. 2.6. All measurements are therefore taken 15 hours or more after initiating

the inflow of particles. If there was a change in the irradiation of the chamber, 30 minutes or more were allowed to pass before further measurements were taken, in order for the ionization to be allowed to take place. Over time some of the particles will leave the gas phase through collision with the chamber walls, which is tested in Sec. 2.3.

The relative humidity from the combined air composition in the chamber was measured to RH $\approx$ 20%. In order to increase and control the humidity of the chamber the inflow of air can be connected an external humidifier where temperature controlled water is passed through a GoreTex tube that goes through the air stream to the chamber.

2.2.3 Scanning Mobility Particle Sizer (SMPS)

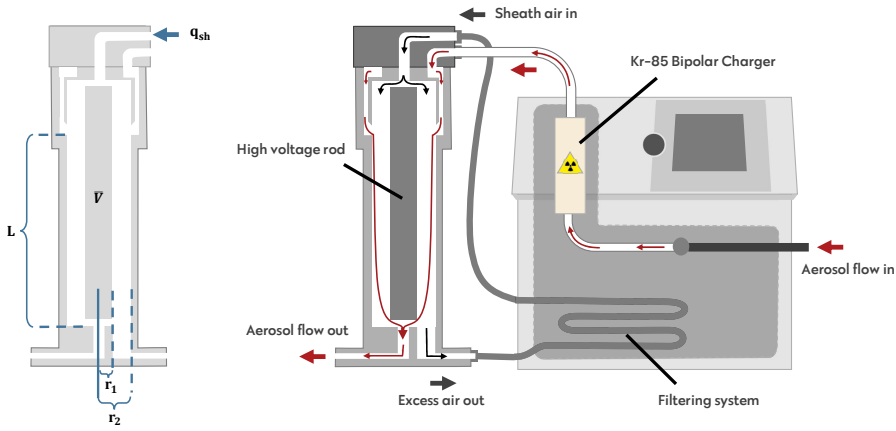

Figure 2.4: Illustration of Electrostatic Classifier (TSI 3080), with Long DMA (TSI 3081). Left: Dimensions of the Long DMA with the values used in Eq. 2.3 and 2.4. Right: Red arrows follow the aerosol flow through the system as it is charged by the bipolar charger, moves through the electric field of the DMA, and is sorted based on electric mobility.

In order to follow the aggregation and charging of the particles, a Scanning Mobility Particle Sizer (SMPS) system is connected to the outflow of the chamber. The SMPS system is designed to measure the electric mobility distribution of the particles and it consists of two parts: An Electrostatic Classifier (see Fig. 2.4) and a Condensation Particle Counter (CPC).

The principle behind the SMPS system is the correlation between the size and charge of particles and their electrical mobility. The electrical mobility (Z_p) reflects

the ability of a particle to move through a medium in response to an electric field, and can be described as:

$$Z_p = \frac{neC}{3\pi\mu D_p} \tag{2.1}$$

where n is the number of elementary charges on the particle, e is the elementary charge, C the Cunningham slip correction (that depends on the gas mean free path which is calculated continuously and D_p), μ the gas viscosity, and D_p the particle diameter (TSI Incorporated, 2009). For small particles or aggregated clusters the particle cannot be assumed to be spherical and D_p will be defined as the *mobility diameter* rather than the physical diameter.

In order to determine the aggregation of the particles, their size distribution must be found, and as shown in Eq. 2.1 this can be done based on the charge and electrical mobility. The SMPS system brings the particles to a known charge distribution in the electrostatic classifier using a Kr-85 Bipolar Charger (also called a neutralizer). The bipolar charger ionizes the air and exposes the particles to high concentrations of bipolar ions. Through collisions with these ions the particles themselves are brought into a known steady-state bipolar charge distribution, where a fixed percentage of the particles will carry none, one, or multiple charges. The bipolar charge distribution has been described by Wiedensohler (1988) and Fuchs et al. (1965), and can be expressed as follows (equation from TSI Incorporated (2009)):

$$f(N) = 10^{\left[\sum_{i=0}^{5} a_i(N)\left(log\frac{D_p}{nm}\right)^i\right]} \tag{2.2}$$

Where N is the number of elementary charge units, D_p is the particle diameter, and a_i is a coefficient depending on N.

The charged particles are passed into a Long Differential Mobility Analyzer (DMA) (TSI 3081), where an electric field allows only particles in a specific electric mobility range to pass through (see Fig. 2.4). The relationship between the electrical mobility and the parameters of the DMA has been described by Knutson & Whitby (1975) as:

$$Z_p^* = \frac{q_{sh}}{2\pi\bar{V}L} ln\left(\frac{r_2}{r_1}\right) \tag{2.3}$$

Where Z_p^* is a set mobility, q_{sh} is the sheath flow rate, $\bar{V}$ is the average voltage used for the DMA, L is the distance between the exit slit and the aerosol inlet in the DMA, and r_1 and r_2 are the inner and out radius of the annular space in the DMA.

Combining Eq. 2.1 and Eq. 2.3, the particle diameter can be related to the number of charges on the particles, the collector rod voltage, the flow rate of the classifier, and the geometry of the DMA (TSI Incorporated, 2009):

$$\frac{D_p}{C} = \frac{2ne\bar{V}L}{3\mu q_{sh} ln\left(\frac{r_2}{r_1}\right)} \tag{2.4}$$

As can be seen from Eq. 2.4 the mobility diameter of a particle can be found based on the charge of the particle and the instrumental setup of the classifier.

As the electric field of the DMA is varied the particles are being sorted based on their mobility, such that the number density of particles within a specific mobility range can be measured. The final measurement is done by a Condensation Particle Counter (CPC) (TSI 3775), that functions by growing the particles to sizes that can be detected through an optical detector. This is done by passing the particles through a heated saturator with vaporized butanol. The butanol enters into the aerosol flow, and together they pass into a cooled condenser. Due to the lower temperatures the butanol becomes supersaturated and condenses onto the particles growing to larger droplets that pass to a particle counting optical detector.

The instruments are operated under the following conditions: The Electrostatic classifier is operated with a sheath flow (the additional air flow entering the DMA) of 3 $Lmin^{-1}$, and the CPC was operated on low-flow mode at 0.3 $Lmin^{-1}$. The choice of using a long DMA together with these flow setting allows us to measure particles within a size range of 13-500 nm. Scan times were chosen for the SMPS based on the flow rates and desired particle size range in addition to the CPC response time. The scan up time, which determines the time spent by the classifier to increase the voltage over the DMA, was set to 180 s, whereas the scan down time, which determines the time taken by the classifier to return to the initial voltage, was set to 60 s. This scan time of a total of 240 s is in accordance with the settings previously used by (Motzkus et al., 2013) to measure SiO_2 particles using a similar setup. The final size distributions are found by averaging over 50 consecutive scans as explained in Sec. 2.2.4.

Charging state

In order to study the charging of the SiO_2 particles the *charging state* is calculated. The charging state is a measure of the charge of the particle population in relation to the steady-state charge distribution implemented by the Kr-85 bipolar charger (Laakso et al., 2007). This is done by replacing the neutralizing Kr-85 charger with a non-neutralizing "dummy", that is identical to the charger but with no Kr-85 source (as explained in Enghoff & Svensmark (2017)). While using the "dummy", the particles will keep the charges they had in the chamber, and the measured electric mobilities will reflect these charges in addition to the particle sizes. The charging state is calculated by dividing measurements performed with the dummy with identical measurements performed with the Kr-85 bipolar charger.

Since the electric field of the DMA will sort for either positively or negatively charged particles, these will be measured separately in the SMPS system. The polarity of the particles being measured is decided by changing the power supply in the classifier, such that a positive power supply will result in the negatively charged particles being measured, and a negative power supply will result in the positively charged particles being measured (Enghoff & Svensmark, 2017).

2.2.4 Evaluation of measurements

All results in this study are based on size distribution measurements done with the SMPS. From these measurements we calculate: average size distributions of different "experiments", number densities of different aggregates, and charging states. In this section we will describe these calculations as well as their associated uncertainties.

Size distribution of experiment:

A single experiment in this study consists of 50 individual size distribution measurements (scans) taken consecutively by the SMPS. Since aerosols generally follow a lognormal size distribution (e.g. Heintzenberg (1994)) the SMPS system will generally output the sizes on a logarithmic scale ($\log(D_P)$) TSI Incorporated (2012). To allow for more easy visual comparison of plots with different size resolutions, the particle concentrations are therefore given by the SMPS as normalized concentration ($dN/d\log D_p$), where dN is the particles concentration and D_p is the midpoint particle diameter for the size-range in which the particles have been

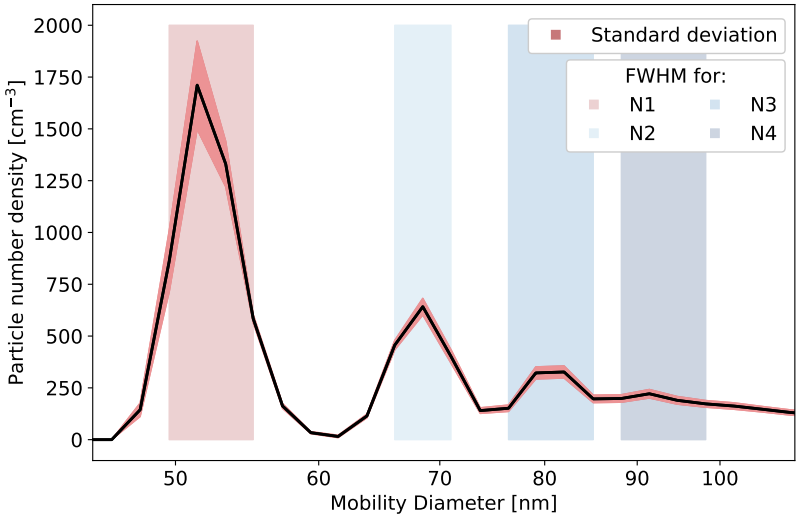

Figure 2.5: Size distribution of particles in experiment with negatively charged particles. N1-N4 indicates the aggregate size (monomer to four aggregated particles). Black line indicates the average and red shading indicates the standard deviation among the 50 measurements constituting this experiment. Shaded areas indicate the FWHM for each peak.

measured as determined by the DMA (see Sec. 2.2.3). The correlation between the normalized concentration ($dN/dlogD_p$) and actual concentration (dN) can be described as (TSI Incorporated, 2012)

$$dN/dlogD_p = \frac{dN}{log(D_{upper}) - log(D_{lower})} \tag{2.5}$$

To get the actual particle concentration from normalized concentration, we therefore multiply the output of the SMPS by the width of the logarithmic size-bin.

The final size distribution of each experiment is found as the average of the 50 consecutive measurements. The standard deviation (σ) and standard error of the mean ($\sigma_{\overline{x}}$) are found for each size bin as:

$$\sigma = \sqrt{\frac{\sum_{i=1}^{n}(x_i - \overline{x})^2}{n-1}} \tag{2.6}$$

$$\sigma_{\overline{x}} = \frac{\sigma}{\sqrt{n}} \tag{2.7}$$

where x_i are each of the measured particle concentration, $\overline{x}$ is the average of the consectutive measurements, and n is the number of measurements.

Number density of aggregates:

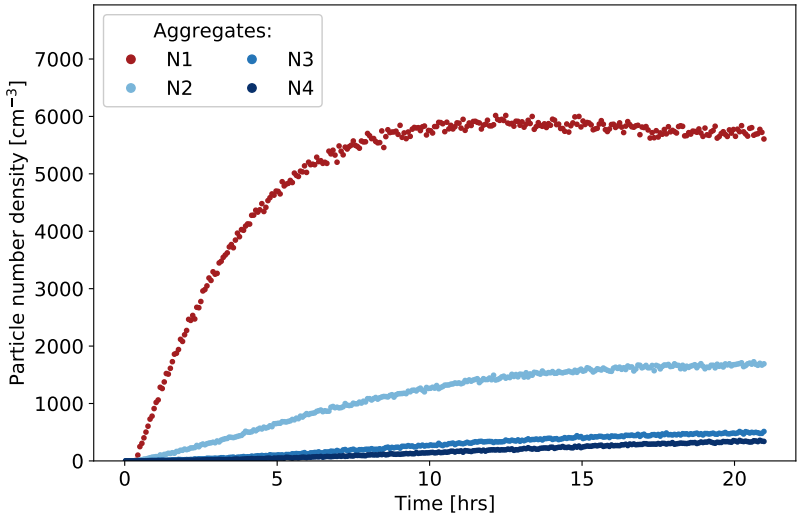

Figure 2.6: Number densities of single particles, N1, and each of the aggregates, N2-N4, over time from the moment the inflow of particles is initiated.

An example of the average size distribution for an experiment is shown in Fig. 2.5 This experiment was done on negatively charged particles from the d $\approx$ 50 nm sample. The standard deviation among the 50 measurements making up the experiment is shown in red.

As shown in Fig. 2.5 and explained in Sec. 2.4.2, the size distribution shows distinct peaks, indicating that the particles cluster to form aggregates of different sizes. The number of aggregates of each size is found as the sum of measured particles within the full width half maximum (FWHM) of the peak. Fig. 2.5 shows the FWHM shaded for the monomers (N1, the d $\approx$ 50 nm particles) and aggregates of two, three, and four particles (N2 - N4). The uncertainty of the number density is found through linear error propagation from the standard deviation of each size bin in the size distribution of the experiment. Linear error propagation is used for finding the standard deviation of a function (y) that can be expressed as a linear

combination of variables (a, b, c) with each their coefficient (k_a, k_b, k_c):

$$y = k_a \cdot a + k_b \cdot b + k_c \cdot c \tag{2.8}$$

The error of the functions (σ_y) can then be expressed from the standard deviation of its constituents (σ_a, σ_b, σ_c):

$$\sigma_y = \sqrt{(k_a \cdot \sigma_a)^2 + (k_b \cdot \sigma_b)^2 + (k_c \cdot \sigma_c)^2} \tag{2.9}$$

Since the number density is found as the sum of particles within the FWHM the standard deviation is found from the standard deviation of the experiments as described in the previous section.

Fig. 2.6 shows the number density of each of the aggregates over time since the particles were first introduced into the chamber. As can be seen the number of single particles, N1, plateaus after $\sim$ 10 hours, while the number densities of the aggregates continues to increase, indicating a continued aggregation over time. We will discuss more on the number densities later.

Charging state:

As mentioned in Sec. 2.2.3 the charging state is a measure of the charge of the particle population in relation to a bipolar charge distribution implemented by the Kr-85 bipolar charger. In order to calculate the charging state, two experiments are performed after each other, one with the Kr-85 bipolar charger and one with the dummy. The number density of each aggregate size is calculated for each of the experiments, and the charging state (CS) is found as the number density of particles (dN) from the measurement with the dummy divided by the measurement with the bipolar charger,

$$CS = \frac{dN_{dummy}}{dN_{bipolar\ charger}} \tag{2.10}$$

A charging state of 1.0 would indicate that the aggregates in the chamber follow the same steady-state charge distribution as implemented by the bipolar charger. Charging states different from 1.0 show that the particles deviate from the steady-state distribution, indicating that the aggregates are actively being charged. Values above 1.0 indicate an overcharge of the particles (a higher number of charged particles than in the steady-state), and values below 1.0 in-

dicate an undercharge of the particles (a lower number of charged particles than in the steady-state). The uncertainty of each charging state calculation is found using the standard formula for error propagation from the uncertainties of the particle number densities. The standard formula for error propagation describes the standard deviation(σ) of a function (y) that can be expressed from a combination of variables (a, b, c) with the coefficient (k):

$$y = \frac{kab}{cd} \tag{2.11}$$

The error of the functions (σ_y) can then be expressed from the standard deviation of its constituents (σ_a, σ_b, σ_c):

$$\sigma_y = y \cdot \sqrt{\left(\frac{\sigma_a}{a}\right)^2 + \left(\frac{\sigma_b}{b}\right)^2 + \left(\frac{\sigma_c}{c}\right)^2 + \left(\frac{\sigma_d}{d}\right)^2} \tag{2.12}$$

The standard deviation of the charging state is thereby found from the standard deviations of the number densities.

In order to increase the accuracy the results the charging state calculations are repeated for multiple experiments, and the final charging states shown in this study are averages among these repeated experiments. The uncertainties for the averages are found in two ways: 1) Error propagation of the errors of each charging state. 2) The standard deviation among the repeated experiments.

2.3 Preliminary tests

Before beginning the actual experiments, we ran a number of preliminary tests. We first test two SiO_2 samples (with diameters of d $\approx$ 20 nm and d $\approx$ 50 nm). We then test the effect of the atomizer and diffusion dryer; the new additions to the setup. We then test the effects of high-energy radiation (gamma and UV respectively). Finally, we test the loss rate of particles to the chamber walls.

Notice that the results in this section are generally showing single measurements and therefore do not indicate averages over repeated measurement or experiments, as described in Sec. 2.2.4.

2.3.1 Testing SiO_2 samples

To test SiO_2 particles samples with the setup, we aimed to reproduce the results of Motzkus et al. (2013). Motzkus et al. (2013) is an extensive study that compares different techniques for measuring the size distribution of airborne SiO_2 particles with diameters of $\sim 30\,\text{nm}$ and $\sim 80\,\text{nm}$. The measurements were performed in 15 different laboratories, many of which used experimental setups similar to ours, with an atomizer, diffusion dryer, and an SMPS system as seen in Fig. 2.7. A major difference between the setup used by Motzkus et al. (2013) and our setup is the use of an atmosphere chamber in our study.

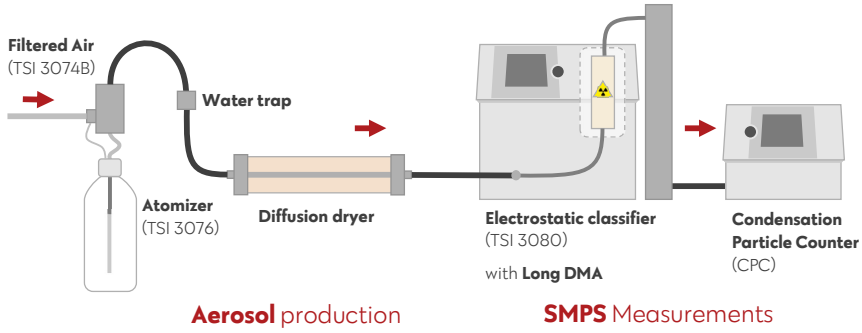

Figure 2.7: Illustration of experimental setup used by most laboratories in Motzkus et al. (2013) as described by Fig. 1 in Motzkus et al. (2013).

Motzkus et al. (2013) measure the size distribution for a mono-species sample of $\sim 30\,\text{nm}$ particles and a double-species sample of $\sim 30\,\text{nm}$ and $\sim 80\,\text{nm}$ particles. In both cases they find distinct peaks at the diameters expected for the respective samples $\sim 30\,\text{nm}$ and $\sim 80\,\text{nm}$ (see Fig. 3 from Motzkus et al. (2013)). The peaks for both sample sizes have a small shoulder at higher diameters indicating the presence of larger aggregates (which will be explored more later in regard to our own investigation).

In this study, we had two criteria for choosing the diameters of the SiO_2 particle samples: 1) The size difference between the samples should be large enough to form distinct peaks in the size distribution. 2) It should be possible to measure the samples within the same scanning range of the classifier. The second criteria should still be valid as the particles would aggregate, which made it beneficial to choose particles as small as possible (the lower size limit being 13 nm, as described in Sec. 2.2.3), while still obeying the first criteria. We therefor chose SiO_2 samples

with diameters of 20 nm and 50 nm.

The size distribution for the 20 nm sample can be seen in Fig. 2.8 for three cases; a high concentration (high conc) sample (where the particle concentration in the atomizer was $\sim 3.2 \cdot 10^{12}$ particles ml^{-1}) with diffusion dryer (DD), and two low concentration (low conc) samples ($\sim 8.0 \cdot 10^{11}$ particles ml^{-1}), with and without diffusion dryer.

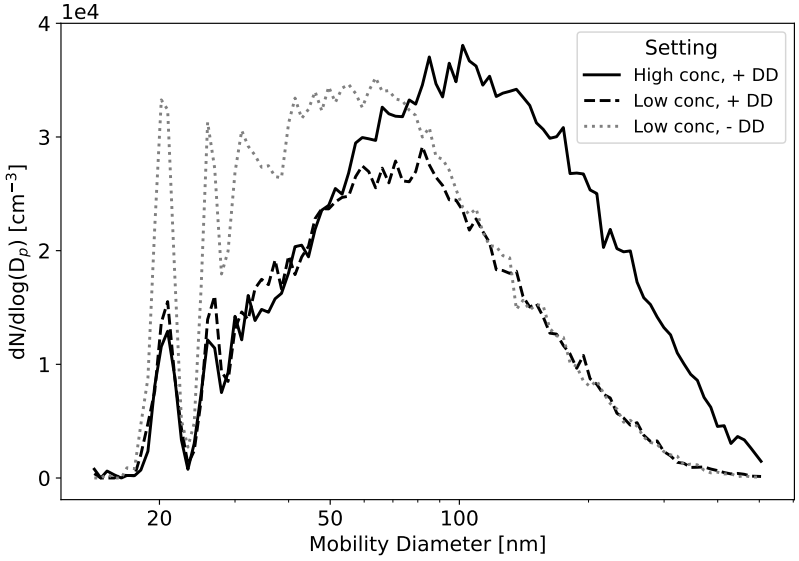

Figure 2.8: Size distribution for 20 nm particles. Solid line: High concentration of SiO_2 particles in the atomizer, with diffusion dryer (DD). Dashed: Low concentration of SiO_2 particles in the atomizer, with diffusion dryer. Dotted: Low concentration of SiO_2 particles in the atomizer, without diffusion dryer.

None of the three cases in Fig. 2.8 show the distinct peak we had expected based on the study by Motzkus et al. (2013). Instead the distributions are dominated by a wide peak at $\sim 60-100$ nm and some smaller at ~ 20 nm and ~ 27 nm. Comparing the high- and low concentration cases (solid and dashed lines), we notice that the wide peak, especially at larger diameters, scales with concentration, indicating that this peak might be due to particles growth that is more predominant for higher concentrations. The smaller peaks seem to follow an opposite trend. The smaller peaks at ~ 20 nm and ~ 27 nm do not scale significantly with concentration (or they might even scale inversely), but are instead significantly more distinct for the case without diffusion dryer (dotted line). This could in-

dicate that these peaks are less dependent on particle concentrations, and are somewhat related to the amount of Milli-Q water entering the chamber (this will be further explored in Sec. 2.3.2).

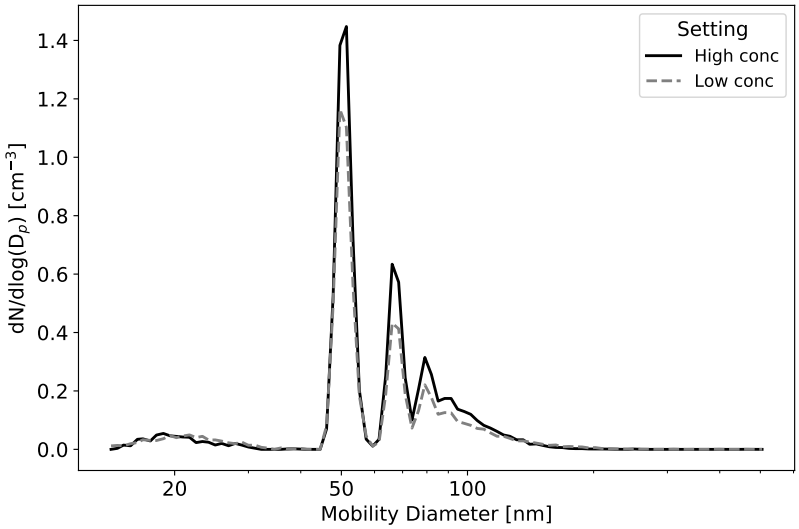

Figure 2.9: Size distribution for 50 nm particle sample. Solid line: High concentration of SiO_2 particles in the atomizer. Dashed: Low concentration of SiO_2 particles in the atomizer. In both cases the diffusion dryer is included in the setup.

The size distribution for the 50 nm sample can be seen in Fig. 2.9 for two cases: a high concentration (high conc) sample (where the particle concentration in the atomizer was $\sim 1.4 \cdot 10^{10}$ particles ml^{-1}) and a low concentration (low conc) sample (where the particle concentration in the atomizer was $\sim 7.1 \cdot 10^{9}$ particles ml^{-1}). In both cases the diffusion dryer was included in the setup. As shown in Fig. 2.9 (and previously mentioned in Sec. 2.2.4), the measurements of the 50 nm sample show clear peaks, not only for the individual monomers (at 50 nm) but also for larger aggregates of particles sticking together. All peaks scale with concentration, indicating that they are created by the 50 nm particles.

The 20 nm and 50 nm samples therefore display very different behaviours. One potential explanation for the size distribution seen in Fig. 2.8 could be that the 20 nm particles are growing. A study by Svensmark et al. (2020) modelled how the presence of ions affects the growth of aerosols, and found that the presence of ion-pairs increased the growth rate, but not the charged aerosol coagulation. The increase in growth rate due to ion concentration was found to be largest

for particles smaller than 25 nm. As we will show in the next section, the unexpected distribution seen for the 20 nm particles in Fig. 2.8 is not found for 50 nm particles (see Fig. 2.9). This might be related to the findings by Svensmark et al. (2020) that show that aerosol growth rates are dependent on the concentration of ion-pairs, and that the growth rate enhancement is largest for particles smaller than 25 nm. If the concentrations of ion-pairs in the chamber are high this will therefore promote the aggregation of the 20 nm particles more than the 50 nm particles.

From Tab. 2.1, we notice that the concentration of the 20 nm SiO_2 sample from the producers side is 4 orders of magnitude higher than for the 50 nm sample. The differences observed in the size distribution of the two samples might therefore also be due to extremely high concentrations of 20 nm particle in the chamber, rather than a size dependent growth mainly affecting the 20 nm particles. The significant difference in he sample concentrations was not discovered until late in the project. Due to time constraints and availability for resources, the experiments for the 20 nm particles were not repeated. In addition to that, other preliminary tests (see Sec. 2.3.2 and 2.3.2) shows that the Milli-Q water the particles are suspended in also has a feature at 20 nm.

Due to the unexpected size distribution for the 20 nm particles, the potentially high tendency for aggregation, as well as the Milli-Q feature at 20 nm conflicting with this particle size, the 20 nm sample was excluded and we moved on with the 50 nm sample for the final study.

2.3.2 Testing the effect of atomizer and diffusion dryer

In preparation for this study an atomizer and diffusion dryer was added to an existing setup that has previously been used to measure the nucleation and growth of molecular clusters (Enghoff & Svensmark, 2017). This is done in order to introduce solid SiO_2 particles into the atmosphere chamber. As explained in Sec. 2.2.1, the atomizer releases aerosols from a liquid suspension of SiO_2 particles in Milli-Q water. The diffusion dryer removes part of the excess Milli-Q water in order to lower the humidity of the airflow.

In these tests we look at the size distributions of particles in the chamber before and after the additions of the atomizer and diffusion dryer, as well as the humidity of the airflow at different points in the setup.

Atomizer

In the atomizer, the SiO_2 particles are suspended in Milli-Q water. For this reason, Milli-Q water is introduced into the experiment together with the particles.

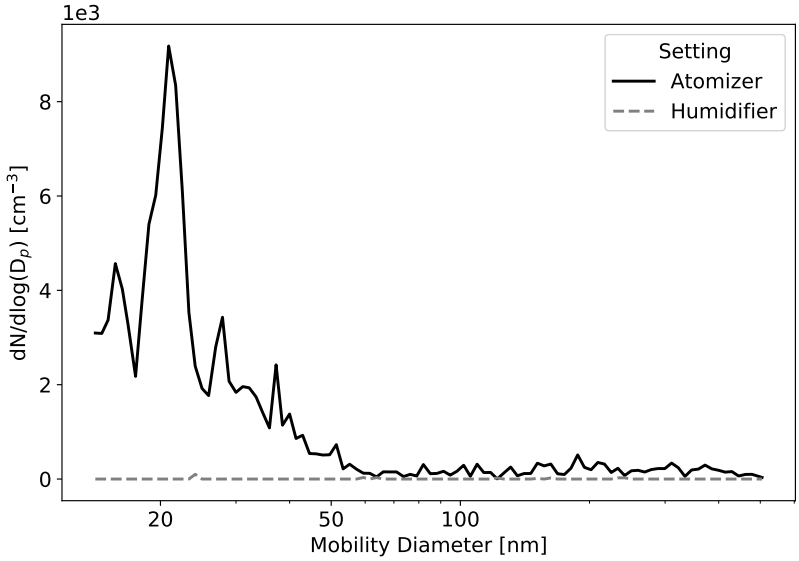

Figure 2.10: Size distribution of particles coming from chamber introduces by atomizer and humidifier respectively. Solid line: The atomizer with pure Milli-Q water (no sample) is connected to chamber. Dashed line: Humid air introduced directly to chamber with humidifier.

Fig. 2.10 shows the size distribution of particles measured from the chamber during two setups. Solid line: The atomizer is connected to the chamber with pure Milli-Q water (no SiO_2 particles). Dashes Line: The atomizer is disconnected, but a humidifier containing Milli-Q water is connected to chamber. The figure shows a significant signal at lower diameters for the atomizer that is not visible for the humidifier, indicating that the atomizer introduces pure Milli-Q aerosols into the chamber, and not just humid air. This signal is strongest at $\sim$20 nm which supports our decision not to include SiO_2 particles with diameters of 20 nm in this study.

Diffusion dryer

To minimize the amount of Milli-Q water introduced by the atomizer, the diffusion dryer is connected to the output of the atomizer. In order to test the efficiency of the diffusion dryer we measure the relative humidity (RH) of the airflow from

the atomizer and humidifier with and without the diffusion dryer. The results are shown in Tab. 2.2. As can be seen from the table, the diffusion dryer lowers the relative humidity (RH) of air from the atomizer by more than 30% from over 90% to 60%. By comparison, air from the humidifier is lowered from more than 70% to 3%.

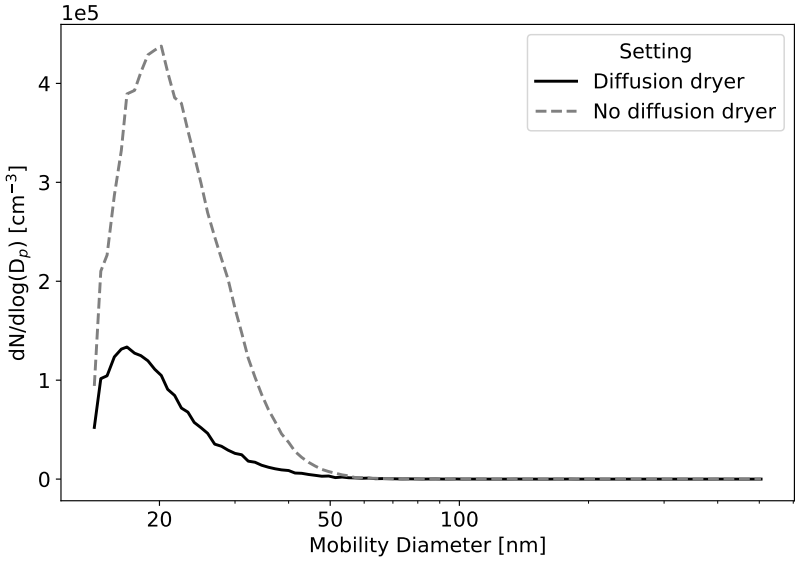

Figure 2.11: Size distribution of particles coming from chamber introduces by atomizer and humidifier respectively. Solid line: The atomizer with pure Milli-Q water (no sample) is connected to chamber. Dashed line: Humid air introduced directly to chamber with humidifier.

To further test the effect of the diffusion dryer, the size distribution of Milli-Q particles (no SiO_2 sample included) from the output of the atomizer are measured, with and without the diffusion dryer. This measurement was done by connecting the SMPS directly to the output of the atomizer-diffusion dryer setup, and as such the chamber was not involved. The results can be seen in Fig. 2.11. The figure indicates that the signal from the Milli-Q water is significantly lowered when the diffusion dryer is included. It also indicates that the diffusion dryer does not introduce additional particles to the airflow, since no other features than the Milli-Q feature is visible.

RH	No diffusion dryer	Diffusion dryer
Humidifier	$\sim 76\%$	$\sim 3\%$
Atomizer	$> 96\%$	$\sim 60\%$

Table 2.2: The table shows the relative humidity (RH) of air passing through a humidifier and atomizer respectively, with and without adding a diffusion dryer to the setup.

2.3.3 The effect of UV and gamma radiation

Our experimental setup has two different sources of high-energy radiation: UV radiation and gamma radiation. In order to test these two source we look at their effect on the aggregation and charging of the 50 nm SiO_2 particles. This was done by introducing the particles to the chamber, waiting at least 12 hours for the particle population to stabilize and then activate either the five UV sources at 40% intensity or removing all shielding plates from the two gamma sources. The top row of Fig. 2.12, shows how the number densities of each aggregate change over time with the introduction of radiation. The arrows indicate changes in radiation as the UV or gamma sources is being turned "on" or "off". To get a clearer view of especially the larger aggregates, linear curves were fitted to the data points shown in Fig. 2.12A1 and B1, after each change in radiation. The change in the slopes of each linear fit can be seen in Fig. 2.12A2 and B2. The linear fits were made for each change in the radiation, corresponding to the sections between the arrows in Fig. 2.12A1 and B1 and the sections before and after the first and last arrow respectively. Each linear fit was started 30 min after the change in radiation in order to allow for the ionization of the gas in the chamber to adapt to the change. The values plotted in Fig. 2.12A1 and B1 are calculated as the slopes of these linear fits subtracted from the initial slope before the first change in radiation.

Looking at 2.12A1 and B1 it can be seen that the gamma radiation has a clear effect on the particle number densities, especially on the single particles (N1), whereas the effect of UV is less visible. Looking more closely at the slopes in Fig. 2.12 B2 they confirm a clear trend for gamma radiation to increase the number of single particles and decrease the number of aggregates (this will be further explored in Sec. 2.4.2). The trends in Fig. 2.12 A2 are slightly less clear, but indicate a trend for UV radiation to decrease both the number of single particles and aggregates.

In this study we choose to mainly focus on the effect of gamma radiation, both due to the clarity of the results shown in Fig. 2.12, and since release of gamma radiation is one of the main products when high energy particles interact with

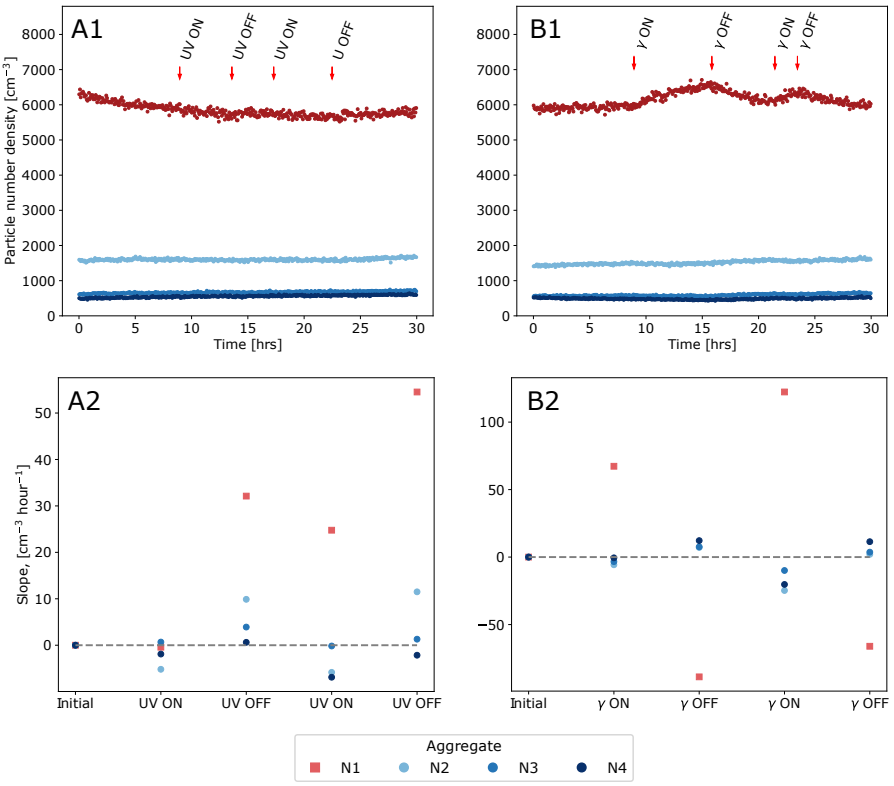

Figure 2.12: Effects of UV radiation (A1 and A2) and gamma radiation (B1 and B2). Top row shows the number densities of the single particles, N1, and each of the aggregated, N2-N4, over time. Arrows indicate the precense or absence or radiation. Bottom rows show the change in number density for each radiation setting shown in the top row (further description in Sec. 2.4.2).

the upper atmosphere (as explained in Sec. 2.5). It would, however, be highly interesting for future studies to look further into the effect of UV on mineral cloud particles.

2.3.4 Testing the loss rate to the chamber walls

Over time, particles will be lost to the chamber walls due to collisions. In order to investigate how many particles are lost to the walls, we study the decrease in particle number density after ending the input of additional particles. The results can be seen in Fig. 2.13.

Fig. 2.13 shows the total decrease in particle number density over a time

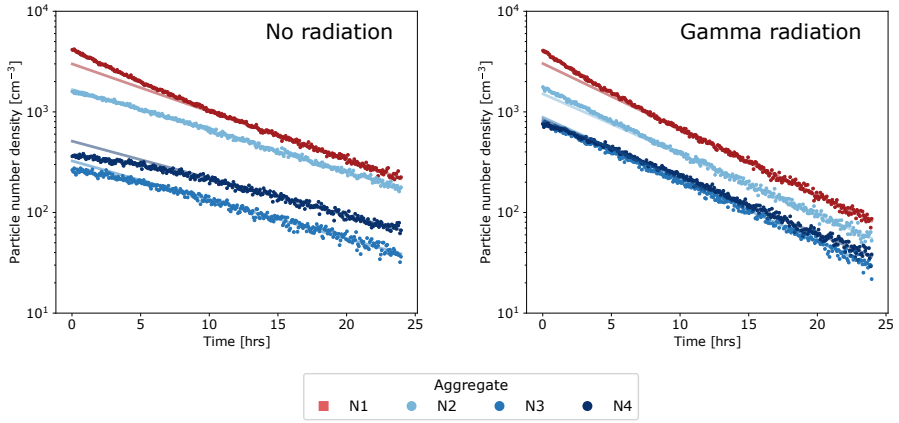

Figure 2.13: Number density of single particles, N1, and each of the aggregates, N2-N4, over time after cutting off the flow of particles into the chamber. Left: The chamber is not irradiated. Right: The chamber is irradiated with gamma radiation. The lines show exponential curves fitted to the data points for the last 10 hours for each of the aggregates.

period of 25 hours after the atomizer has been turned off, for non-irradiated and irradiated particles respectively. The number density of each of the aggregates can decrease due to three processes: 1) Aggregation leads to a decrease of one aggregate population, and an increase of an other population. 2) Particles are lost with the airflow, e.g. to the measurements. 3) Particles collide with the chamber walls and stay there.

If the particles were solely lost to the airflow and the chamber walls, we would expect the decrease to be exponential for each of the aggregates. Exponential curves have been fitted to each of the aggregates for the last 10 hours (hour 15 to 25). The plots in Fig. 2.13 both show that the number density of smaller aggregates (N1 and partly N2) initially decreases faster than exponential, whereas the density of the larger aggregates initially decreases slower than exponential, which confirms that aggregation continues to take place after the input of new particles has stopped. For the last 10 hours, where the exponential curves have been fitted, the aggregates follow these fits with R^2-values of $\geqslant$0.9. Based on the fact that the number densities follow an exponential fit for the last 10 hours, we assume that aggregation is insignificant for this time span. Following this assumption the exponent for the exponential fits should reflect the loss of particles solely due to the airflow and the chamber walls. It should be noted that the input airflow was different for the two cases (13 L/min for the case without radiation and 16 L/min for the case with gamma radiation), leading to the particles being

	Total	Airflow	Chamber walls
No radiation	-0.100	-0.098	-0.002
Gamma radiation	-0.142	-0.120	-0.022

Table 2.3: Loss rates of total number of aggregates in units of hr^{-1} to airflow, chamber walls, and in tota.

diluted faster for the irradiated case.

Given that the exponential loss of particles follow the curve:

$$N(t) = N_0 * exp(-a \cdot t) \tag{2.13}$$

Where N(t) is the particle number density at time, t, and a is the loss rate of the particles. The total loss rate of the particles can be expressed as:

$$a = a_{airflow} + a_{walls} = flow_{air} \cdot V_{chamber}^{-1} + a_{walls} \tag{2.14}$$

The loss rate of particles lost to the airflow ($a_{airflow}$) is found as the total flow of air through the chamber ($flow_{air}$) over the chamber volume ($V_{chamber}$). Values can be seen in Tab. 2.3.

In order to find the total particle loss rate to the chamber walls, the particle number densities shown in Fig. 2.13 have been summed up to find the total number density in the chamber (N1+N2+N3+N4). Exponential curves were fitted to the last 10 hours similarly to what is shown in Fig. 2.13, and the loss rates to the chamber walls was found from the exponent and the loss rate to the airflow.

2.4 Aggregation and charging under high-energy irradiation

In this section, we present the results from the publication Bach-Møller et al. (2024) on the "*Aggregation and charging of mineral cloud particles under high-energy irradiation*". This study used the experimental setup described in the previous section to explore the effect of gamma radiation on SiO_2 particles with diameter of d $\approx$ 50 nm. This section is highly adapted from the publication Bach-Møller et al. (2024). The contributions to this work have been as listed at the beginning of the chapter.

2.4.1 Methods

The experimental setup used in this study is described in Sec. 2.2 and shown in Fig. 2.1, and consists of an aerosol production setup, a chamber that can be irradiated with gamma radiation, and an SMPS system for measurements. A single experiment in this study consists of 50 individual size distribution measurements, each with a scan time of 240 s, taken consecutively, corresponding to a total of $\sim$3.5 hours of measurements for each experiment. The sample used is MSP NanoSilica™; an aqueous suspension of amorphous SiO_2 particles with a highly uniform size distribution around diameters of 50 nm.

The specific settings used for the experiments in this study can be seen in Tab. 2.4. Here we list the universal setting used for all experiments, as well as specific settings for individual experiments. Some of the differences between the experiments include:

- Low humidity (Nr. 1-10) and high humidity (Nr. 11-19) environments.
- Positively (Nr. 1-4, 11-14, and 19) and negatively (Nr. 5-10 and 15-18) charged particles.
- With and without gamma radiation.
- With and without the bipolar charger (to allow for charging state calculations, as described in Sec. 2.2.4).

Many experiments are repeated, as can be seen in the rightmost column, and the results of these experiments will generally be shown as averages, as explained

Universal settings for all experiment	
Scan up time	180 s
Scan down time	60 s
Sheath flow	3 L/min
CPC flow	0.3 L/min
Multiple charge correction	ON
Particle number density in atomizer	$\sim 7 \cdot 10^9$ mL^{-1}
Particle number density in chamber	$\sim 7 \cdot 10^3$ cm^{-3}
Total N_2 flow to chamber	16 L/min

Specific settings for each experiment

Nr.[a]	Charge[b]	Gamma[c]	Bipolar charger[d]	RH	Duration[e]	Repetitions[f]
1	Pos	No	Yes	$\sim$ 20%	3.5	6
2	Pos	No	No	$\sim$ 20%	3.5	6
3	Pos	Yes	Yes	$\sim$ 20%	3.5	6
4	Pos	Yes	No	$\sim$ 20%	3.5	6
5	Neg	No	Yes	$\sim$ 20%	3.5	6
6	Neg	No	No	$\sim$ 20%	3.5	6
7	Neg	Yes	Yes	$\sim$ 20%	3.5	6
8	Neg	Yes	No	$\sim$ 20%	3.5	6
9	Neg	No	Yes	$\sim$ 20%	20	1
10	Neg	Yes/No	Yes	$\sim$ 20%	30	1
11	Pos	No	Yes	$\sim$ 65%	3.5	3
12	Pos	No	No	$\sim$ 65%	3.5	3
13	Pos	Yes	Yes	$\sim$ 65%	3.5	3
14	Pos	Yes	No	$\sim$ 65%	3.5	3
15	Neg	No	Yes	$\sim$ 65%	3.5	3
16	Neg	No	No	$\sim$ 65%	3.5	3
17	Neg	Yes	Yes	$\sim$ 65%	3.5	3
18	Neg	Yes	No	$\sim$ 65%	3.5	3
19	Pos	Yes/No	Yes	$\sim$ 50%	22	1

[a] Identifier for type of experiment.
[b] Electric charge of measured particles.
[c] Irradiation with gamma radiation.
[d] Specifies whether measurements were done with the bipolar charger (yes) or the dummy (no)
[e] Total duration of each experiment in hours.
[f] Number of repetitions of experiments with these settings.

Table 2.4: Settings for experiments. Top part shows universal settings for all experiments. Bottom part shows experiment-specific settings for low-humidity (Nr. 1-10) and high-humidity (Nr. 11-19) environments respectively.

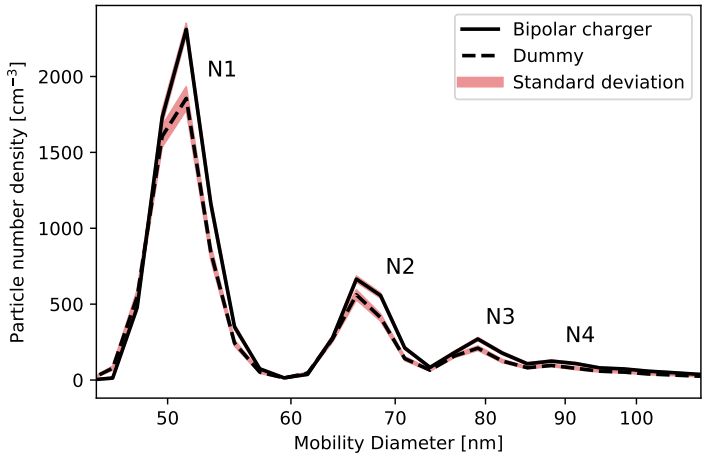

Figure 2.14: Size distribution of negatively charged particles measured with and without bipolar charger. Red shading indicates standard deviation among the 50 measurements constituting each experiment. Shows one repetition of experiment nr. 5 and 6 in Tab. 2.4.

in Sec.2.2.4. Most experiments are of a duration of 3.5 hours in accordance with the scan time, but some are of a longer duration to observe changes over time.

2.4.2 Results

In this section we show the results for the charging state and aggregation of positively and negatively charged particles respectively. The results have been obtained through a number of repeated experiments, all listed in Tab. 2.4. The results presented in Sec. 2.4.2 - 2.4.2 are all done in low humidity environments (RH $\approx$ 20%), whereas the experiments in Sec. 2.4.2 are done at higher humidity (RH $>$ 50%).

Size distribution

An example of the size distributions measured by the SMPS has previously been shown in Fig. 2.5 that shows non-irradiated negatively charged particles (experiment Nr. 5 in Tab. 2.4). The same size distribution can be seen in Fig. 2.14, where the two size distributions show experiments with and without the bipolar charger for the negatively charged particles. Measurements with the bipolar charger illustrate the actual size distribution of the particles, while measurements without the charger (dummy) also reflect the inherent charging of the particles.

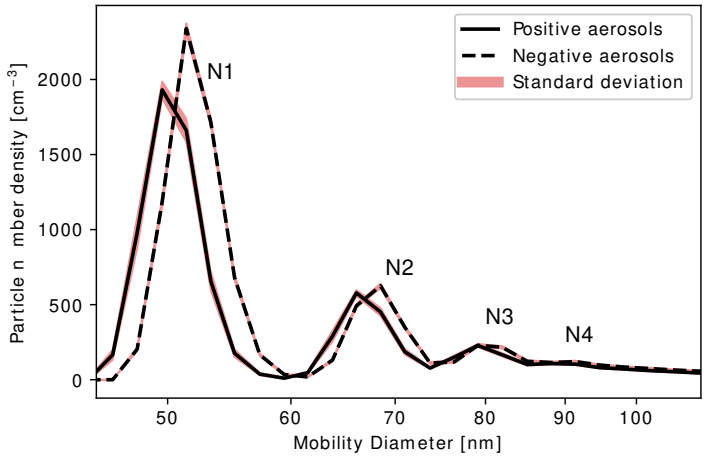

Figure 2.15: Comparison of size distribution of positively and negatively particles respectively. Both measurements are done with the bipolar charger. Red shading indicates standard deviation among the 50 measurements constituting each experiment. Shows one repetition of experiment nr. 5 and 6 in Tab. 2.4.

The size distributions show 3-4 distinct peaks corresponding to the original particles (with diameters of d $\approx$ 50 nm) and aggregates of two, three and four particles (i.e. N1, N2, N3, and N4). The mobility diameters of the aggregates, as shown on the primary axis, do not correspond exactly to physical diameter, but rather describe the mobility of the aggregates through the electric field of the DMA, which depends on the physical diameter as described in Sec. 2.2.3. The plots in Fig. 2.14 and 2.15 show only the relevant mobility diameter range for the SiO_2 aggregates and thereby exclude features at lower mobility diameters caused by e.g. the Milli-Q water. By comparing the distribution with and without the bipolar charger for these peaks we see that more particles are being measured with the charger, indicating that there are fewer negatively charged particles in the population than we would expect from the steady-state bipolar charge distribution. This will be further discussed in Sec. 2.4.2.

The particles get their positive or negative charge from collisions with ions in the gas phase. Since the positive and negative ions can have different mobility (Hõrrak et al., 1998), the ions with the highest mobility will participate in more collisions, which can affect both the number of charged particles and their mobility through the DMA in the SMPS system. Fig. 2.15 illustrates the size distribution of the positively and negatively charged particles respectively. The distributions differ slightly, both in regard to the particle count and the position of

the peaks. The measurements show a higher number of negatively charged particles at around 50 nm. We also see that the distribution for the negatively charged particles is shifted slightly towards higher diameters, indicating that their mobility in the DMA is lower than for the positively charged particles. These differences are not a major concern as charging state calculations are relative.

Aggregation over time

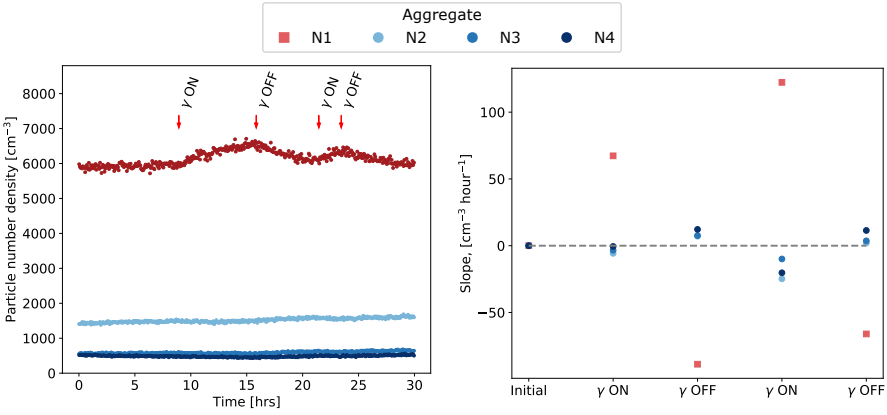

(a) **(b)**

Figure 2.16: Effect of gamma radiation on the aggregation of particles in a low-humidity environment (RH ≈ 20%). a) Number density of single particles, N1, and each of the aggregates, N2-N4, over time . Arrows indicate the presence of absence of gamma radiation. b) The change in number density found as the slope of linear fits for each radiation setting shown in (a) in relation to the initial slope. Each linear fit is started 30 min after the change in radiation (gamma being turned on or off), in order to allow for ionization to take effect, and ended just before the next change. Dashed line at 0.0 indicates no change in particle number. Plots show experiment Nr. 10 in Tab. 2.4

In order to study the effect the gamma radiation on the aggregation of the particles, we looked at the change in the production rate of the aggregates before and after gamma radiation was introduced. The plots shown in Fig. 2.16 show the same particle number densities and slopes as Fig. 2.12. As noticed previously there is a clear trend for gamma radiation to cause an increase in the number of single particles (N1) and a decrease in the number of aggregates (N2-N4), as indicated by positive and negative slopes respectively in Fig. 2.16b. Similarly, turning the gamma radiation off caused a decrease in the number of single particles (N1) and an increase in the number of aggregates (N2-N4). This indicates that gamma

radiation inhibits the aggregation of the particles.

Charging state

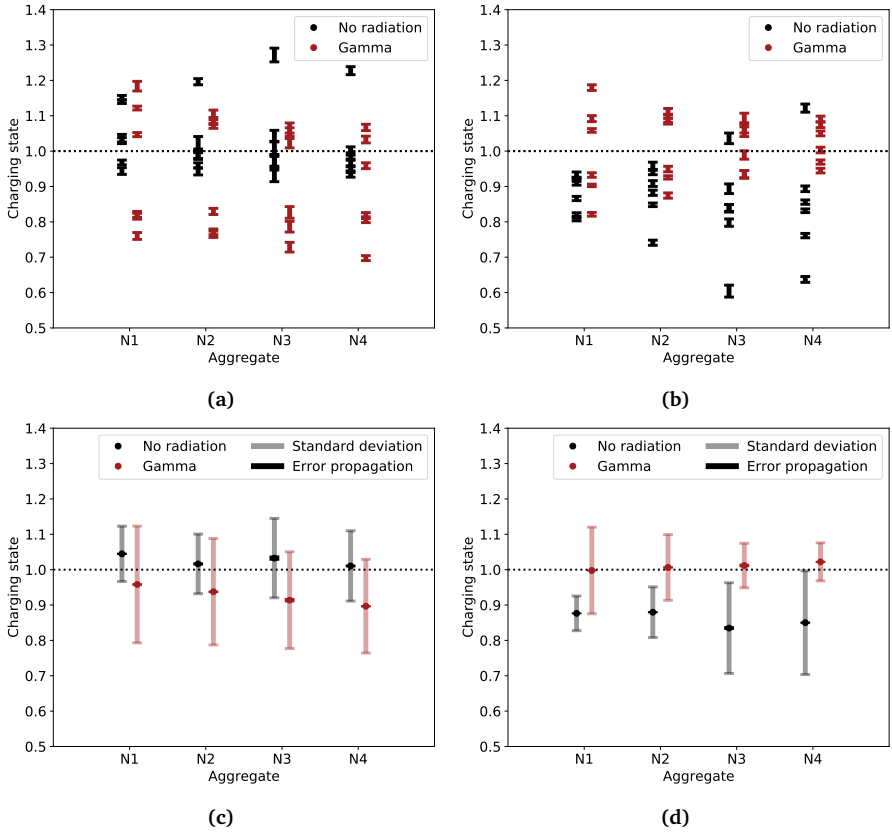

Figure 2.17: Charging state of positively (left) and negatively (right) charged particles. (a) and (b) show charging state of all repeated experiments with error bars indicating propagated errors. (c) and (d) show average charging states for each aggregate, with dark error bars indicating propagated errors (notice that they are so small that they fit within the data points), and light error bars indicating standard deviation among repeated experiments. Horizontal dotted line at 1.0 indicates bipolar charge distribution. Show experiments nr. 1-8 in Tab. 2.4

As explained in Sec. 2.2.3 the charging state is a measure of the fraction of charged particles in the population compared to the fraction of charged particles in a steady-state bipolar distribution. As such the charging state indicates the charging relative to a standard distribution, and potential changes in the charging state due to irradiation with gamma radiation can indicate how high-energy

radiation affects the overall charging of the particle population.

Fig. 2.17 shows the charging state, individually and averaged, of all experiments of positively and negatively charged particles respectively. Each plot shows the charging state for both non-irradiated particles, and particles irradiated with gamma radiation. The experiments plotted are listed in Tab. 2.4. Experiments with and without bipolar charger are done consecutively, and charging states are calculated for each pair. A total of six individual charging state measurements are plotted in Figs. 2.17a and 2.17b and used to find each average shown in Figs. 2.17c and 2.17d.

For the non-irradiated case, the positively charged particles in Fig. 2.17c have charging states just above the steady-state distribution, as illustrated by the horizontal dotted line. This corresponds to a slight overcharging of the particles, and indicates that there are more positively charged particles than expected from the steady-state distribution. Gamma radiation decreases the number of positively charged particles, thereby lowering the charging state, resulting in the particle population becoming undercharged compared to the steady-state distribution.

For the non-irradiated case, the negatively charged particles in Fig. 2.17d generally have charging states below the horizontal line, indicating a lack of negatively charged particles in the population compared to the steady-state distribution. Gamma radiation increases the number of negatively charged particles, bringing the charging state close to the steady-state distribution.

Both plots' averages in Fig. 2.17 indicate a shift towards more negatively charged particles in the population as a result of the gamma radiation.

Statistical T-test of charging states

In order to test the effect of gamma radiation on the particles we compare the mean charging state of irradiated and non-irradiated particles. Since the test needed would be a comparison of the means of two independent samples, an independent T-test was chosen. The test was performed for positively and negatively charged particles separately, and the samples tested correspond to the data plotted in Fig. 2.17 (a) and (b).

The probability values (p-values) from the T-test are shown in Tab. 2.5. For the positively charged particles we find p-values that are all outside the a significance level of 5% (i.e. all p-values are above 0.05). For the negatively charged particles,

	N1	N2	N3	N4
Positively charged	0.31	0.33	0.16	0.16
Negatively charged	0.07	0.04	0.02	0.03

Table 2.5: P-values for t-test of two independent samples comparing irradiated and non-irradiated particles. Low-humidity environment, Fig. 2.17.

most of the aggregates have p-values within a significance level of 5%, the only exception from this is the N1 particles showing a p-value of 7%. These results indicate that the effect of gamma radiation seen for the average charging states shown in Fig. 2.17 is statistically significant for the negatively charged particles (d), but not for the positively charged particles (c).

Relative humidity

As mentioned in Sec. 2.2 the lowest relative humidity reached in the chamber was RH $\approx$ 20%, and all measurements in the previous sections were done at this RH value. In order to test the effect of relative humidity on the aggregation and charging of the particles a set of experiments were repeated at higher relative humidities with RH $>$ 50%. The experimental settings can be seen in Tab. 2.4 (nr. 11-19), and the results are shown in Fig. 2.18. The top row of the figure, (a and b), shows that gamma radiation also inhibits the aggregation of the particles in a high-humidity environment, similarly to the low humidity cases in Fig. 2.16. Fig. 2.18a, show a trend of an increase in the number of N1 particles under irradiation with gamma, similarly to what was seen for the low-humidity case. The changes observed for the N1 particles shown in Fig. 2.18b are even more pronounced than those seen for the low-humidity case in Fig. 2.16b, with average changes in slopes of $\sim$250 $\pm$ 60 cm^{-3}hr^{-1} in high humidity compared to $\sim$170 $\pm$ 20 cm^{-3}hr^{-1} in low humidity. The trend for the aggregates (N2-N4) is less clear in this high-humidity case compared to the low-humidity. The bottom row of Fig. 2.18, (c and d), show the average charging states of positively and negatively charged particles respectively, corresponding to the low-humidity cases, Fig. 2.17c and Fig. 2.17d. The positively charged particles in Fig. 2.18c show a general trend for the irradiated particles to be more undercharged than the non-irradiated particles. This indicates that the number of positively charged particles decreases under gamma radiation. The opposite trend is seen for the negatively charged particles in Fig. 2.18d, where the irradiated particles are significantly more overcharged compared to the non-irradiated particles indicating an increase in the number of negatively charged particles under gamma radiation. Both these trends are similar

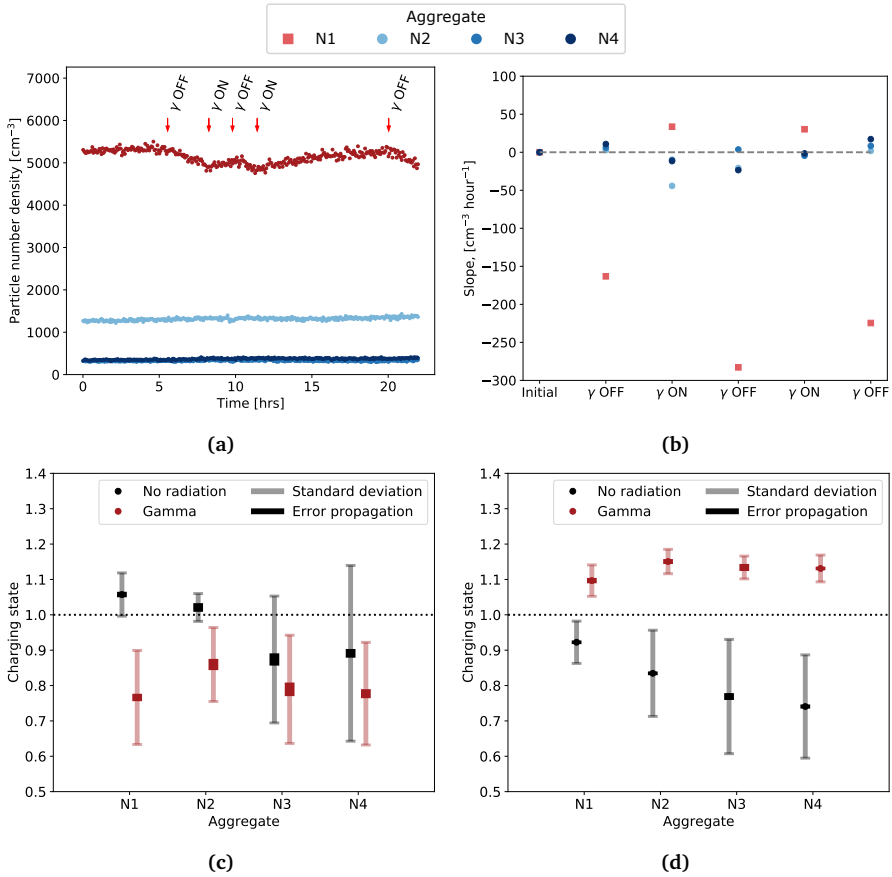

Figure 2.18: Experiments conducted in a high humidity environment (RH $>$ 50%). Top: Number densities of aggregates over time. The change in density caused by gamma radiation is shown in (b) as slopes from linear fits for the different radiation settings as marked by arrows in (a). Experiment nr. 19 in Tab. 2.4. Bottom: Average of the charging states calculated for each of the repeated experiments (nr. 11-18 in Tab. 2.4). (c) shows the positively charged particles, and (d) shows the negatively charged particles. Dark error bars indicate propagated errors (notice that they are so small that they often fit within the data points), and light error bars indicate standard deviation among repeated experiments.

to what was seen in the low-humidity environment, where gamma radiation was observed to shift the particles population towards a more negative charge.

To test the statistical significance of the effect of gamma radiation on the charging state in a high-humidity environment a T-test was performed, and the resulting p-values can be seen in Tab. 2.6. For the positively charged particles it is found that the effect of gamma radiation is not statistically significant for most of the

	N1	N2	N3	N4
Positively charged	0.05	0.11	0.64	0.60
Negatively charged	0.03	0.02	0.04	0.02

Table 2.6: P-values for t-test of two independent samples comparing irradiated and non-irradiated particles. High-humidity environment, Fig. 2.18 (c) and (d).

aggregates (the exception being the N1 particles). For the negatively charged particles it is found that the effect of gamma radiation is statistically significant for all aggregates, with p-values that are well within the 5% significance level. The fact that the changes caused by gamma radiation are more statistically significant in the high-humidity environment, could indicate that the increase in the number of negatively charged particles is more pronounced at higher humidity.

2.5 Discussion

If we wish to understand exoplanets in different planetary systems it is important to understand how the radiation field of the host star influences the exoplanet atmospheres. Here high-energy radiation plays an important role.

The radiation environment caused by the host star and galactic environment has been found to have an impact on both chemistry and climate of exoplanets (reviewed by e.g. Airapetian et al. (2020)). High-energy particles, such and cosmic rays and SEPs, have been found to affect both the chemical composition (Barth et al., 2021) and ionization (Rodríguez-Barrera et al., 2018) of the atmospheres. Due to the importance of ionization and charging in ion-induced nucleation (Wagner et al., 2017), high-energetic particles might play a significant role in cloud formation in environments with low presence of primary aerosols (Jokinen et al., 2018), such as gas planets.

The majority of all stars in the Milky Way are M-dwarfs, and given our current observation biases, these make for interesting targets for transit observations of exoplanets in the habitable zone (Mesquita et al., 2021a). Due to the low luminosity of M-dwarfs their habitable zone is very close to the star (Kasting et al., 1993; Selsis et al., 2007), which allows for smaller planets to be observable in the habitable zone. M-dwarfs have been found to remain magnetically active for longer than Sun-like stars (West et al., 2004; Scalo et al., 2007; Guinan et al., 2016), which creates a very different radiative environment than in the Solar System. The high activity causes the stars to have stronger flares (Vida et al., 2017; Tilley et al., 2019), and release more stellar energetic particles and gamma radiation

(Grießmeier et al., 2005; Obridko et al., 2020; Sadovski et al., 2018; Fraschetti et al., 2019). Exoplanets in these systems might therefore be exposed to a higher degree of high-energy radiation from the host star, both due to the higher activity and due to the potentially closer proximity to the star.

The exact correlation between the activity of the host star and the total influx of high energy radiation to an exoplanet is, however, nontrivial. While the particle influx from the star itself increases with stellar activity, the corresponding increase in magnetic flux and stellar wind has also been found to shield the system from the influx of GCR from outside the system (Mesquita et al. (2021a,b); Nandy et al. (2021), and reviewed in e.g. Potgieter (2013)). The nature of the high-energy particles in a system will therefore change depending on the activity of the host star during its evolutionary phases, such that SEPs might be dominating during the younger active phase of the star, while GCRs will be dominating later in the evolution or for less active stars (Rodgers-Lee et al., 2021a).

In this study we imitate the high-energy radiation of SEPs and GCRs with gamma radiation, similarly to what has been done previously (Enghoff & Svensmark, 2017). Gamma radiation is one of the products released in the interaction between SEPs and GCRs and celestial atmospheres, and high-energy particles will therefore release gamma radiation both from the host star and from the atmosphere of the planet itself, making the Earth atmosphere a bright source of gamma radiation (as reviewed by e.g. Mazziotta et al. (2020) and Dean et al. (1988)). The Cs-137 sources used in this study release gamma radiation with energies of 0.66 MeV which lies within the energy range of SEPs and low-energy GCRs (e.g. Barth et al. (2021)) as well as the range of cosmic ray showers caused by higher energy GCRs. The duration of each experiment has been determined by the scan times and number of desired consecutive measurements, and the chamber has therefore been irradiated with gamma radiation for periods of $\sim$4 hours at a time. This is longer than the average SEP event, but still lies well within the general time scales from minutes to hours (e.g. Firoz et al. (2022); Doyle et al. (2018); Reep & Knizhnik (2019)),while the influx of GCRs is more continuous. It should be noted that studies have found that in the case of ion-induced nucleation the nature of the ionizing radiation is not important as long as the ionizing effect is the same (Enghoff et al., 2011).

The aim of this paper has been to study how the aggregation and charging of mineral cloud particles are affected by high-energy radiation and humidity.

Using experiments with SiO_2 particles in an atmosphere chamber we observed two trends: 1) gamma radiation inhibits the aggregation of the particles, and 2) gamma radiation causes a higher number of particles to become negatively charged. These trends, of less aggregation and more negative charge, are observed both in environments with lower relative humidity (RH $\approx$ 20%) and higher relative humidity (RH $>$ 50%).

The coupling between the effects of gamma radiation (i.e. the inhibited aggregation and the negative charge of the particles) is uncertain, but it might be related to a change in the mobility of the particles. As can be seen from Fig. 2.15, the mobility size of the negatively charged particles is slightly larger than for the positively charged particles. As the mobility diameter is linked to the size of the particles, as described in Sec. 2.2, this indicates a slight difference in the size of the positively and negatively charged particles with the negatively charged particles being larger. Since the gamma radiation leads to an increase in the number of negatively charged particles it leads to an overall increase in particle size in the chamber. At these particle sizes the coagulation coefficient between similar sized particles decreases with increasing particles size (Fujimoto et al., 2021; Fuchs et al., 1965) leading to fewer collisions overall in the chamber. Thus the decrease in aggregation might be linked to a decrease in the number of collisions caused by a lower mobility of the negatively charged particles. It is uncertain what causes the difference in mobility diameter between negatively and positively charged particles in this study.

The effect of gamma radiation on the charging state, as shown in Fig. 2.17 and 2.18, indicates that gamma radiation causes a decrease in the charging state for positively charged particles and an increase for negatively charged particles for both the low-humidity and high-humidity case. However, this change is only found to be statistically significant for the negatively charged particles and not the positively charged particles. It is yet unknown whether the decrease in the number of positively charged particles would get more statistically significant with more repetitions of the experiments, or it is caused by an actual physical process allowing the particles to maintain their positive charge under gamma radiation.

The overall negative charging of the particles might be linked to the mobility of the ions created by the gamma radiation. In Earth's atmosphere, high-energy radiation, such as SEPs and GCRs, lead to the formation of ions and ionic clusters through the separation of electrons from N_2 or O_2, that will subsequently be cap-

tured by neutral molecules (reviewed in Harrison & Carslaw (2003)). Depending on the composition of these ions, they will have different mobility and thereby different rate of uptake by aerosols. In Earth's troposphere, the negative ions generally have higher mobilities than the positive (e.g. Hõrrak et al. (1998); Harrison & Carslaw (2003)), and some of the dominating negative ions are $O_2^-(H_2O)_n$ and $NO_3^-(H_2O)_n$, while some of the dominating positive ions are $H_3O^+(H_2O)_n$, $H^+(H_2O)_n$, and $NO^+(H_2O)_n$. Most of these ions could also be present in our experiments, since they can be formed through ionisation of N_2 and H_2O (the gas composition used in this study), and the Cs-137 gamma sources we use can ionize both N_2 and H_2O. This could indicate that we might also expect a higher mobility of the negative compared to the positive ions in our setup, similar to what is seen in Earth's atmosphere. A noticeable difference between the gas composition in this study and Earth's atmospheric composition is the lack of O_2 in the chamber. A previous study by (Wiedensohler et al., 1986), looked at the charging distribution of positively and negatively charged particles in different gas composition. They found a larger split in the charging state of positively and negatively charged particles in N_2 gas compared to air, with a significantly higher number of negatively charged particles. They suggest that this might be due to the lack of O_2 since this results in a lack of electron receptors, leading to more free electrons and thereby potentially a higher average mobility of all negative ions. Exactly how the number and mobility of the small air ions will affect the final charging of particles is non-trivial, and depends on a series of chemical and ion exchange reactions where ion clusters build up before they collide with and are absorbed by the larger particles (Harrison & Carslaw, 2003). But as observed by Wiedensohler et al. (1986) the initial composition of air ions can affect the final charging.

Different degrees of relative humidity were tested in this study, and as mentioned, gamma radiation is shown to have a similar effect on the SiO_2 particles in low- and high-humidity environments. Previous studies have suggested that water molecules structure themselves differently on silicates, depending on the relative humidity of the environment (Asay & Kim, 2005). Based on the terminology from Asay & Kim (2005), the two humidity ranges we are observing lead to structures that are ice-like (RH $= \sim 20\%$) and transitional/liquid (RH $> 50\%$) respectively. The fact that we observe similar effects of gamma radiation in the two cases, could indicate that the charging and inhibition of aggregation is not dependent on the structuring of water molecules on the surface of the particles. However, the adhesion of water molecules to solid surfaces (reviewed in e.g. Zhou & Huang (2021);

Sacchi & Tamtögl (2023)), and the resulting effect on charging and aggregation of particles (He et al., 2019, 2020), is complex and depends on both the physical and chemical properties of the surfaces, and we have not accounted for it in this study.

Based on the results of this and previous studies we suggest that high-energy environments might promote the formation of smaller cloud particles. Previous studies have shown that high-energy radiation induces the nucleation of cloud particles in Earth-like atmospheres, thereby increasing the number of new particles (Lee et al., 2019; Wagner et al., 2017; Svensmark et al., 2013). In this study, we show that high-energy radiation may inhibit aggregation of the existing particles, thereby favouring a high number of smaller particles rather than a low number of larger particles. Together this could indicate that high-energy radiation increases the number of particles overall. Under the right conditions, these particles might act directly as cloud particles or potentially as cloud condensation nuclei for other cloud forming species. For Earth, it has been speculated that the required size of a cloud condensation nuclei is 50 nm (e.g. Svensmark et al. (2013); Sarangi et al. (2015); Fan et al. (2018)), and under Earth-like conditions, previous studies (Svensmark et al., 2013) have found that gamma radiation promotes the growth of nucleated particles up to $>$ 50 nm. Since this study has found that gamma radiation inhibits aggregation of d $\approx$ 50 nm particles, this could indicate that high-energy radiation will increase the number of cloud condensation nuclei overall by promoting their formation and preventing the loss in number through aggregation. We note that the studies promoting nucleation and growth of smaller aerosols were performed on a different set of species than in this study.

With telescopes such as James Webb Space Telescope (JWST) our understanding of cloud formation is being put to the test as it becomes essential in our analysis of transit spectra. Already the early release observations from JWST (Pontoppidan et al., 2022) presented planets such as WASP-96b with strong H_2O features, that are also predicted to have mineral cloud particles including silicate species ($\geqslant$40%) (Samra et al., 2023), indicating the relevance of understanding the behaviour of mineral cloud particles in humid environments. The presence of mineral cloud particles is not unusual, and has been observed for e.g. WASP-107b both with Hubble Space Telescope (Kreidberg et al., 2018) and later with JWST (preprint Dyrek et al. (2023)). Another potential JWST target of interest is HD189733b, that is both expected to have silicate cloud particles (Lee et al., 2016; Barth et al., 2021), and where observations have shown flares from the host

star (Bourrier et al., 2020), indicating that an increased level of gamma radiation might be present in the upper atmosphere of the planet. These observations and models all show the importance of understanding the interplay between mineral cloud particles and high-energy radiation.

The results of this study have been primarily qualitative and solely focused on SiO_2 as an analogue to mineral cloud particles. In order to get a better understanding of the behaviour of mineral cloud particles in general, it would be highly beneficial to conduct further extensive studies with more repetitions and other predicted cloud formation species, such as silicate and magnesium species, like enstatite ($MgSiO_3$) and forsterite (Mg_2SiO_4) (e.g. Lunine et al. (1986); Helling et al. (2008b); Carone et al. (2023); Gao & Powell (2021)), or titanium species such as TiO_2 (e.g. Kohn et al. (2021); Helling et al. (2008c)).

2.6 Summary

In this study we have explored the question of how high-energy radiation affects the aggregation and charging of mineral cloud particles. We here present the results of a series of experiments with mineral SiO_2 particles in an atmosphere chamber under varying degrees of high-energy radiation and relative humidity.

Based on the experiments we observe the following:

1. The d $\approx$ 50 nm SiO_2 particles (N1) aggregate in the chamber to form clusters of two, three, and potentially four particles (N2 - N4).

2. Gamma radiation inhibits the overall aggregation of the SiO_2 particles. This is observed as an increase in the number of single particles (N1) and a decrease the number of larger aggregates (N2 - N4). It is unknown if the trend reflects a prevention of the N1 particles to aggregate, or if it reflects a fragmentation of existing aggregates (N2-N4), but it could be linked to a lowered mobility of the N1 particles due to a change in their charging state.

3. Gamma radiation causes the particle population to become more negatively charged. This is observed as an increase in the charging state of the negatively charged particles and a decrease in the charging state of positively charged particles, when gamma radiation is present. This change in charging state is only found to be statistically significant for negatively charged particles.

4. The effect of gamma radiation is visible both at lower ($\sim$20%) and higher ($\geqslant$50%) relative humidity.

We suggest that gamma radiation may favour the formation of many smaller particles based on: 1) previous studies have found that gamma radiation increases ion-induced nucleation, and 2) this study has found that gamma radiation decreases aggregation. Depending on the environment, the many smaller particles might act directly as cloud particles or as cloud condensation nuclei for other cloud forming species.

3

High-energy radiative environments and atmospheric chemistry

- A modelling approach

In this chapter, I present the work done in preparation for a future publication on the effect of the high-energy radiative environment on the complex chemistry of exoplanet atmospheres. This work utilizes a chemical network in combination with a photochemistry and diffusion code to model a test planet in different radiative environments. A great part of the chapter focuses on the preparation of the input files, as this work is relatively novel, and we have had to gather a lot of new material.

The contributions to the work were as follows:

- I (first author) participated in project planning and was primarily respon-

sible for doing background research, preparing the input files, running the models, and data analysis, and I have done all writing for this chapter.

- Christiane Helling, Uffe Gråe Jørgensen, and Martin Bødker Enghoff participated in project planning, discussions, and data analysis.
- David Lewis, Patrick Barth, Lidia M. Oskinova, Luca Fossati, and Fernando Cruz Aguirre have provided data for input files, guidance, and discussion.

3.1 Background and Aim

When we observe exoplanet atmospheres, we are limited to information that can be gained from the emission or absorption of light in the upper parts of the atmosphere. Our observations are therefore greatly affected by the chemistry of the upper layers of the atmosphere and any processes that target these parts. The upper part of the atmosphere is also the part that is most exposed to external radiation. Understanding the effect of radiation is therefore crucial for understanding our observations and what they can tell us about the deeper atmosphere.

As we have explained in previous chapters, high-energy radiation is known to have a significant effect on exoplanet atmospheres, both with regard to the temperature structure (Sinnhuber et al., 2012), global electric circuit (Rycroft & Harrison, 2012), mass loss (Murray-Clay et al., 2009), cloud formation (Svensmark, 2006; Enghoff & Svensmark, 2017; Bach-Møller et al., 2024), and gas phase chemistry (e.g. Barth et al. (2021); Miguel & Kaltenegger (2013); Linsky et al. (2014). As described in detail in Sec. 1.3, the main sources of high-energy radiation entering the atmosphere are XUV radiation and stellar energetic particles from the host star, as well as galactic cosmic rays from outside the system.

XUV radiation is known to impact planetary atmospheres through the ionization and heating of the upper atmosphere, as well as driving photo chemistry and mass loss (e.g. Linsky (2014); Johnstone (2016)). Since XUV radiation can vary significantly for different stellar types, this can lead to very different environments for exoplanets depending on their host star. The effect of photochemistry on exoplanet atmospheres has been studied for different host stellar types by Baeyens et al. (2021, 2022). Using a GCM in combination with a pseudo-2D chemical kinetics code, Baeyens et al. (2021) built a grid of models for tidally locked exoplanet atmospheres with different effective temperatures and host stellar types (M-, K-, G-, and F-type stars). Baeyens et al. (2022) built upon this grid by in-

corporating photochemical reactions, and find that photochemistry can strongly change the chemical composition of atmosphere down to atmospheric layers of several bars. They find that the products of these photochemical reactions can be transported all the way to the night-side of the planet, and therefore also affect the terminator regions that are targets for transmission spectroscopy observations.

As reviewed in Sec. 1.3, while radiation in the UV, visible, and IR wavelength is dependent on the temperature of the stellar photosphere and thereby the stellar mass, radiation in the FUV, EUV, and X-ray is dependent on the heating of the chromosphere and corona, which is believed to be linked to the magnetic activity of the host star (reviewed by Johnstone (2016)). Magnetic activity is generally found to be higher in low mass stars, due to there deep outer convective zone longer rotational breaking (e.g. Berdyugina (2005); Bouvier et al. (2014); Astudillo-Defru et al. (2017). Studies have found that the thickness of the outer convective zone decreases with increasing temperature, until in completely disappears for temperatures above $\sim$ 8500 K Bohn (1984); Christensen-Dalsgaard & Aguirre (2018); Kupka & Montgomery (2002). Both factors lead to higher magnetic activity and stronger X-ray emission for low mass stars, while the more massive F-, A-, and B-type are weak X-ray sources. The exception for this trend is the O-type stars, which are X-ray sources due emission from perturbations in their strong stellar winds Oskinova et al. (2006).

The host star can also effect the atmosphere through the emission of stellar energetic particles (SEP). As shown by previous studies, such as (Barth et al., 2021), SEP can significantly alter the concentrations of complex organic molecules in the atmosphere, and can in some layers of the atmosphere act as the primary source of ionization. As described in Sec. 1.3.1 SEP are released during magnetic activity events such as stellar flares and CMEs, and the SEP flux will therefore also depend on the stellar type.

As explained in 1.4, galactic cosmic ray from outside the system can also have a significant effect on the atmosphere. In addition to the effect on nucleation and cloud formation explored in Chapter 2, GCR are known to be one of the primary sources of ionization on Earth in the lower atmosphere at altitudes from 3 to 60 km. Due to the high energy of GCR, the energetic particles can penetrate deeper into the atmosphere than their stellar counterparts. Alternatively, they can react with the gas of the upper atmosphere creating cascades of ionizing radiation that

propagates through the atmospheric column (reviewed in e.g. Mironova et al. (2015)). This causes the ionizing effect of GCR to peak at lower altitudes where the ionization can, for example, lead to the formation of ion clusters of $H^+(H_2O)_n$.

Since the influx of high-energy radiation can change drastically depending on the host star and surrounding galactic environment, it needs to be included in our models and taken into consideration when we analyse the observations of exoplanet atmospheres.

As described in detail in Sec. 1.4, a lot of work has already been done to understand the effect of high-energy radiation on exoplanet atmospheres. The focus of most of these previous studies has been M-, K-, and G-type stars, due to their majority in the stellar population, known magnetic activities, and potential for habitability. In addition to this many previous studies focusing on SEP and GCR have been centered around individual case studies, and as such much of the parameter space for XUV, SEP, and GCR is still unexplored.

In this work we wish to expand on the previous studies by exploring the full range of potential radiative environments exoplanets might be found in. We utilize a photochemistry and diffusion code in combination with a chemical kinetics network to model the chemical composition of a hot-Jupiter under a varying irradiation by XUV radiation, SEP, and GCRs.

In Sec. 3.2 we describe our modelling approach as well as some of the required input files. In Sec. 3.4 we go through the preparation of the input files for the different radiative environments. In Sec. 3.4 we present the results of a series of models for different radiative inputs. In Sec. 3.5 the methods are discussed. Finally in Sec. 3.6 we summarize our findings.

3.2 Modelling approach

In this study we model exoplanet atmospheres using the 1D photochemistry and diffusion code, `ARGO`, in combination with the chemical kinetics network `STAND2020`. In this section, I will describe our modelling approach as well as how to prepare some of the specific input files related to high-energy radiation.

3.2.1 Photochemistry/diffusion code, ARGO

ARGO was developed by Rimmer & Helling (2016a) as a one-dimensional photochemistry and diffusion code with the purpose of running the chemical network STAND2015 (the precusor to STAND2020) in a stepwise manner for each layer in an atmospheric column. ARGO is based on the numerical code NAHOON (Wakelam et al., 2012), that computes the chemical evolution of a medium in a pseudo time-dependent manner by solving a set of differential equations for a chosen chemical network. ARGO differs from NAHOON by including wavelength-dependent photochemistry, cosmic-ray transport, condensation, and chemical mixing. ARGO operates by developing a gas parcel from its initial conditions at the bottom of the atmosphere as it moves up and down through the layers of the atmospheric column. Each of these cycles up and down through the atmosphere is called a *global run*. For each atmospheric layer, ARGO runs two sets of calculations: it (1) solves the chemical transport, and 2) calculates the rate constants for reactions induced by photochemistry and cosmic rays.

Chemical transport

The chemical transport is modelled by solvingthe continuity equations for each chemical species (i) of the atmosphere:

$$\frac{\partial n_i}{\partial t} = P_i - L_i - \frac{\partial \Phi_i}{\partial z} \tag{3.1}$$

where n_i is the number density, P_i is the production rate, and L_i is the loss rate. The last term describes the vertical change in the flux (Φ_i) represented both by Eddy and molecular diffusion. The molecular diffusion coefficients are determined by the Chapman–Enskog theory (Enskog, 1917; Chapman & Cowling, 1990). The Eddy diffusion coefficients are given as an input for the specific planet being modelled and are either determined empirically or derived by GCMs. The production and loss rates in the continuity equations are calculated using STAND2020, which will be described in further detail in Sec. 3.2.2.

Chemical rate constants for photoionization and cosmic rays

After the first global run through the atmosphere, the XUV flux and cosmic ray ionization are introduced into the model. This is done by computing the direct and approximate diffusive actinic flux for different altitudes in the atmosphere

(z).

$$F(\lambda, z) = F(\lambda, z_{\text{top}}) e^{-\tau(\lambda,z)/\mu_0} + F_{\text{diff}} \tag{3.2}$$

where $F(\lambda, z_{\text{top}})$ is the actinic flux spectrum for the specific host star given as a model input, $\tau(\lambda, z)$ is the total optical depth taking into account the photoabsorption and Rayleigh scattering, and F_{diff} is the actinic flux of the diffusive radiation calculated by the δ-Eddington two-stream approximation.

The effect of XUV radiation on the atmospheric chemistry is calculated based on the actinic flux as the rate constants $k_{ph,i}$:

$$k_{ph,i}(z) = t_f \int_{1\text{Å}}^{10^4\text{Å}} \sigma_i F(\lambda, z) d\lambda \tag{3.3}$$

where i is indexed over the molecules for which photochemistry is considered, σ_i is the cross section of species i, and t_f is the fraction of time over which the atmosphere is irradiated.

The effect of galactic cosmic rays (GCR) is implemented as the ionization parameter, ζ. This parameter reflects both the direct ionization by the cosmic rays and the secondary ionization caused by air showers as cosmic rays interact with the atmosphere and generate cascades of subatomic particles and electromagnetic radiation.

The actual chemical ionization rate depends on the atmospheric composition, as different species have different cross sections for photons released by the cosmic rays. The chemical rate constant for cosmic rays $k_{CR,i}$ is therefore found as:

$$k_{CR,i}(z) = \kappa_{CR,i} \zeta(z) \tag{3.4}$$

where the constant $\kappa_{CR,i}$ is specific for the specific atmospheric species.

ARGO treats low-energy cosmic rays (LECR, E $<$ 1GeV) and high-energy cosmic rays (HECR, E $>$ 1GeV) separately. The low energy cosmic rays are implemented based on Rimmer & Helling (2013) that assumes that the LECR flux density reaching the planet follows a broken power law spectrum (Indriolo et al., 2009):

$$j(E) = \begin{cases} j(E_1) \left(\frac{p(E)}{p(E_1)}\right)^{\gamma} & if\, E > E_2 \\ j(E_1) \left(\frac{p(E_2)}{p(E_1)}\right)^{\gamma} \left(\frac{p(E)}{p(E_2)}\right)^{\alpha} & if\, E_{cut} < E < E_2 \\ 0 & if\, E < E_{cut} \end{cases} \tag{3.5}$$

where $p(E) = \frac{1}{c}\sqrt{E^2 + 2EE_0}$. Here E_0 is the proton rest energy ($E_0 = 9.38 \cdot 10^8$ eV), and E_1 and E_2 and constants determined by the observed shape of the power law (Indriolo et al., 2009) ($E_1 = 10^9$ eV and $E_2 = 2 \cdot 10^8$ eV). $j(E_1)$ is the measured cosmic ray flux at 10^9 eV ($j(E_1) = 0.22$ cm^{-2} s^{-1} sr^{-1} (10^9 eV nucleon^{-1})$^{-1}$). γ and α are both fitting parameters, where the first is well-constrained by observations Mori (1997) ($\gamma \approx$ -1.35) while the second is chosen based on its agreement with the CR ionization in the ISM (Indriolo et al., 2007) ($\alpha =$ -2.15). E_{cut} is the low-energy cut-off and is set to $E_{cut} = 10^6$ eV, since GCR with energies lower than this have been found to not travel further from their source than $\sim$ 1 pc (Rimmer et al., 2012; Rimmer & Helling, 2013).

Based on these LECR fluxes, ionization of the atmospheric column was simulated through Monte Carlo simulations (Rimmer & Helling, 2013). The resulting ionization parameter ζ is determined based on the column density N_{col} [cm^{-2}] as:

$$\zeta_{GCR}(N_{col}) = \zeta_{GCR,0} \times \begin{cases} 480 & if\, N_{col} < N_1 \\ 1 + (N_0/N_{col})^{1.2} & if\, N_1 < N_{col} < N_2 \\ exp(-kN_{col}) & if\, N_{col} > N_2 \end{cases} \tag{3.6}$$

where ζ_0 is the standard ionization rate in a dense interstellar medium ($\zeta_0 = 10^{-17}$s^{-1}), and the column densities $N_0 = 7.85 \cdot 10^{21}$cm^{-2}, $N_1 = 4.6 \cdot 10^{19}$cm^{-2}, and $N_2 = 5.0 \cdot 10^{23}$cm^{-2}, and the constant $k = 1.7 \cdot 10^{-26}$ cm^2 are fitting parameters.

3.2.2 Chemical kinetics network, STAND2020

The production and loss rates (P_i and L_i) in Eq. 3.1 are calculated by calling the chemical kinetics network STAND2020. STAND2020 is an updated version of the chemical network STAND2015 Rimmer & Helling (2016a,b); Rimmer & Rugheimer (2019) that now contains more than 6000 reactions involving 327 atmospheric species. It is an H/C/N/O network that covers all reactions for species with up to six H, two C, two N, and three O atoms (for which reaction rates have been published), and it also includes a smaller number of reactions with He, Na, Mg, Si, Ar, K, Ti, and Fe, as well as ions for these. It is valid for temperatures between 100 and 30.000K and has been tested against modern Earth and Jupiter (Rimmer & Helling, 2016a), and validated against other models with hot-Jupiters

(Barth et al., 2021; Hobbs et al., 2021; Tsai et al., 2023, 2017; Hobbs et al., 2019).

The network consists of a list of rate constants for each reaction that have been obtained from databases such as the NIST Chemical Kinetics Database (Manion et al., 2013) and the KIDA database Wakelam et al. (2012), and publications such as Ikezoe et al. (1987); Sander et al. (2011) and Harada et al. (2010). Depending on the reaction, the rate constants can be of zeroth (e.g. source terms S_i), first (k_1, interactions between species i and particles not included in the network, such as photons and cosmic rays), second (k_2, interactions between species i and j of the network), or third order (k_3, interactions between species i and j of the network and a third body). By combining all reaction rates for each species, the production and loss rates for species i can be found as follows:

$$P_i = S_i + \sum k_1 n_j + \sum k_2 n_j n_k + \sum k_3 n_{gas} n_j n_k \tag{3.7}$$

$$L_i = \sum k_1 n_i + \sum k_2 n_i n_j + \sum k_3 n_{gas} n_i n_j \tag{3.8}$$

Where n_i is the number density of species i and n_{gas} is the total gas number density. As can be seen, the production of species i will depend on the rate constants and concentrations of the reactants, j and k, forming i, while the loss of i will depend on the concentration of i itself, and the species it reacts with.

For the photochemical and ionization reactions, the rate constants indicated in Eq. 3.8 are found as shown in Eqs. 3.3 and 3.4. Each reaction in the network will have a reverse reaction, and for each of these reaction pairs the most well determined reaction rate (usually for the exothermic reaction) is listed in `STAND2020`. The reverse reaction rate is then calculated based on the description by Burcat & Ruscic (2005). These calculations are described in more detail in Rimmer & Helling (2016a).

3.2.3 Required input files

In addition to the chemical network containing all of the reaction rate constants, `ARGO` requires a number of other inputs:

- Pressure-temperature profile of the planet's atmosphere
- Vertical eddy diffusion coefficient profile
- Atmospheric element abundances

- Boundary conditions for top and bottom of atmosphere
- Actinic flux from host star at the top of the atmosphere

The atmospheric layers that ARGO steps through are defined by the pressure-grid of the P-T profile, which is given as an input file to the model. Both the input P-T profiles and the eddy diffusion profiles are often obtained from GCM runs, that have modelled the radiative transfer and dynamic of the atmosphere based on the host star's irradiation. Alternatively the profiles can be estimated based on observations or measurements of Solar System objects. The P-T profile used by ARGO remains constant throughout the run, and as such there is no feedback between the chemical processes and the temperature of the atmosphere.

The atmospheric element abundances are initially assumed to be identical throughout the atmosphere, and is often set based on the composition of the host star. Based on these element abundances an initial chemical composition is set for the bottom layer of the atmosphere, often assuming chemical equilibrium. During the first global run, new chemical concentrations are calculated from the initial composition based on the reaction rates and the conditions for this specific layer. This new composition is used to calculate the chemistry of the above layers as ARGO steps up through the atmosphere.

The actinic flux is scaled to the planetary orbit based on the SED of the host star in the wavelength range 1 to 10,000 Å. As explained in Sec. 3.2.1 the direct and diffusive actinic flux is calculated for the different atmospheric layers, and based on this the photochemical reaction rate is calculated and applied when the chemical network is run.

3.3 Model inputs for radiative environments

The aim of this project is to model the atmosphere of a test planet, as it is moved around to different host stars in different galactic environments, thereby covering the range of high-energy radiation that exoplanets can be expected to encounter. As previously explained, we focus on three different sources of high-energy radiation: the XUV radiation and stellar energetic particles (SEPs) of the host star, and galactic cosmic rays (GCR) originating from outside the system.

3.3.1 Test planet

In order to isolate the effect of high-energy radiation, all models in this study are run on the same "test planet". Due to their relevance for transmission spectroscopy observations we chose a hot-Jupiter and to allow for photochemical reactions to take place in the upper atmosphere, we prioritized profiles that were extended to lower pressures. As mentioned in Sec. 3.2.3 the planet-specific inputs to the model are: pressure-temperature profiles, vertical mixing (eddy diffusion), atmospheric composition, as well as a few other parameters that can be read in Tab. 3.1.

We obtain the P-T and eddy diffusion profiles for our test planet from Helling et al. (2023), originally modeled by Baeyens et al. (2021). Baeyens et al. (2021)

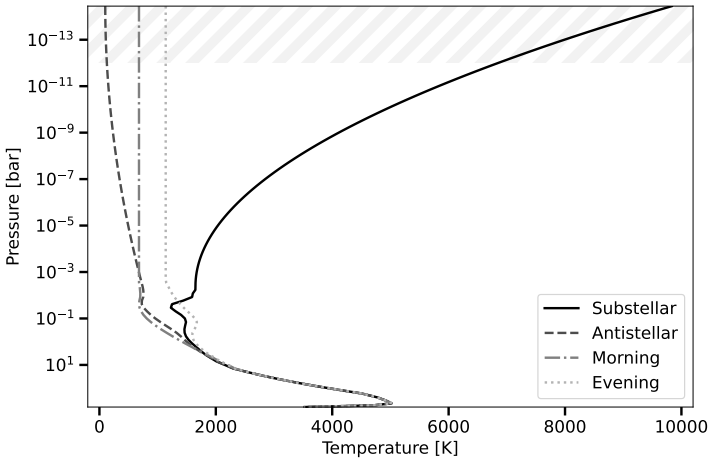

Figure 3.1: Extended pressure temperature profiles for test planet at four different coordinates. Profiles extracted from GCM model by Baeyens et al. (2021) and extended by Helling et al. (2023). Pressures lower that 10^{-12} bar are excluded due to the low collisional cross section in these regions.

Effective temperature, T_{eff}	1600K
Surface gravity, $\log_{10}(g)$	3.0 [cgs]
Semi major axis, a	0.025 AU
Period, P_{orb}	1.55 days
Host star type	G5V
Mean molecular weight, μ	2.3
Element abundances	Solar

Table 3.1: Settings for test planet used for all model runs

conducted a series of GCM simulations to create a grid of models for atmospheres with different effective temperatures and host stars. Our test planet was modelled for an effective temperature of 1600K based on a G-type host star, corresponding to a semi-major axis of $a = 0.025$ AU. Helling et al. (2023) extracted four 1D profiles (substellar point, antistellar point, morning terminator, and evening terminator) from the 3D GCM output and extended these profiles to lower pressures. The P-T profiles of the test planet at the four coordinates can be seen in Fig. 3.1. The original GCR profiles from Baeyens et al. (2021) span from 10^2 bar to 10^{-4} bar, whereas the Helling et al. (2023) profiles extend to $3.6 \cdot 10^{-15}$ bar. For the two terminators regions the extension to lower pressures was assumed to be isothermal. For the substellar and antistellar points the extension was done following the methods by García Muñoz (2007) and Yelle (2004) and the temperature for the substellar point was increased to 10,000 K, while the temperature for the antistellar point was decreased to 100 K.

Even though the extrapolation reaches $3.6 \cdot 10^{-15}$ bar, Helling et al. (2023) note that unless the gas is sufficiently ionized, the collisional cross section will most likely be too low at the upper parts of the atmosphere for the atmosphere to remain collisionally dominated. Following this reasoning, they do not consider the extrapolation beyond 10^{-12} bar, and we will implement the same cut-off in this study.

The settings shown in Tab. 3.1 and the input profiles for the test planet are kept constant throughout all model runs. This means that there is no feedback of the stellar spectrum on the P-T profiles or the effective temperature of the planet. This approach isolates the direct effect of the high-energy radiation on the chemistry from potential effects from changes in the temperature profile.

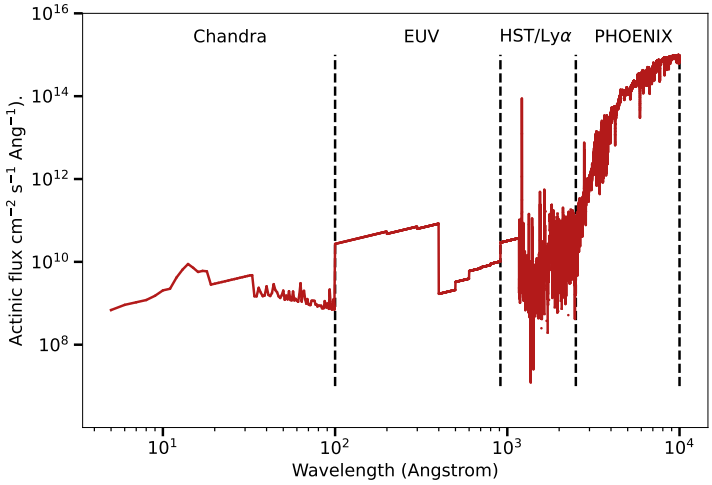

Figure 3.2: Spectral energy distribution (SED) of the M-dwarf GJ667 C obtained from the MUSCLES Treasury Survey (France et al., 2016; Youngblood et al., 2016; Loyd et al., 2016). The data for the SED are combined from different sources, as indicated by the labeled sections separated by vertical dashed lines.

3.3.2 Host stars

This study looks at planets around host stars of all seven main sequence types: M, K, G, F, A, B, and O. As mentioned in Sec. 3.2.3, the high-energy inputs from the host stars are the actinic flux in the XUV range (0 to 10,000 Å) and the SEP.

Stellar spectra

In order to get the actinic flux for the XUV radiation at the top of the atmosphere, we need to scale a SED for the host star to calculate the flux reaching the orbit of the planet.

Except for the Sun, none of our observations or models of stars cover the entire XUV wavelength range from 1 to 10,000 Å. The SEDs for most host stars are therefore combined from different observations and models. An example can be seen in Fig. 3.2 that shows the spectrum of the M-dwarf GJ667 C obtained from the MUSCLES Treasury Survey (France et al., 2016; Youngblood et al., 2016; Loyd et al., 2016). This database contains a list of M-, K- and G-star spectra for different exoplanet host stars, that have all been combined from data from different sources. As can be seen in the figure: The shorter wavelength from 0 to $\sim 10^2$ Å are obtained from the Astrophysical Plasma Emission Code (APEC) using obser-

vations from the X-ray observatories Chandra and XMM-Newton and Swift X-ray Telescope (Smith et al., 2001). The wavelength from $\sim 10^2$ to $\sim 10^3$ Å are an empirical scaling of EUV emission based on Lyα observations (Linsky et al., 2014) or Differential Emission Measure models (Duvvuri et al., 2021). The wavelength from $\sim 10^3$ to $\sim 5 \cdot 10^3$ is a reconstruction of the Lyα and UV emission based on observations from Hubble Space Telecope (Youngblood et al., 2016). For longer wavelength the spectra are synthetic and produced with the stellar atmosphere code PHOENIX (Husser et al., 2013; Allard, 2016).

Based on these SEDs, the actinic flux is calculated. The actinic flux F_λ is the total number of photons with a specific wavelength received from all directions, and it has the unit $[\mathrm{cm}^{-2}\mathrm{s}^{-1}\mathrm{\AA}^{-1}]$. It is calculated by dividing the flux of each wavelength bin by the energy of the photons in that specific bin. The final actinic flux spectrum is scaled based on the orbit of the planet to get the final XUV irradiation at the top of the atmosphere.

The scaled actinic flux spectra for the seven different host star types are shown in Fig. 3.3. Tab. 3.2 lists the SEDs the actinic flux spectra have been calculated from, in addition to which stars the SEDs are based on, and where the spectra are obtained from.

Stellar type	Spectrum based on			Reference
	T_{eff}	log(g)	Inspiration	
M	$\sim$ 3,400 K		GJ667 C (M1.5V)	MUSCLES survey *
K	5,050 K	4.0	HD189733 A (K1.5V)	Barth et al. (2021) **
G	5780 K	4.4	Sun (G2V)	Rimmer & Helling (2016a)
F	6,500 K	4.0	Procyon A (F5 IV -V)	Aguirre et al. (2023)
A	10,000 K	4.5	Sirius A, (A1)	Kurucz ***
B	16,000 K	4.0	29 Persei (B3V)	Kurucz ***
O	36,000 K	4.0	10 Lacertae (O9V)	****

Table 3.2: Information on host stars used in study including the inspiration for the stellar spectrum and the source of the data.
* France et al. (2016); Youngblood et al. (2016, 2017); Loyd et al. (2016, 2018)
** Originally from Fares et al. (2017)
*** Castelli & Kurucz (2003)
**** Hainich et al. (2019) + X-ray model provided as a courtesy of Prof. Lidia Oskinova (Potsdam University)

The SEDs for M-, K-, and F- stars are all composite spectra that have been used by previous studies, as listed in the references. The SEDs from the A- and B-stars

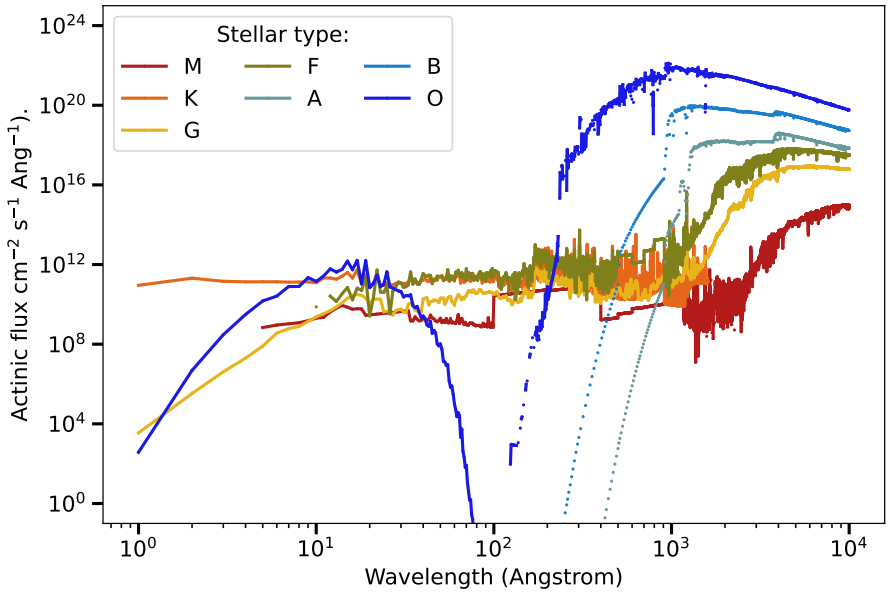

Figure 3.3: Actinic flux spectra for the different host stars host star scaled to the test planet orbit at 0.025AU. The spectra have been obtained from the following sources: M-type: MUSCLES survey. K-type: Barth et al. (2021); Fares et al. (2017). G-type Rimmer & Helling (2016a). F-type: Aguirre et al. (2023). A-type and B-type: Kurucz Castelli & Kurucz (2003). O-type: Hainich et al. (2019) for wavelength longer than 100 Ang and X-ray model provided as a courtesy of Prof. Lidia Oskinova (Potsdam University) for wavelength shorter than 100 Ang.

are therefore obtained solely from the Kurucz models for the UV and FUV range, which is reasonable since A- and B-stars are generally not X-ray sources due to their lack of surface convection zone (as reviewed by Fossati et al. (2018) and described in Sec. 1.3.1). In contrast to A- and B-star, O-stars are known to have X-ray emission due to perturbations of the hot gas in their strong stellar winds (e.g. Oskinova (2016)). The UV and FUV range of the Kurucz model is therefore not enough to cover the radiation of O-stars so a Kurucz model has been combined with an X-ray model provided as a courtesy of Prof. Lidia Oskinova (Potsdam University).

Stellar Energetic Particles

In addition to the stellar spectrum, the host star can also introduce stellar energetic particles (SEP) into the system. The effect of stellar energetic particles is implemented as an ionization rate that is added to the ionization by GCR, as

mentioned in 3.2.1 and as further described in the following section on GCR.

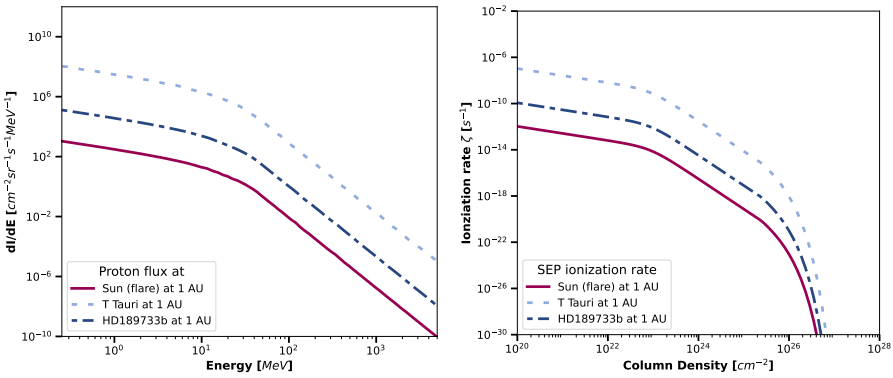

(a) **(b)**

Figure 3.4: Proton flux spectrum (a) and ionization rate (b) for the Sun (Rab et al., 2017), HD189733b (Barth et al., 2021), and a T-tauri star (Rab et al., 2017). The spectra have been calculated based on X-ray flare intensities following Herbst et al. (2019a). All spectra are scaled to 1 AU.

As explained previously in Sec. 1.3.1, SEP are released from stellar flares or coronal mass ejections and it has been found that the energetic particles and the X-ray radiation emitted during these events follow an almost linear relation (Belov et al., 2005; Hudson, 1978; Herbst et al., 2019a). The amount of SEP released can therefore be estimated based on the intensity of the X-ray flares at the same events. The correlation between the peak size distribution of the SEP (I_p) and the X-ray flare intensity (I_X) for G, K, and M stars has been described by Herbst et al. (2019a) as follows:

$$I_p(E > 10\text{MeV}) = (a \cdot I_X + (b \cdot exp(-0.001 \cdot I_X)))^{\gamma} \tag{3.9}$$

where $a = 1.22 \cdot 10^5 (\pm 7.17 \cdot 10^4)$, $b = 3.05(\pm 1.79)$ and $\gamma = 1.72(\pm 0.397)$.

These SEP proton intensities are scaled based on the orbit of the planet to get the SEP influx into the atmosphere. The ionization rates for the SEP in this study are estimated by assuming that the SEP spectrum of other stars follow the same distribution as the Sun. This is done following the procedure by first Rab et al. (2017) and later Barth et al. (2021) that estimate the SEP spectra of a T-Tauri star and the K-star HD189733b respectively by scaling the solar SEP spectrum. Rab et al. (2017) assume that the integrated proton flux of the solar event described in Eq. 3.9 also can be used to describe SEP events of other stars. They thereby scale

the spectrum of the solar event (shown in Fig. 3.4) to estimate the SEP spectrum of other stars based. Fig. 3.4a shows the SEP spectrum of the solar SEP event plotted with one of the T-tauri stars studied by Rab et al. (2017) and HD189733b studied by Barth et al. (2021).

The ionization rate can then be calculated following the approach by Rab et al. (2017) based on the total hydrogen column density ($(N_{\langle H \rangle}$):

$$\zeta_{SEP}(N_{\langle H \rangle}) = \zeta_{SEP,0}(N_{\langle H \rangle}) \times \begin{cases} 1 & \text{if } \mathrm{N}_{\langle \mathrm{H} \rangle} \leqslant \mathrm{N}_{\mathrm{E}} \\ \exp\left[-\left(\frac{\mathrm{N}_{\langle \mathrm{H} \rangle}}{\mathrm{N}_{\mathrm{E}}} - 1.0\right)\right] & \text{if } \mathrm{N}_{\langle \mathrm{H} \rangle} > \mathrm{N}_{\mathrm{E}} \end{cases} \tag{3.10}$$

where

$$\zeta_{SEP,0}(N_{\langle H \rangle}) = \left[\frac{1}{\zeta_L \left(\frac{N_{\langle H \rangle}}{10^{20}\mathrm{cm}^{-2}} \right)^a} + \frac{1}{\zeta_H \left(\frac{N_{\langle H \rangle}}{10^{20}\mathrm{cm}^{-2}} \right)^b} \right]^{-1} \left[\mathrm{s}^{-1}\right] \tag{3.11}$$

where N_E describes the column density for the exponential drop of the ionization rate, ζ_L and ζ_H account for the ionization rates at low and high column densities respectively, $a = 0.61$, and $b = -2.61$.

$$\begin{aligned} N_{\langle H \rangle} &= N_H + 2N_{H_2} \\ N_E &= 2.5 \cdot 10^{25}\mathrm{cm}^{-2} \\ \zeta_L &= 1.06 \cdot 10^{l}\mathrm{s}^{-1} \\ \zeta_H &= 8.34 \cdot 10^{h}\mathrm{s}^{-1} \end{aligned}$$

Here the exponents l and h are fitting parameters depending on the peak proton flux at the top of the atmosphere. Fig. 3.4b shows the ionization rates calculated based on the SEP intensities in Fig. 3.4a. The final SEP ionization rates are implemented together with the GCR ionization rates described in Sec. 3.2.1.

In this study we are focusing on SEP for the M-, K-, and G-type stars, since these are generally known to be magnetically active with regular flaring, and are thereby also active SEP and X-ray sources. The X-ray flare intensities and corresponding SEP spectra for K- and G-type stars are already known from Barth et al. (2021), and have been listed in Tab. 3.3.

Stellar-type	I_X at 1 AU [W m^{-2}]	Reference
M-Dwarf	$1.0 \cdot 10^{-1}$	See Tab. 3.4
K-type	$2.2 \cdot 10^{-2}$	Barth et al. (2021)
G-Type	$1.3 \cdot 10^{-4}$	Barth et al. (2021)

Table 3.3: Values for X-ray flare intensities (I_X) used to scale SEP spectrum.

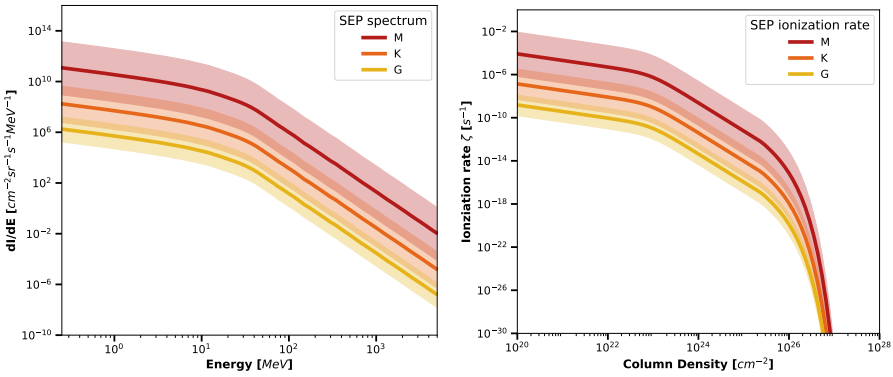

(a) **(b)**

Figure 3.5: Proton flux spectrum (a) and ionization rate (b) for an M, K, and G-type star. The spectra have been calculated based on X-ray flare intensities of the host stars (Herbst et al., 2019a) and scaled to the orbit of the test planet (0.025 AU). See X-ray flare intensities and references in Tab. 3.3.

In order to estimate the SEP of M-dwarfs we have done a literature search on X-ray flare observations on M-dwarfs and have listed a number of observed objects in Tab. 3.4. The X-ray flare intensities are here either listed directly from the publications, or have been calculated (calc) based on X-ray flare luminosities (L_X) as:

$$I_x(1AU) = \frac{L_X[erg \cdot s^{-1}] \cdot 10^{-7} \left[\frac{W}{erg \cdot s^{-1}}\right]}{4\pi(1[AU])^2} = \frac{L_X \cdot 10^{-7}}{2.8 \cdot 10^{23}}[W \cdot m^{-2}] = \frac{L_X}{2.8 \cdot 10^{30}}[W \cdot m^{-2}] \tag{3.12}$$

Based on the values in Tab. 3.4 we choose an X-ray flare intensity of 0.1 W m^{-2} as being representative for M-dwarfs. The scaled SEP spectra for the three stellar types can be seen in Fig. 3.5 together with the ionization rates that have been calculated from the spectra. These rates are used as input files for the models.

Star	Type	I_X at 1AU [W m^{-2}]	Reference
AD Leo / GJ 388	M3.5V	0.23	Segura et al. (2010)
Proxima centauri	M5.5V	6.0	Herbst et al. (2019a)
GJ876	M4V	0.1	Herbst et al. (2019a)
X128	M2V	0.39 (calc)	Hünsch et al. (2003)
X151	M0V	0.28 (calc)	Hünsch et al. (2003)
EV Lac	M4.5V	0.019 (calc)	Mitra-Kraev et al. (2004)
UV Cet	M5.5	0.0012 (calc)	Mitra-Kraev et al. (2004)
YZ CMi	M5V	0.013 (calc)	Mitra-Kraev et al. (2004)
AU Mic	M1V	0.107 (calc)	Mitra-Kraev et al. (2004)
AT Mic	M4.5V	0.103 (calc)	Mitra-Kraev et al. (2004)

Table 3.4: List of reported X-ray flares for M-dwarfs. (calc) indicates that I_X has been calculated from reported luminosities using Eq. 3.12.

3.3.3 Galactic cosmic rays

The GCR radiation implemented in this study is the ionization rate of low-energy GCR as expressed in Eq. 3.4. This ionization profile was calculated by Rimmer & Helling (2013) for a hydrogen dominated atmosphere exposed to the local interstellar spectrum (LIS) for GCR. In order to study the effect of GCR on our test planet atmosphere, we would like to vary this GCR ionization, to imitate environments that are more and less exposed to GCR.

The more accurate way to do this would be to recalculate the ionization of the atmosphere for different GCR spectra dependent on the environment of the planet. The spectrum of GCR reaching the planet's atmosphere depends both on the galactic environment around the system, the modulation of the GCR through the astrosphere, and the modulation of the GCR through the magnetic field of the planet. These recalculations were outside the scope of the project, but will be further discussed in Sec. 3.5.

To get a first approximation of different radiative environment we scale the ionization rates from Eq. 3.4 based on the expected GCR proton densities of the environment. These approximations allow us explore the effect of varying the GCR irradiation, despite not knowing the exact ionization of the atmospheres in different environments. The final ionization rates are found by multiplying the ionization calculated by Rimmer & Helling (2013) with the scale factors.

We choose seven different scale factors for the GCR: five that are based on different GCR spectra to represent specific radiative environments and two addi-

tional high GCR values to mimic more extreme cases. In this section we will first give an overview of the different environments, and then describe how the scale factors were calculated:

- **High-activity host star, low-energy environment, $\mathbf{GCR_0}$:**
  This environment imitates planets in a system completely shielded by the astrosphere of a very active host star located in a low-energy area of the galaxy. In this case we assume that there is no GCR ionization.

- **High-activity host star, LIS* environment, $\mathbf{GCR_{\mathit{low}}}$:**
  This environment imitates planets in a highly shielded system with an active host star that is located in a galactic environment similar to the solar system. In this case we estimate the GCR ionization based on the proton flux around an M-dwarf star.

- **Active host star, LIS environment, similar to Earth, $\mathbf{GCR_\oplus}$:**
  This environment imitates planets in a shielded system with a low-activity host star that is located in a galactic environment similar to the solar system. In this case we estimate the GCR ionization based on the GCR flux around Earth.

- **Medium exposure, similar to the LIS, $\mathbf{GCR_{\mathit{LIS}}}$:**
  This environment imitates planets in either an exposed system with an inactive host star in a galactic environment similar to the solar system, or a shielded system with a high-activity host star that is located in a high-energy environment. In this case we use the GCR ionization calculated for the local interstellar GCR spectrum (LIS) by Rimmer & Helling (2013).

- **Inactive host star, high-energy environment, similar to the high-energy interstellar medium, $\mathbf{GCR_{\mathit{high}}}$:**
  This environment imitates planets in an exposed system located in a high-energy environment. In this case we estimate the GCR ionization based on the GCR flux in high-energy parts of the atmosphere.

- **Very high-energy environment, $\mathbf{GCR_{50\oplus} = 50\ GCR_\oplus}$.**

- **Extremely high-energy environment, $\mathbf{GCR_{150\oplus} = 150\ GCR_\oplus}$.**

*Local Interstellar Spectrum, as described in Sec. 1.3.2

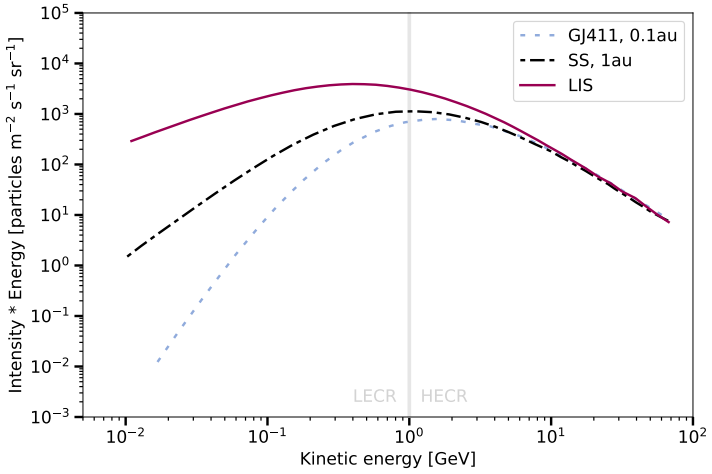

Figure 3.6: Intensity × Energy profiles for GCR radiation at the M-dwarf GJ411, the Solar System (SS), and the local interstellar spectrum (LIS). The intensity profiles have been obtained from Mesquita et al. (2021b) for GJ411 and from Jasinski et al. (2020) for the Solar System and LIS. The vertical line indicates the separation between low-energy (LECR) and high-energy (HECR) GCR.

We already know the scale factors for GCR_0 ($GCR_0 = 0$, since there is no ionization) and GCR_{LIS} ($GCR_{LIS} = 1$, since this is the original ionization profile calculated by Rimmer & Helling (2013)). $GCR_{50_\oplus}$ and $GCR_{150_\oplus}$ are both dependent on $GCR_\oplus$.

In order to estimate scale factors for the remaining environments, we look at the differences in the GCR proton fluxes between each of the environments and LIS. Figure 3.6 shows the GCR intensities for three of the environments. Since the ionization rate in a gas will not only depend on the proton flux, but also on the energy of the individual protons, the intensities have been multiplied with the energies (IE) as indicated by the y-axis. The scale factors are then found by calculating the average IE for the low energy GCR (< 1GeV) for each of the cases, and dividing them with the average IE for LIS.

The spectra shown in Fig. 3.6 for each environment have been chosen as follows:

GCR_{low} is estimated based on proton densities of GCR in an M-dwarf system. The modulation of GCR through M-dwarf systems has been simulated by multiple studies (Herbst et al., 2020; Mesquita et al., 2021a,b). Mesquita et al. (2021b) investigated the propagation of GCR through the stellar winds of five different

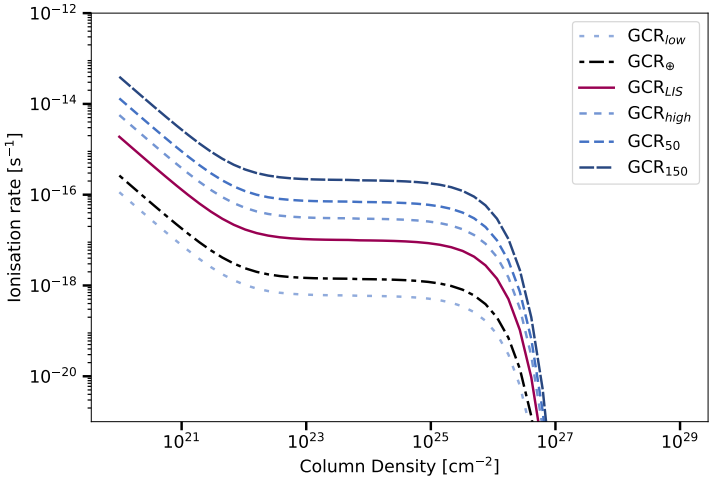

Figure 3.7: ionization rates as a function of the atmospheric column density for the different GCR environments studied in this project. The rates are estimated by scaling the LIS ionization rates (GCR$_{LIS}$, marked by full red line), as calculated by Rimmer & Helling (2013).

M-dwarfs. This was done by combining a model for 1D magnetohydrodynamic Alfvén-wave-driven stellar wind with a model for 1D GCR transport. Among the simulated systems from Mesquita et al. (2021b) we choose a representative: the M2 V star GJ 411. This star is chosen due to its size and spectral type being similar to that of GJ667C, which is the spectrum we are using for M-dwarfs in this study (see Tab. 3.2). The GCR proton density of GJ 411 is also closest to average among the five simulated systems. The GCR flux for GJ 411 at 0.1 AU is shown in Fig. 3.6.

GCR$_{\oplus}$ is estimated based on the proton densities of GCR reaching Earth through the solar system. Jasinski et al. (2020) study the propagation of GCR through the solar system, and how this if affected by changes in the heliosphere caused by differences in the surrounding interstellar medium. They estimate the GCR proton flux at 1 AU for heliospheres that have been extended to 402 AU and compressed to 26 AU, and compare these to the current solar system proton flux at 1 AU (as reported by Adriani et al. (2013)) and the LIS proton flux outside the system (as described by Bisschoff et al. (2019)). The GCR fluxess for the current solar system at 1 AU and LIS are shown in Fig. 3.6.

GCR$_{high}$ is estimated based on the proton densities of GCR in high-energy environments in the galaxy. A study by Aharonian et al. (2020) looked at the galac-

Environment	Scale factor	$\times$ $GCR_{\oplus}$
GCR_0	0	0
GCR_{low}	0.06	0.4
$GCR_{\oplus}$	0.14	1
GCR_{LIS}	1	7.3
GCR_{high}	3	22
GCR_{50}	7	50
GCR_{150}	21	150

Table 3.5: Calculated scale factors for each of the GCR environments modelled in this study. The rightmost column shows each of the scale factor in relation to the Earth.

tic distribution of GCR based on gamma ray observations from giant molecular clouds. They find that GCR further out in the galaxy (8kpc or more from the galactic center) can be described as a homogeneous "sea" with a constant proton density and spectral shape. Further into the galaxy the GCR density varies more, and they report the highest proton density ($>$ 10 GeV) to $\sim$3 times the local density. As a first approximation, we therefore choose $GCR_{high} = 3\ GCR_{LIS}$.

The scale factors for each of the cases can be seen in Tab. 3.5. The ionization rates for each environment are finally calculated by multiplying the ionization rates described by Rimmer & Helling (2013) with the scale factors, and the results are shown in Fig. 3.7.

3.3.4 Location differences

When we model tidally locked exoplanets different parts of the globe will experience widely different irradiation. The model inputs should therefore be varied accordingly.

The sub-stellar of tidally locked planets will always be facing the star. The sub-stellar point will therefore be fully irradiated by both the stellar spectrum and SEP, and both are therefore included to their full effect.

The anti-stellar point will always be facing away from the star, and neither the stellar spectrum nor SEP are included.

The terminator regions make up the boundary between the day- and night-side of the planet. They will therefore experience some irradiation, but not nearly the same amount as the sub-stellar point. How this irradiation is implemented into the model depends on the pressure range of the atmosphere being modeled. The shallow angle of incidence will cause the radiation from the host star to pass through a lot of atmospheric gas before it reaches the column of the 1D profile of

the simulated atmosphere above the terminator. This is accounted for by scaling the XUV spectrum based on the average cosine inclination angle, going from 1 at the substellar point to 0.1 at the terminator regions Moses et al. (2011).
Many models simulate a pressure range of $\sim 10^2$ bar to $\sim 10^{-5}$ bar (e.g. Baeyens et al. (2021); Barth et al. (2021); Rimmer & Rugheimer (2019); Helling (2020)). For this pressure range the upper part of the atmosphere is not included in the model, and since XUV radiation is easily scattered and absorbed by these upper parts of the atmosphere, the effect of the radiation further down is therefore negligible. The stellar spectrum might therefore be excluded for the terminator regions for many models, as we will see in Chapter 4. SEP, on the other hand, have been shown to penetrate deeper into the atmosphere (Barth et al., 2021) and should therefore be included for the terminator regions.

In this study, we scale the XUV radiation based on the incident angle for the terminator regions, but due to the approximate nature of the SEP calculations, SEP are not scaled based on the incident angle but are included at the terminators at their full effect.

3.4 Results for radiative environments and atmospheric chemistry

In this section, I describe the results of an on-going project where we model the atmosphere of a test planet, as it is moved around to different host stars in different galactic environments. We do this using the models and methods described previously in this chapter, and the end goal is a grid of models that can be compared to observations, enabling future studies to place their targets in a wider context of radiative environments.

3.4.1 Global variations in Chemistry

To get an idea of the chemistry taking place at different locations on the planet, Fig. 3.8 and 3.9 show the relative concentration of a selection of neutral and ion species on four locations along the equator: substellar and antistellar point (Fig. 3.8) and morning and evening terminators (3.9). The gas species plotted are selected to represent a broad range of chemistry, and also include some observationally interesting species, such as H_2O, CO, HCN , CH_4, NH_3, and C_2H_2 (e.g. Giacobbe et al. (2021); Barth et al. (2021)). The models for the substellar point and the two terminators were run with XUV of a G-type host star, and all four models were run without SEP and GCR irradiation. The differences in the chemistry are therefore caused by both differences in the P-T profiles and the XUV radiation. The P-T profiles have been plotted in grey on each plot and the temperatures can be read on the upper x-axis.

Comparing the substellar and antistellar points (Fig. 3.8), we notice a significant difference in the concentration profiles of both neutral molecules and ions. For the substellar point the concentrations of many neutral species decrease significantly in the upper atmosphere while for the antistellar point most neutral molecules remain stable throughout the atmospheric column. Similarly we see an increase in many ion species in the upper atmosphere for the substellar point, indicating that the neutral molecules are ionizes as illustrated for e.g. H/H^+ and Fe/Fe^+. For both locations we see that the concentration profiles of many species in the lower atmosphere are also dependent on the P-T profiles such that the concentration of species such that H, HO, O, $NH_4{}^+$, and Fe^+ are positively dependent on the temperatures, while CO_2, Fe, and H_2 are inversely dependent on the temperatures.

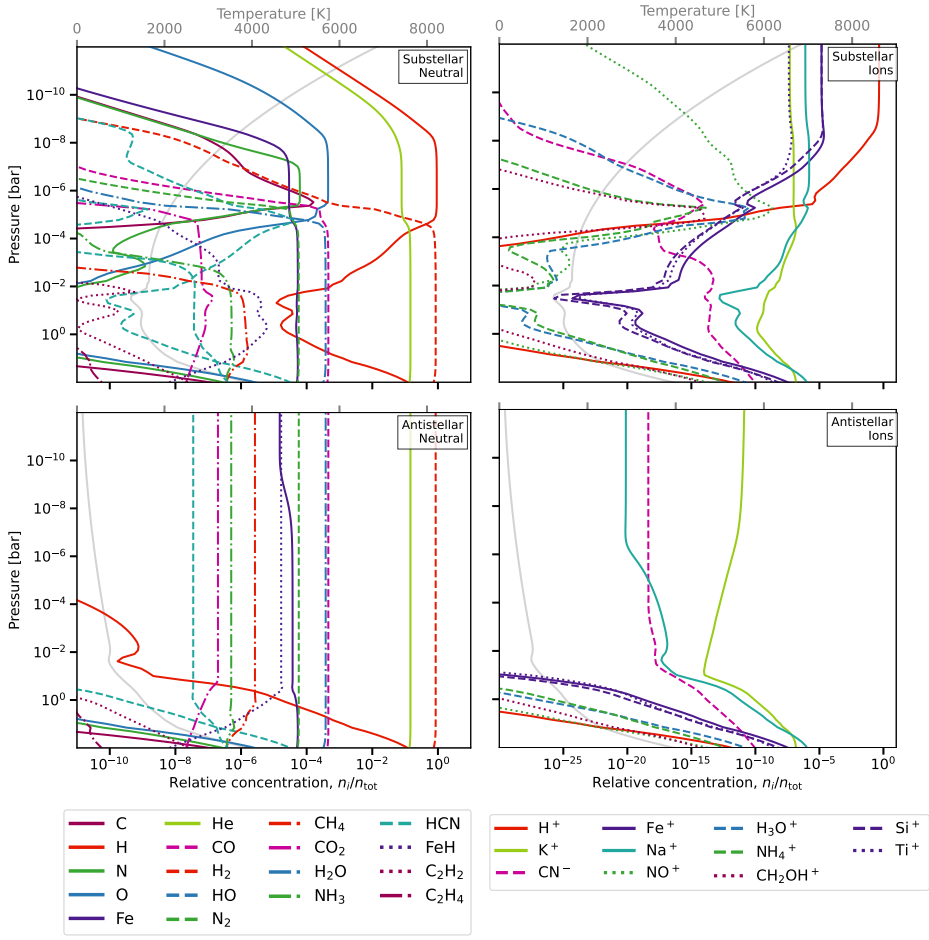

Figure 3.8: Relative concentration for a selection of gas species in the test planet atmosphere under irradiation of XUV from a G-type host star, no SEP, and GCR_0. Top: Substellar point. Bottom: Antistellar point. Left: Neutral molecules. Right: Ions. The grey line indicates the P-T profiles for each coordinate, as indicated on the upper x-axis.

Comparing the morning and evening terminators (Fig. 3.9), we notice that they follow the same trends, but that the concentrations still differ significantly. These differences are solely caused by differences in the P-T profiles, since the XUV irradiation is the same for both locations. From this it becomes apparent that the decrease in the concentrations of e.g. H, HO, and Na^+ at around 1 bar is highly dependent on the P-T profile, while the increase in the concentration of these and other species at around 10^{-2} bar depends on the external radiation rather than the temperature, since these features are visible both in the terminator regions and

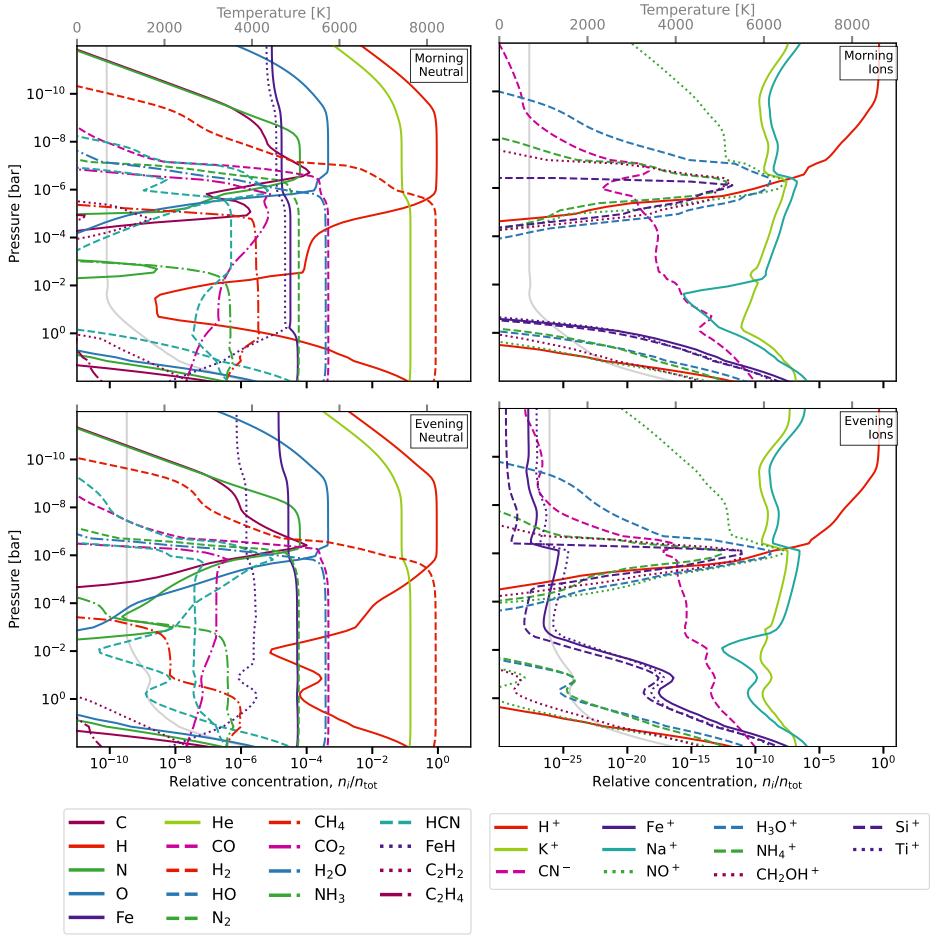

Figure 3.9: Relative concentration for a selection of gas species in the test planet atmosphere under irradiation of XUV from a G-type host star, no SEP, and GCR_0. Top: Morning terminator. Bottom: Evening terminator. Left: Neutral molecules. Right: Ions. The grey line indicates the P-T profiles for each coordinate, as indicated on the upper x-axis.

substellar point but not in the antistellar point. The fact that the terminators and substellar point shows very similar increases in concentration at 10^{-2} bar could indicate that these are caused by SEP rather than XUV, since the XUV irradiation is significantly lower for the terminators, while the SEP irradiation is the same.

Comparing the two terminator coordinates in Fig, 3.9 to the substellar point in Fig. 3.8 we notice that the decrease in the concentrations of many neutral species in the upper atmosphere is more pronounced for the substellar point and begins further down in the atmosphere (at $\sim 10^{-8}$ bar rather than $\sim 10^{-9}$ bar for the

terminators). We also notice that the metals (e.g. Fe, FeH, Fe^+, Si^+, and Ti^+), get significantly less ionized in the upper atmosphere of the terminators, as shown by higher concentrations of neutral molecules and lower concentration of ions, which shows that this ionization must be mainly caused by the XUV radiation.

3.4.2 Species of interest for different types of high-energy radiation

To study the effect of each type of high-energy radiation on the atmosphere, we would like to identify which gas species are most susceptible to high-energy radiation. We do this by first looking at some of the species that previous studies have identified as species of interest, and then by calculating which species are most affected by high-energy radiation in our study.

Species of interest from previous studies

As reviewed in Sec. 1.4, previous studies have looked at the effect of high-energy radiation, and identified a number of gas species that a sensitive to the radiation. In Fig. 3.10 we show the relative concentrations of some of these under different radiation inputs. All models are run for the substellar P-T profile, and the radiation input is varied from no radiation (black solid line), to one type of radiation (blue dotted/dashed lines), and finally all high-energy radiation (red solid line). The radiation input used in some of these models are for a G-type host star (XUV and SEP) and the GCR input is the one corresponding to the local interstellar spectrum (GCR_{LIS}).

The figure shows that the XUV model (dashed) follows the fully irradiated model (red, solid) closely for all gas species. This indicates XUV radiation is the most important type of high-energy radiation in determining the concentration of these species. The significant impact of XUV is in line with the findings of the previous studies (Linsky, 2014; Miguel & Kaltenegger, 2013; Baeyens et al., 2022; Barth et al., 2021; Scheucher et al., 2020) and emphasize the importance of photochemistry. The GCR models (dotted), on the other hand, overlap with the non-irradiated model (black, solid) for all species, indicating that GCR has no significant effect on the concentration profiles of the species. The SEP models (dot-dashed) generally follow the non-irradiated models for many of the species, but for some species (CH_4, HCN, N_2O, C_2H_2, CH_2O, and C_2H_4) the SEP models diverge, indicating that these species are affected significantly by SEP (in correspondence

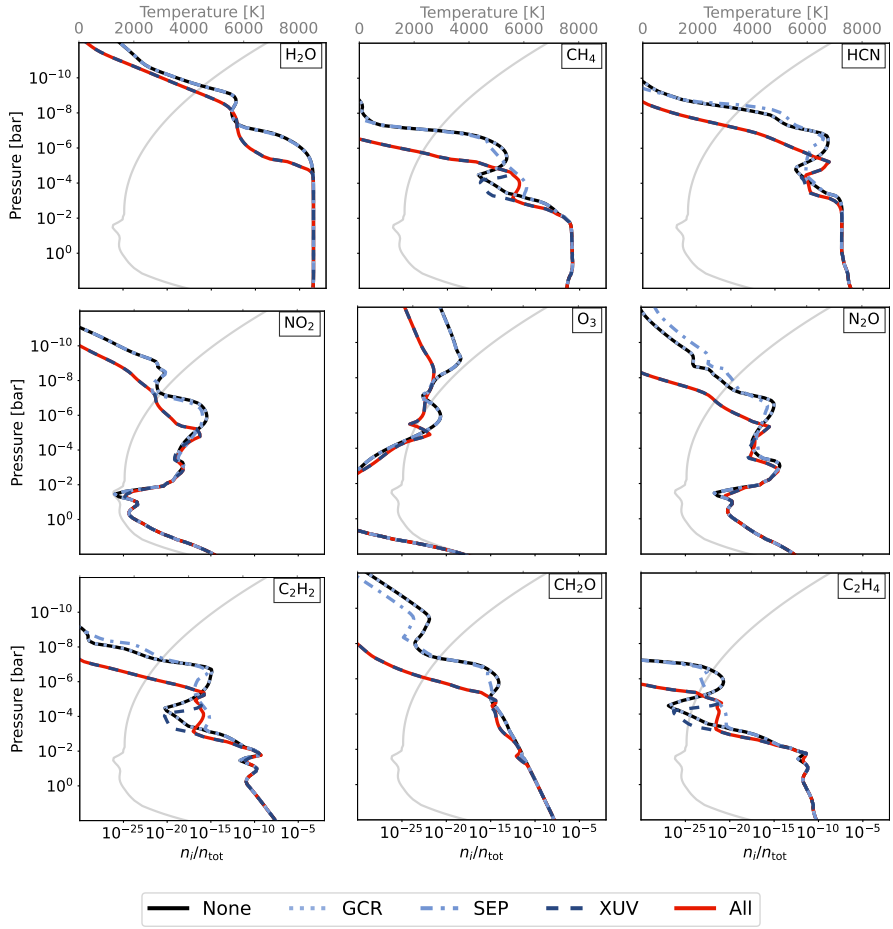

Figure 3.10: Relative concentration profiles for some of the neutral molecules that have previously been found to be affected by high-energy radiation (Miguel & Kaltenegger, 2013; Baeyens et al., 2022; Mironova et al., 2015; Herbst et al., 2023; Scheucher et al., 2020; Barth et al., 2021; Ridgway et al., 2023). The legend indicates models run with either no radiation (None), only one type of radiation: GCR_{LIS} (GCR), G-type SEP (SEP), or G-type XUV (XUV), or all three types of radiation (All). All models are run for the substellar P-T profile, as plotted in grey and indicated on the upper x-axis.

with Herbst et al. (2023); Barth et al. (2021)). In a few cases (CH_4,C_2H_2, and C_2H_4) the fully irradiated models follow the SEP models rather than XUV in the deeper part of the atmosphere (from $\sim 10^{-3}$ to $\sim 10^{-4}$ bar), indicating that SEP is the dominating type of high-energy radiation in these layers (as seen in Sec. 1.4).

Case	Maximum relative difference		Maximum total difference	
	Neutral	Ion	Neutral	Ion
SEP (M)	C_4H_6, C_4H_4, C_4H, C_4H_3, C_4H_2	CHO_2^+, $C_4H_2N^+$ $C_3H_6^+$, $C_3H_7^+$, C_3HN^+,	H, H_2, He, O, CO	H^+, He^+, C^+, O^+, N^+
SEP (K)	C_4H_{10}, C_4H_4, CH_3OCH_2, C_4H, C_4H_3	He^+, CHO_2^+, O^+, $C_4H_9^+$, N_2^+	H_2, H, He, Si, Fe	H^+, He^+, Si^+, Fe^+, Mg^+
SEP (G)	C_4H_6, C_2H_3O, CH_2CHO, C_4H, C_3H_3	C_3^+, He^+, CHO_2^+, O^+, $CH_2O_2^+$	H, H_2, He, Si, H_2O	H^+, Si^+, He^+, O^+, C^+
GCR	C_4H_6, ClS_2, CH_3OCO, Cl_2S, C_2H_5	C_3^+ He^+, CHO_2^+, $CH_2O_2^+$, O^+	H, H_2, He, H_2O, CO	H^+, He^+, C^+, N^+, O^+

Table 3.6: Potential species of interest that show the highest relative and total differences in their concentration due to irradiation by SEP or GCR. The SEP(M), SEP(K), and SEP(G) cases indicate differences calculated between two models with and without SEPs, for M-, K-, and G-type host stars respectively (GCR_0 in all cases). The GCR case indicates differences calculated between a model with GCR_0 and a model with GCR_{150}, both for G-type host stars and with no SEP.

While our models agree that XUV has a significant impact on the concentration of these species, the impact of SEP and GCR is not as compelling on these species for our test planet as for the cases presented by previous studies. In the following we therefore calculate which species might be of interest in our modelled environments.

Species that are most affected by radiation

To study the effect of each type of high-energy radiation on the atmosphere, we would like to determine which gas species are most affected by the radiation. We do this by calculating the difference in the relative concentrations $\left(\frac{n_i}{n_{tot}}\right)$ of all species between two different models with different irradiation. We calculate two differences: The total difference $\left(\left|\frac{n_i - n_j}{n_{tot}}\right|\right)$ and the relative difference $\left(\left|\frac{n_i - n_j}{n_i}\right|\right)$.

Based on the relative and total differences we select five potential species of interest for each model pair, that have the highest maximum differences across the atmospheric column. We exclude species where the relative concentration or the maximum total difference of the species are below 10^{-30}, since the concentration of these species will most likely be too low for the effect of high-energy radiation to be observed, even if the radiation affects them significantly. The species of interest are shown in Tab. 3.6-3.8, and in this section we will describe the models the species have been selected based on and what they indicate.

Star	None		M		K		G	
	Neutral	Ion	Neutral	Ion	Neutral	Ion	Neutral	Ion
M	C_3H_3N C_2H_3N HCCN NCCN C_3H_5	He^+ $C_3H_8^+$ $C_3H_9^+$ $C_4H_9^+$ $C_4H_2N^+$						
K	C_4H_6 C_4H C_4H_3 C_4H_2 C_4H_5	He^+ $C_3H_8^+$ $C_3H_9^+$ $C_4H_9^+$ $C_3H_6^+$	CH_3NO_2 CH_3NO C_4H_6 C_3H_3N S_4	C_3^+ $C_3H_9^+$ $C_3H_8^+$ $C_4H_9^+$ $C_4H_2N^+$				
G	C_4H_6 C_3H_4 C_2H_5OO C_3H_5 C_4H	He^+ $C_3H_8^+$ $C_3H_9^+$ $C_4H_9^+$ $C_3H_6^+$	C_3H_5 ClS_2 C_3H_4 HNNH C_4H_6	$C_3H_9^+$ $C_3H_8^+$ C_2^- $C_4H_9^+$ N_2^+	C_2H_4O ClS_2 C_3H_3 C_2H_4 CH_3COOH	$C_2H_4O^+$ $C_2H_4^+$ C_2^- CO^+ He^+		
F	C_3H_5 C_3H_4 C_4H HCCN CNC	He^+ C_3HN^+ CN^+ $C_2N_2^+$ $C_3N_3^+$	C_3H_5 C_3H_4 ClS_2 C_3H_3 HCCN	CN^+ C_3HN^+ $C_2N_2^+$ $C_3H_2^+$ CH^+	C_3H_4 C_3H_3 CH_2N_2 C_2H_4 ClS_2	He^+ CN^+ $C_2H_4^+$ CH^+ $C_2N_2^+$	C_3H_4 ClS_2 C_3H_3 C_2H_4 HCCN	C_3^+ He^+ CN^+ $C_2N_2^+$ C_3H^+
A	C_4H C_2 N_2O_3 HCCN C_2O	C^+ CN^+ O^+ N^+ C_3HN^+	N_2O_3 C_4H C_2 Cl_2S_2 NO_3	C^+ O^+ CN^+ N^+ H^+	ClS_2 N_2O_3 Cl_2S_2 N_2 NO_3	C^+ CN^+ O^+ N^+ CH^+	C_2 C_4H N_2O_3 He N_2	CN^+ N^+ CH^+ O^+ C^+
B	N_2O_3 Cl_2S_2 NO_3 S_2O C_2	C^+ CN^+ O^+ C_3H^+ N^+	N_2O_3 Cl_2S_2 NO_3 S_2O C_2	C^+ CN^+ N^+ O^+ CH^+	N_2O_3 NH_2O Cl_2S_2 NO_3 $C_2H_3NO_2$	C^+ CN^+ N^+ CH^+ C_2N^+	$C_2H_3NO_2$ N_2O_3 C_2N NH_2O C_2	CN^+ C^+ CH^+ N^+ C_3H^+
O	C_3H_5 C_3H_3N Cl_2S_2 HO_3 N_2O_3	He^+ C^+ C_3^+ CN^+ O^+	C_4H_6 C_3H_5 C_3H_3N Cl_2S_2 C_3H_4	He^+ C^+ CN^+ C_3^+ O^+	C_3H_3N C_3H_4 Cl_2S_2 C_3H_3 HO_3	He^+ C^+ CN^+ O^+ C_3^+	C_3H_5 C_3H_3N C_3H_3 $C_2H_5NO_2$ Cl_2S_2	He^+ C^+ CN^+ O^+ C_3^+

Table 3.7: Potential species of interest that show the highest relative differences in their concentration due to XUV radiation from different spectra. The differences are calculated between two models with different host stellar types, as indicated by the row- and column headers. The first column compares models with each of the host stars to a model with no XUV radiation. All models are with no SEP and GCR. The remaining host star combinations can be seen in Fig. 3.8

The potential species of interest for SEP and GCR irradiation are shown in Tab. 3.6. The three top rows show the potential species of interest for SEP selected based on models with M, K, and G-type host stars. In these cases the differences are calculated between models with and without the SEP irradiation for the respective host star, all with XUV spectra for the respective star, and with no GCR

Star	F		A		B	
	Neut	Ion	Neut	Ion	Neut	Ion
A	H_2N_2	NH_4^+				
	HNNH	N_2^+				
	NH_2NH	CN^+				
	HOCN	CH_4N^+				
	CH_3CN	NH_3^+				
B	$C_2H_3NO_2$	C_4H^+	$C_2H_3NO_2$	CN^+		
	ClS_2	CN^+	H_2CN	C_2^+		
	C_4H	C^+	C_4H_6	CH_4O^+		
	Cl_2S	C_2^+	C_4H	N^+		
	C_2N	$C_3H_2^+$	$C_2H_4O_2$	C_5HN^+		
O	C_3H_3	C^+	C_3H_4	C^+	NCN	$C_3H_4O^+$
	C_4H_4	CN^+	$C_2H_5NO_2$	C_3H^+	C_3H_3	$C_3H_8^+$
	$C_2H_5NO_2$	CH^+	C_4H	CN^+	HC_3N	$C_3H_9^+$
	ClS_2	C_2N^+	C_3H_3	CH^+	C_2H_4	CN^+
	H_2NNO_2	O^+	NaCl	$C_3H_5O^+$	C_2N	C_2^+

Table 3.8: Potential species of interest that show the highest relative differences in their concentration due to XUV radiation from different spectra. The differences are calculated between two models with different host stellar types, as indicated by the row- and column headers. All models are with no SEP and GCR. The remaining host star combinations can be seen in Fig. 3.7

irradiation. The fourth row shows the potential species of interest for GCR. In this case the differences are calculated between models with GCR inputs of GCR_0 and GCR_{150}, both for a G-type host star with no SEP.

As can be seen from the table, the SEP irradiation has a significant effect on the carbon chemistry. There are especially a lot of C_4H_x and C_3H_x species among both the neutral molecules and the ions with the highest maximum relative difference. There are also metals among the species with the highest maximum total difference, where both Si, Fe, Si^+, Fe^+, and Mg^+ are listed for the models with K- and G-type stars.
The GCR irradiation also affects the carbon chemistry, with a few of the most affected species being the same as for the SEPs. In addition to this some of the species with the highest relative differences are ClS_2 and Cl_2S, indicating an effect on the Cl and S chemistry.

The potential species of interest for XUV irradiation are shown in Tab. 3.7 and 3.8. The species listed here are the ones with the highest relative difference in their concentrations between models with different host stars. The host star combinations are indicated by the row- and column headers, and in all cases both neutral molecules and ions are listed.

The first column in Fig. 3.7 shows the potential species of interest calculated from the differences between models with each of the host stars and a model with no XUV radiation. This column indicates that many of the neutral species are significantly affected by multiple XUV spectra across different stellar type. This is especially organic molecules such as: C_4H_4, C_3H_5, HCCN, and C_3H_3N, which indicates that the carbon chemistry is affected by radiation over a wide wavelength range, since e.g. HCCN is listed for the A-type host that only has radiation at the longer wavelength, but even more organic molecules are listed for the low mass stars that are weaker at the longer wavelength, but also has radiation in the X-ray range. Some species such as N_2O_3, C_2, and Cl_2S_2 are only listed for the more massive stars, which could indicate that these especially are affected by the radiation at the longer wavelength. In regards to the ions, it can be seen that the high-mass stars mainly affect the concentrations of small ions, such as C^+, O^+, and N^+, whereas the low-mass stars especially affect larger more complex organic molecules which indicates that longer wavelength radiation highly affects smaller ions, while more high-energy radiation affects the complex carbon chemistry.

The rest of the columns show the species that are most affected by the differences in radiation between the different host stars. These results confirm that especially organic molecules are affected by changes in the XUV radiation, but also some N-bearing species and a few Cl_xS_x species are affected. Among the ions, we notice that a lot of smaller ions such as C^+ and CN^+ are listed for the pairings between the high- (A, B, and O) and low mass stars (M, K, G, and F), which again indicates that the characteristics of high mass stars (such as high intensities at longer wavelengths) especially affect these ions. Among low mass stars and among stars of similar sizes larger organic ions are listed as being most affected.

3.4.3 Effect of different types of radiation

To look at the effect of the different types of high energy radiation we have selected some of the most reoccurring neutral species and ions listed in Tab. 3.6, 3.7, and 3.8 and plotted them in Fig. 3.11 and Fig. 3.12. Similarly to Fig. 3.10, these figures show the relative concentration of the chosen species in atmosphere modelled with different radiation inputs. Again the different lines indicate no radiation (black solid line), one type of radiation (blue dotted/dashed lines), and all high-energy radiation (red solid line).

Looking at the neutral species in Fig. 3.11 we notice that the GCR and SEP

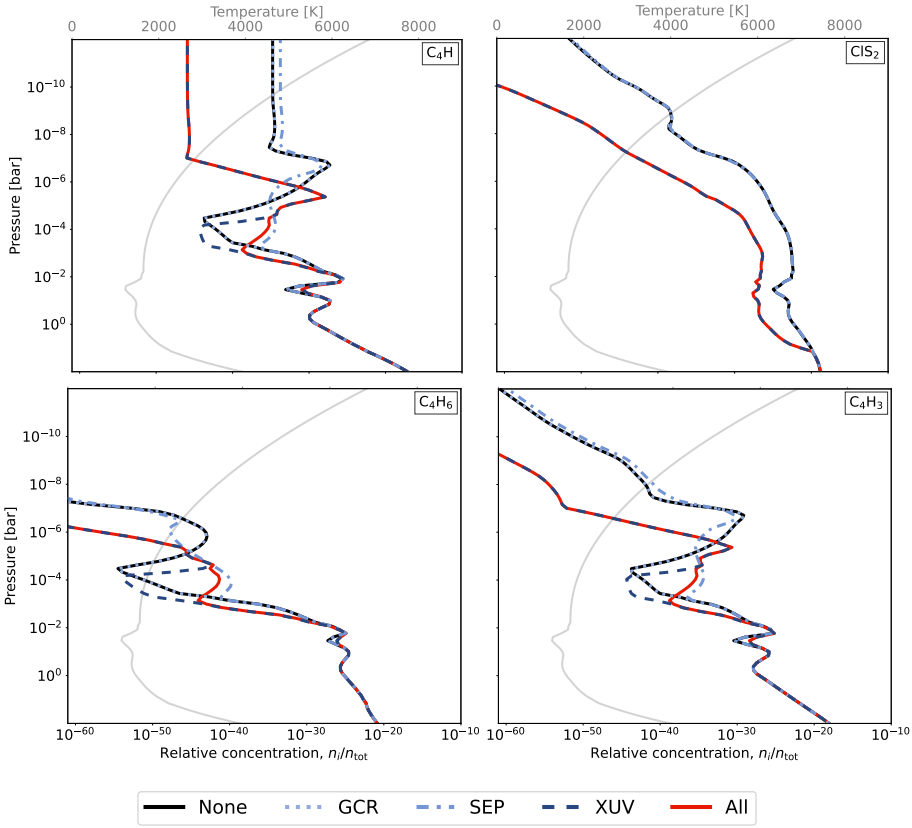

Figure 3.11: Relative concentration profiles for some of the neutral species most affected by changes in the radiation. The legend indicates models run with either no radiation (None), only one type of radiation: GCR_{LIS} (GCR), G-type SEP (SEP), or G-type XUV (XUV), or all three types of radiation (All). All models are run for the substellar P-T profile, as plotted in grey and indicated on the upper x-axis.

models (dotted and dot-dashed) are mainly following the no radiation model (solid black), while the XUV model (dashed) is following the fully radiated model (solid red). This indicates that the concentration profiles of the neutral species are primarily determined by the XUV radiation, since there is little difference between the fully irradiated model, and the model with only XUV radiation.

The exception from this is seen from the C_xH_x species in the pressure range 10^{-3} to 10^{-5} bar. In in this range the SEP model diverges significantly from the non-irradiated model, and the fully irradiated model is following the SEP. This shows us that the ionization by SEP plays a larger role in this atmospheric layer.

The GCR model follows the non-irradiated model extremely closely for the entire

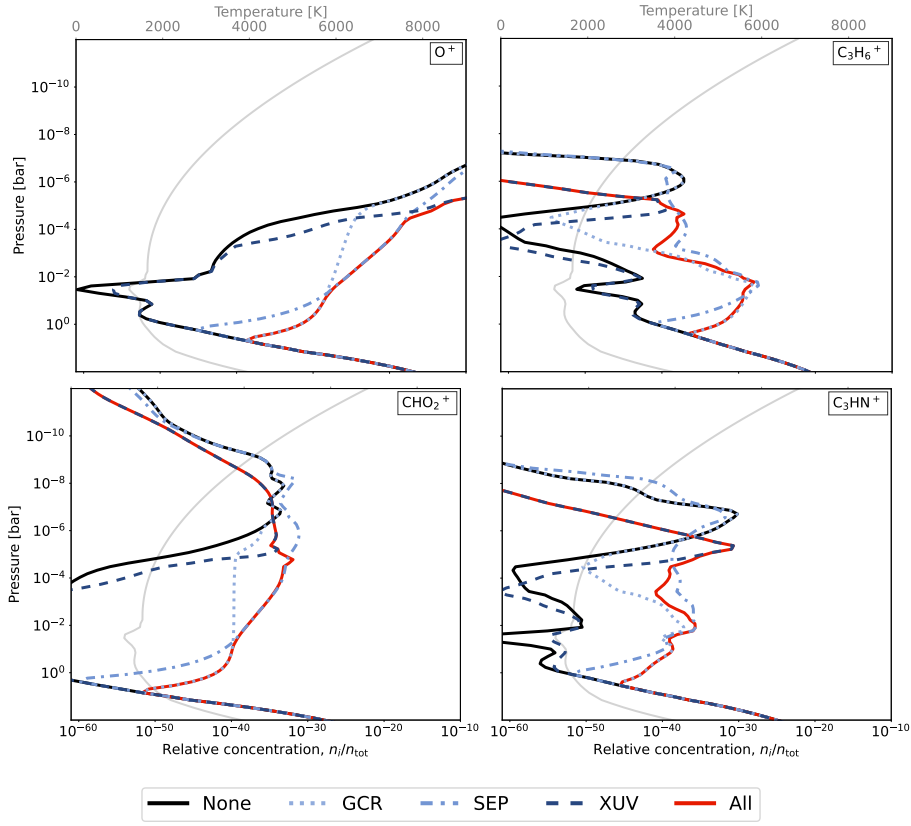

Figure 3.12: Relative concentration profiles for some of the ions that are most affected by changes in the radiation. The legend indicates models run with either no radiation (None), only one type of radiation: GCR_{LIS} (GCR), G-type SEP (SEP), or G-type XUV (XUV), or all three types of radiation (All). All models are run for the substellar P-T profile, as plotted in grey and indicated on the upper x-axis.

atmospheric column, indicating that GCR has very little effect on these neutral species, even for the species that are most effected by GCR (C_4H_6 and ClS_2) according to Tab. 3.6.

Looking at the ions in Fig. 3.12 we notice that the concentration of the ions differ significantly between the models. Here we notice that in the upper atmosphere ($p < 10^{-5}$ bar) the fully irradiated model (solid red) is still primarily determined by the XUV radiation (dashed blue), but for the lower atmosphere it is determined by the SEP and GCR input. For all four ions the fully irradiated model overlaps with the GCR model (dotted blue) for pressures of $\sim 10^{1}$ to $\sim 10^{-1}$ bar and follows the SEP model (dot-dashed blue) for pressures of $\sim 10^{-1}$ to $\sim 10^{-5}$ bar. This

indicates that SEP and GCR generally has a greater effect on the ion chemistry of the atmosphere, and that these energetic particles can be the primary factor determining the concentrations of some ions in the lower atmosphere.

3.4.4 Effect of XUV

To look at the effect of the XUV radiation of the different host stars we have plotted the concentration profiles for four of the most abundant neutral species in the atmosphere (He is excluded due to its lack of participation in the atmospheric chemistry). Fig. 3.13 shows a grid over models run for different locations on the test planet (antistellar point, morning terminator, substellar point, and evening terminator) under irradiation from different host stars. Each of the coordinates were run for their respective P-T profiles (indicated in grey) and with XUV radiation accounting for incident angles as explained in Sec. 3.3.4. Notice that since the antistellar point experiences no XUV, the first column is identical for all host stars. All models were run without SEP and GCR.

Fig. 3.13 shows that the concentration profiles for all host stars largely follow the same trends as we saw in Fig. 3.8 and Fig. 3.9, where irradiation causes a decrease in the concentrations in the upper atmosphere due to photolysis, and a dip for some species (O and H) deeper in the atmosphere due to a combination of XUV and the P-T profile. The greatest differences between the stellar types is seen in the upper atmosphere, where the more massive star (O and B) show a more extreme decrease in the concentrations due to the higher intensity of the UV radiation of these stars.

3.4.5 Effect of stellar energetic particles

To look at the effect of SEP, we have plotted the relative concentrations of the neutral species and ions that are most affected by SEP in Fig. 3.14. The figure shows the species listed with the maximum relative differences in Tab. 3.6 plotted for models with M-, K-, and G-type host stars, with and without SEP. All models are run for the substellar point with no GCR.

Fig. 3.14 shows a visible difference between the models with and without SEP for both neutral species and ions. For the neutral species (top grid), the effect of the SEP generally becomes visible at pressures below 10^{-3} bar. For the K- and G-type host stars the SEP causes an increase in the concentrations of all four

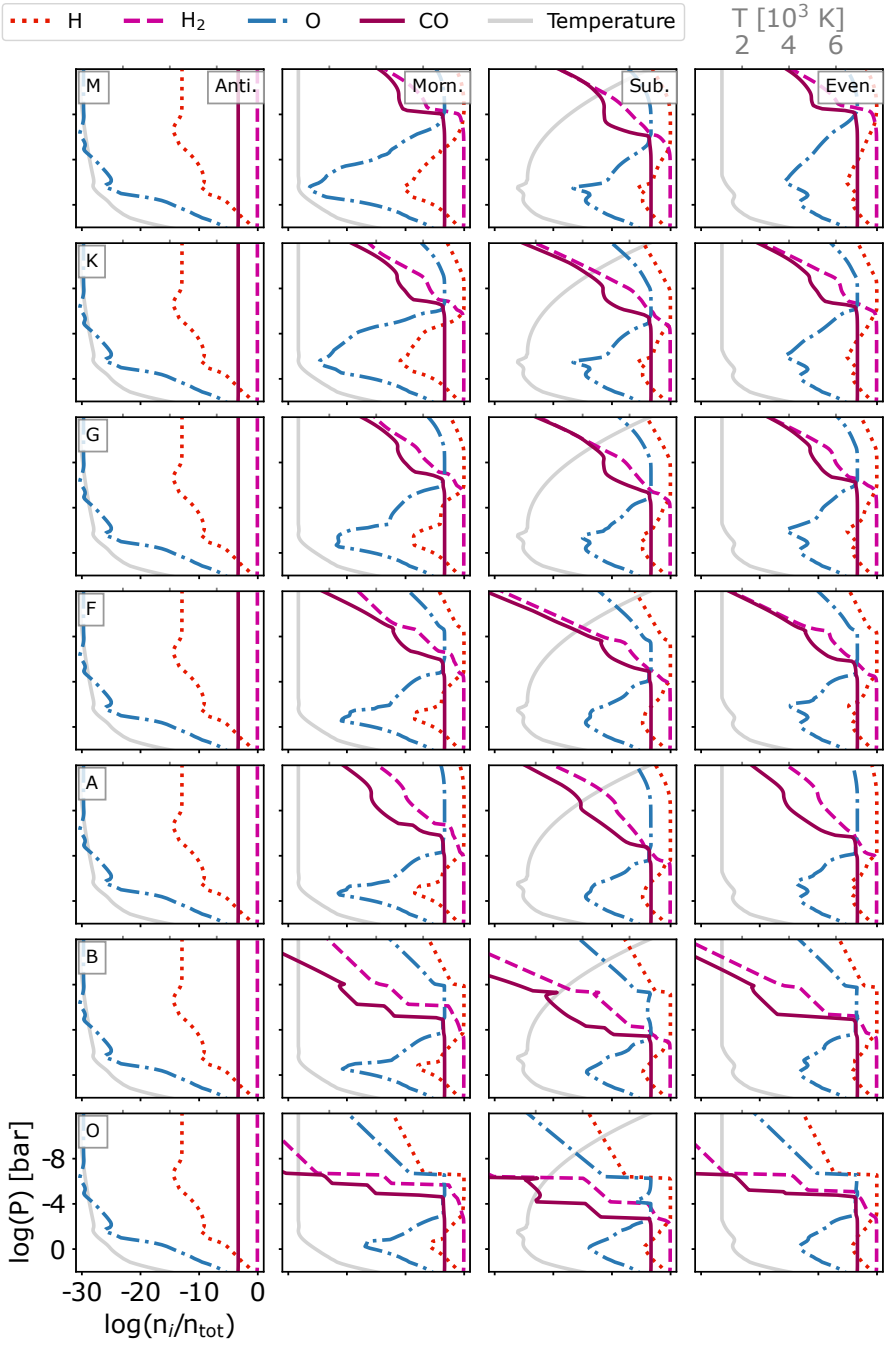

Figure 3.13: Relative concentration of some of the most abundant neutral species for different locations (columns) and host stars (rows). The axes can be read in lower left and upper right corners.

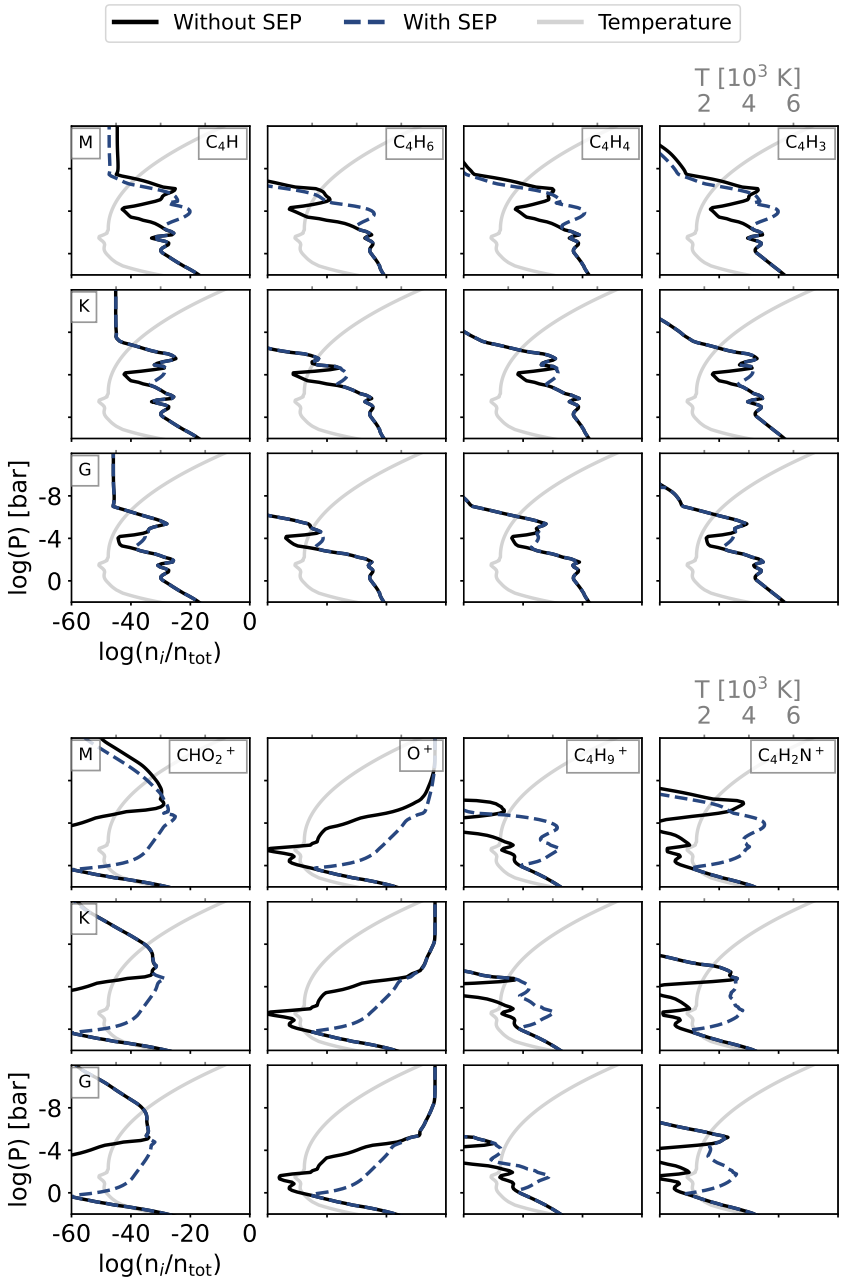

Figure 3.14: Relative concentration of the neutral gas species (top) and ions (bottom) that are most affected by SEP according to Tab. 3.6. Rows indicate stellar type of host star. The axes can be read in lower left and upper right corners.

species in the pressure range 10^{-3} to 10^{-5} bar. For the M-dwarf host star the SEP affects the concentration for the entire upper part of the atmosphere, leading to an increase in the concentration of the species from 10^{-3} to 10^{-6} bar, and a decrease in the concentration for atmospheric layers above this point.

The effect of SEP on the ions (bottom grid) is similar to the effect on the neutral species. We see an increase in the concentration of ions in the lower atmosphere (10^{0} to 10^{-4} bar) for all stellar types, and a decrease in the concentration of ions in the upper atmosphere for the M-dwarf stars.

The differences between the effect of the K- and G-type SEP and the M-dwarf SEP indicates that the effect of the SEP scales significantly with the influx of SEP from the host star, and thereby also the activity of the star.

3.4.6 Effect of galactic cosmic rays

To look at the effect of GCR we have plotted the relative concentrations of the neutral species and ions that are most affected by GCR in Fig. 3.15. The figure shows the species listed with the maximum relative differences in Tab. 3.6 plotted for seven different models covering all the GCR inputs described in Sec. 3.3.3. All models are run for the substellar point with a G-type XUV spectrum and no SEP.

Among the neutral species (Fig. 3.15, top) only one of the species (C_2H_5) show a visible difference in the concentrations for different GCR inputs, and the difference only occurs at the top of the atmosphere at relative concentrations below 10^{-50}. This is in accordance with what we saw in Fig. 3.11, that GCR has very little effect on the concentrations of the neutral species.

Among the ions (Fig. 3.15, bottom) the differences are more pronounced. Comparing the model with no GCR input (GCR_0, solid lines) with the models with GCR inputs (GCR_{low} to GCR_{150}, dotted/dashed) we notice that there is a significant difference between the non-irradiated model and the irradiated models, while the differences among the irradiated models are smaller.

The general effect of the GCR is an increase in the concentrations of the ions in the pressure range $\sim 10^{1}$ to $\sim 10^{-5}$ bar in accordance with the ionizing effect seen in Fig. 3.12. From the Fig. 3.15 (top) we notice that also the concentrations of the neutral species, C_2H_5 is increased as a result of the GCR radiation, indicating that this species is a bi-product of ionization.

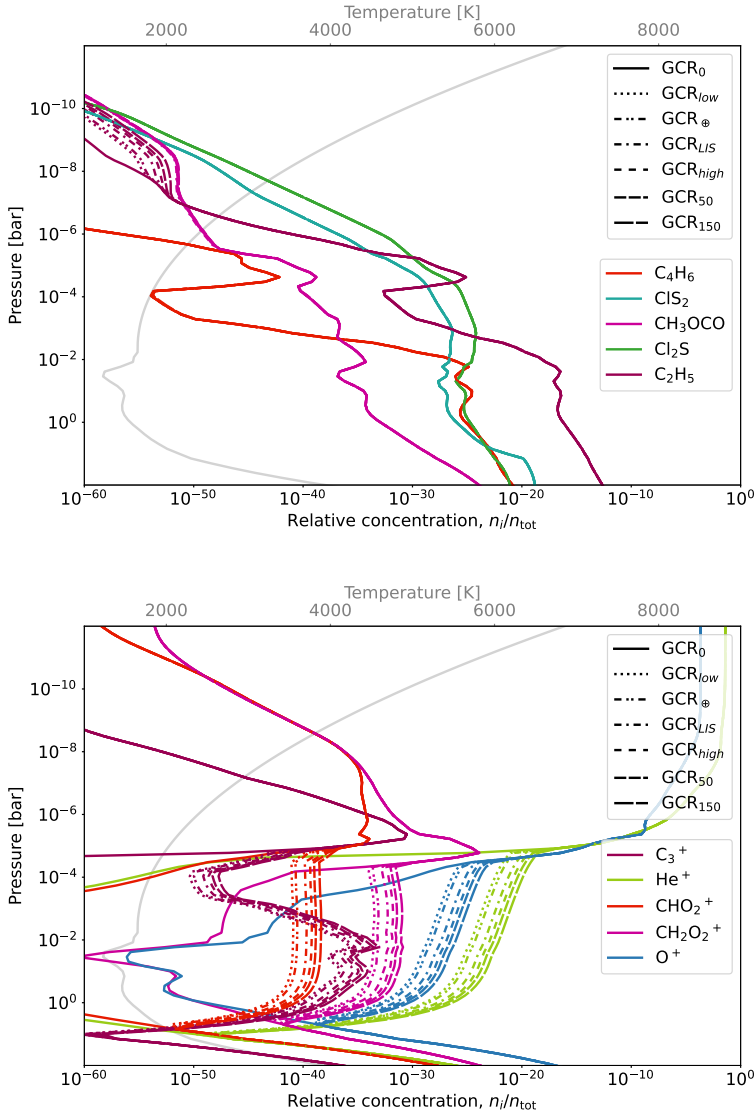

Figure 3.15: Relative concentration of the neutral gas species (top) and ions (bottom) that are most affected by GCR according to Tab. 3.6. Colours indicate species and line styles indicate GCR irradiation.

Since the differences among the different irradiated models (GCR$_{low}$ to GCR$_{150}$, dotted/dashed) are smaller in the following we will move forward with only four models that cover the entire range: GCR$_0$, GCR$_\oplus$, GCR$_{LIS}$, and GCR$_{150}$.

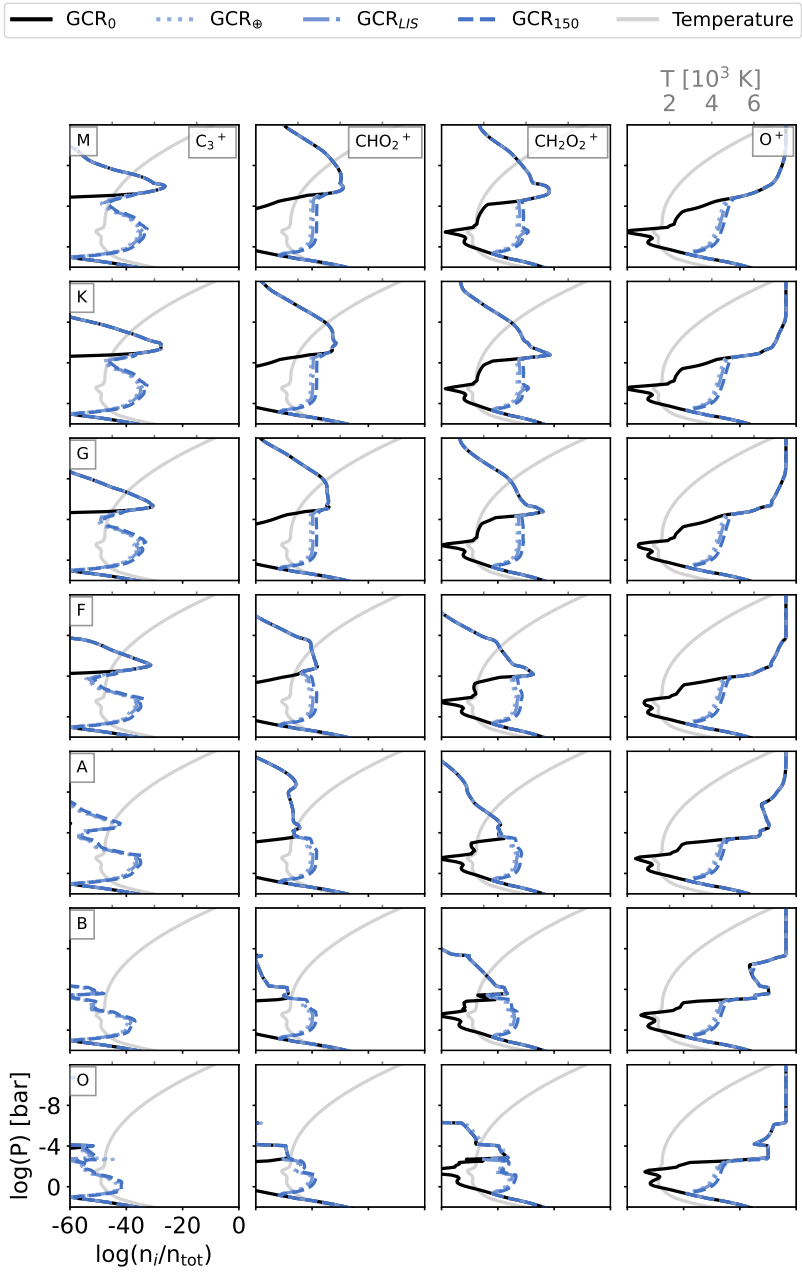

Figure 3.16: Relative concentration of the ions that are most affected by GCR according to Tab. 3.6. Rows indicate stellar type of host star. The axes can be read in lower left and upper right corners.

Figure 3.16 shows a grid of models for different host stars and GCR inputs. The plots show the concentrations of four of the ions that most affected by GCR (He^+ has been excluded it generally does not participate in the chemical reactions of the atmosphere). Comparing the models for the different host stars we notice that GCR causes an increase in concentration of ions in the lower atmosphere for all stellar types, and that these GCR-caused features remain similar even when the rest of the profile (determined by XUV) changes.

The fact that the concentration profiles remain so similar for the entire range of GCR (from $GCR_{low} = 0.4\ GCR_{\oplus}$ to $GCR_{150} = 150\ GCR_{\oplus}$) could indicate that the effect of GCR remains largely the same, regardless of the intensity of GCR in the environment.

3.4.7 Global run 10 vs global run 20

In this study, the models are run for 10 global runs, meaning following the parcel of gas up and down through the atmosphere 10 times (as explained in Sec. 3.2.1). This choice was made based on Rimmer & Helling (2016a) stating that depending on the input parameters `ARGO` will usually reach convergence within 5 to 12 global runs.

To test the validity of this choice we have selected some of the more extreme input cases and run them for 20 global runs, to look at the difference. Fig. 3.17 compares models run 10 and 20 global runs for four cases: 1) No radiation. 2) An M-dwarf case with XUV and SEP suitable for M-dwarfs and no GCR (GCR_0). 3) A G-type star case with XUV and SEP suitable for G-type stars and medium GCR (GCR_{LIS}). 4) An O-type star case with XUV for a O-type star and high irradiation by GCR (GCR_{150}). These cases cover the full range of XUV (from none, to M-dwarfs, to O-type), SEPs (from none to M-dwarf), and GCR (from none to GCR_{150}), as well as the standard case we have used throughout for a G-type host star.

Comparing the solid colored lines (indicating the 10 global run models) with their corresponding dashed black lines (indicating the 20 global run models), we see that in most cases they are completely overlapping. This indicates that there is very little difference in the chemistry between the 10th and the 20th global runs, and that the models are almost completely static in-between. The greatest difference is seen for the O-type case. By calculating the maximum and relative differences between the concentrations (as done in Sec. 3.4.2), we find that the

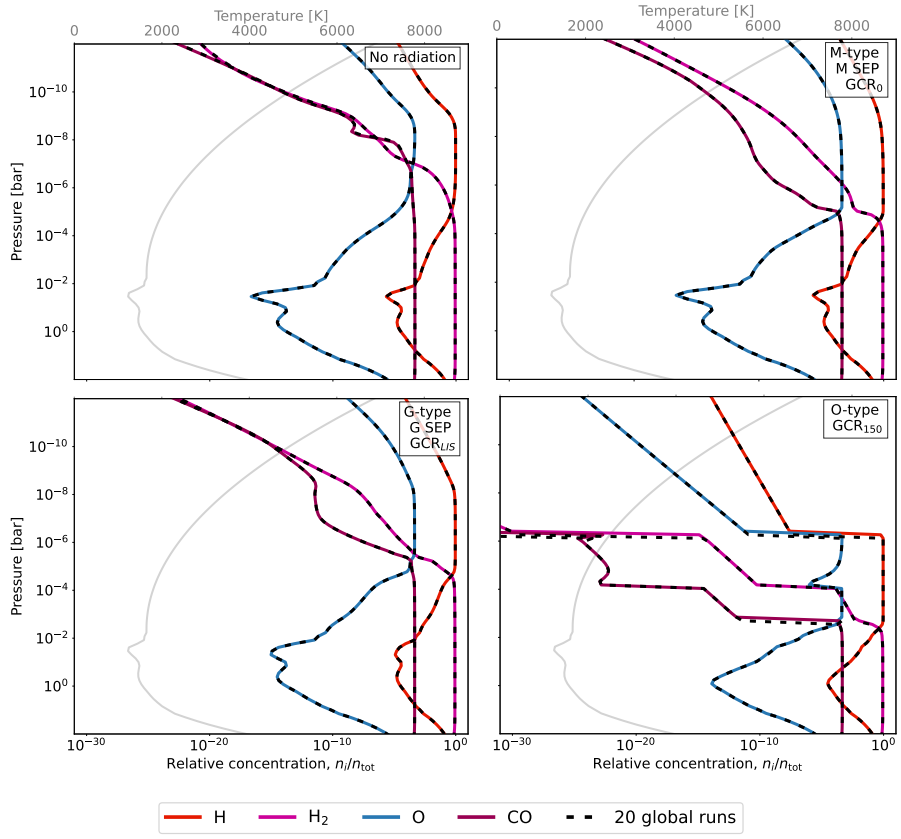

Figure 3.17: Relative concentration profiles for some of the most abundant neutral species run for different radiation cases (indicated by labels). Each setting is run for 10 and 20 global runs, indicated by solid colored lines and overlapping dashed lines respectively. All models have been run for the substellar P-T profile.

highest maximum difference is seen for H, that has a maximum difference of $5.9 \cdot 10^{-1}$. Looking more closely at the profiles, it is how ever seen that this difference is a numerical feature caused by a single shift in the data points along the pressure axis of otherwise identical profiles, and that the medium difference even in this radiation case is 0. Due to the insignificant differences between the models run for 10 and 20 global runs we conclude that 10 global runs are sufficient for this study.

3.5 Discussion

The discovery of exoplanets has revealed that planetary environments can differ significantly from our Solar System, particularly in terms of high-energy radiation. High-energy radiation is known to impact the Earth's atmosphere through photochemical reactions and ionization of the upper atmosphere (see review in Mironova et al. (2015)). Similar effects are expected on exoplanets, where models predict that high-energy radiation can significantly change the chemical composition (e.g. Baeyens et al. (2022); Barth et al. (2021)), cause atmosphere loss (Johnstone, 2016), promote cloud formation (e.g. Svensmark et al. (2013)), and change the overall habitability of the planets (e.g. Ridgway et al. (2023); Engelbrecht et al. (2024)). With missions such as JWST and CHEOPS, and soon potentially ELT, PLATO, and Ariel, we are starting to get detailed exoplanet atmosphere observations. In order to analyse and interpret these observations, we need to understand the processes taking place in the atmospheres, and here high-energy processes such as photochemistry have already proven to be a challenge (as shown by Rustamkulov et al. (2023); Alderson et al. (2023); Tsai et al. (2023), reviewed in Sec. 1.4).

In this study, we have aimed to explore the effects of high-energy radiation on the chemistry of exoplanet atmospheres. This study has focused on two primary sources of high-energy radiation: 1) the host star, through XUV radiation and stellar energetic particles (SEPs), and 2) the galactic environment, through galactic cosmic rays (GCRs).

We estimate the effect of GCR on our test planet by scaling the modelled GCR ionization described by Rimmer & Helling (2013) based on the proton density of the environment. The ionization rates modelled by Rimmer & Helling (2013) assume a H dominated atmosphere irradiated by the GCR spectrum outside the Solar System (LIS: The Local interstellar spectrum). Scaling a known ionization profile is a first approximation to explore the effect of GCR. However, the actual influx of GCR into a system, and the resulting ionization rate in an environment is non-trivial, and should not be expected to scale directly with proton density. A more accurate approach to calculate the ionizing effect of GCR would therefore be to directly model first the GCR propagation through the astrosphere of the specific host stars (similarly to, e.g. Rodgers-Lee et al. (2023); Mesquita et al. (2021a); Svensmark (2006), see more references in Sec. 1.3), second the propagation of GCR through the magnetosphere of the planet (similarly to e.g. Grießmeier et al.

(2015, 2005)), and thirdly the energy-dependent propagation and ionization of the individual GCR particles entering into the atmosphere (similarly to, e.g. Rimmer & Helling (2013)). In all three cases the behaviour of the GCR will be strongly dependent on the energy of the GCR, with lower energy GCR particles being more strongly affected by the modulation through both the astrosphere and the planetary magnetosphere (e.g. Patrignani et al. (2016); Grießmeier et al. (2015)), and the ionization of the atmosphere also being energy dependent (Mironova et al. (2015)). It is therefore not only important to understand the behaviour of the GCR particles inside the system, but also the energy distribution of the particles entering the system. As mentioned in Sec. 1.3, the GCR distribution seems to be forming a homogeneous "sea" at galactic distances of > 8 kpc, with a potential increase in the GCR density closer to the galactic center, either due to a global change of the sea or due to an increased number of GCR accelerators (Aharonian et al., 2020; Peron et al., 2021). The exact GCR distribution is, however, uncertain and the potential changes in the GCR energy distribution are not yet understood.

In this study, we seek to understand the overall effect of GCR on the atmosphere in comparison with SEP and XUV radiation. As such, the exact propagation and ionization profiles of the individual systems and environments are less important. In addition to this, the GCR influx into the atmosphere can vary significantly over time due to e.g. changes in the stellar activity, and as shown by Herbst et al. (2020), this can cause uncertainties in the GCR intensities of several orders of magnitude. We therefore believe that our GCR estimate is a valid approach for an investigation of the effect on the GCR parameter space. However, if we wish to truly understand the radiative environments in the specific systems and their effect on the atmosphere, it would be beneficial to expand this study with more detailed models of the GCR ionization.

A potential advancement for understanding the radiative environments of exoplanets could come with the mission Athena+ (Nandra et al., 2013; noa, 2024). Athena+ (Advanced Telescope for High ENergy Astrophysics) is a space-based X-ray observatory set to be launched in the 2030s, that aims to explore the hot and energetic universe. One of the goals of Athena+ is to observe the X-ray radiation of exoplanet systems, which will allow a more in-depth study of host star activity and some of the effects of stellar energetic particles and stellar wind on close-in exoplanet atmospheres (Branduardi-Raymont et al., 2013). Athena+ is also set to observe GCR (Meidinger, 2018), and through their observations of the high-energy areas of the galaxy this could give us new insight into the formation and

distribution of GCR in the galaxy.

In this study, we have scaled the energetic particles for galactic environment and stellar activity of the host star, but we have not taken the planet's magnetic field into account which has been found by Grießmeier et al. (2015) to be able to change the influx of GCR by three orders of magnitude. Since a potential magnetic field would function to shield the atmosphere from energetic particles, the actual influx of SEP and GCR into the atmosphere could therefore be expected to lie in-between the irradiated and non-irradiated models presented in this study.

3.6 Summary

In this study, we have explored the question of how the high-energy radiative environment affects the complex chemistry of exoplanet atmospheres.

Using the 1D photo-chemistry and diffusion code `ARGO` in conjunction with the chemical kinetic network `STAND2020`, we modeled the disequilibrium chemistry of a hot-Jupiter in a series of simulated radiative environments. The radiative inputs for these environments were varied as follows:
XUV radiation: Composite spectra, obtained from the literature for seven main sequence host stars: M-, K-, G-, F-, A-, B-, and O-type stars.
Stellar energetic particles (SEP): SEP proton flux spectra for M-, K-, and G-type stars obtained by scaling the solar SEP spectrum based on observed X-ray flare luminosities.
Galactic cosmic rays (GCR): Seven GCR environments are estimated based on GCR proton densities in the ISM and GCR propagation through astrospheres as described in the literature.

We will here summarise our main findings:

- XUV radiation is the most important type of high-energy radiation for determining the concentration of most atmospheric species.
- The neutral species that are most affected by SEPs are hydrocarbons. For some species such as CH_4, C_2H_2, C_2H_4, and C_4H, as well as many ions, SEP is the most important type of high-energy radiation in the deeper atmosphere, from 10^{-3} to 10^{-5} bar.
- SEP radiation leads to an increase in the concentration of many C_4H_x species in the lower atmosphere $\left(< 10^{-6}\right)$ for M-, K-, and G-type stars. For M-type

stars there is a decrease in the concentration of the same species in the upper atmosphere.

- GCR has little effect on the neutral species, but has a significant effect on the concentrations of many ions. For some species such as O^+, ${C_3H_6}^+$, ${CHO_2}^+$, and C_3HN^+, GCR is the most important type of high-energy radiation in the lower atmosphere, from 10^1 to 10^{-1} bar.
- Comparing the non-irradiated model to the models irradiated with GCR we see a significant difference in the concentration of the species that are most affected by GCR. The variation between the different GCR-irradiated models is, however, very small, despite the GCR ionization changing by a factor of > 350.

The study presented in this chapter is still ongoing and the results are not yet published. The next step in the project will be to identify molecules that can act as observable tracer for the different types of high-energy radiation. We will test the observabilities of these tracer molecules by producing synthetic transmission spectra of the test planet, and see if the change in concentration caused by the high-energy radiation leads to a feature that is observable within the accuracy of JWST. We will present more on this approach in Chapter 4. When we have found observable tracer molecules they can be used as a reference when analysing and interpreting atmosphere observations.

4

Cloud formation on warm Saturn around M-dwarf star

- A case study of HATS-6b

In this chapter, I present the work done for the submitted publication Kiefer et al. (submitted 2024), titled "*Under the magnifying glass: A combined 3D model applied to cloudy warm Saturn-type exoplanets around M-dwarfs*". This work combines several state-of-the-art models to assess whether cloud formation can be added to General Circulation Models (GCMs) in a post-processed manner, producing results that are credible within the accuracy limits of JWST observations. The study focuses on HATS-6b, a warm Saturn orbiting an M-dwarf star.

The contributions to the work were as follows:

- Sven Kiefer (first author) designed and ran the integration between the GCM

and the cloud model outputs, modeled the synthetic spectra, and was primarily responsible for project planning, writing, and data analysis.

- I (second author) modeled the disequilibrium chemistry of the atmosphere, wrote most sections concerning the disequilibrium chemistry, and participated in project planning, data analysis, and paper revisions.
- Dominic Samra and David Lewis ran the microphysical cloud formation models, wrote the sections on this topic, participated in data analysis, and contributed to paper revisions.
- Aaron Schneider ran the cloudless GCMs and participated in project planning.
- Flavia Amadio ran the initial equilibrium chemistry model and participated in project planning.
- Helena Lecoq-Molinos participated in project planning, assisted with data analysis, and contributed to paper revisions.
- Ludmila Carone, Leen Decin, Uffe Jørgensen, and Christiane Helling supervised the project, contributed to the writing, and performed revisions on the paper.

This chapter is adapted from the publication with a focus on the sections authored by me. All sections related to disequilibrium chemistry are included in a form close to their original version, while I have rewritten and summarized the introduction, discussion, and conclusion, as well as methods and results contributed by other co-authors.

4.1 Introduction

Warm Saturns are a class of Saturn-sized gas giants that are promising observation targets due to their size, close proximity to their host star, and slightly lower equilibrium temperatures (500 - 1200 K) than hot Jupiters. When observing the atmospheres of warm Saturns, Hubble Space Telescope found muted or absent spectral feature, which could suggest either an extensive cloud coverage or a cloud-free atmosphere with a high metallicity composition (Komacek et al., 2020; Carone et al., 2021; Wong et al., 2022). The James Webb Space Telescope (JWST) is expected to provide clearer insights into these atmospheres.

Warm Saturns have previously been observed around K-, G-, and F-type stars (Buchhave et al., 2018), with a few detections around M-dwarfs (Cañas et al., 2022; Lin et al., 2023; Hartman et al., 2015). Warm Saturns around M-dwarf stars are especially interesting targets due to the favorable stellar-to-planetary radius ratio caused by the significant size of the planet compared to the small host star. Atmosphere observations of warm Saturns around M-dwarf stars have previously been difficult, since M-dwarfs are faint at the wavelengths that have been covered by telescopes like HST, and instead peak at longer wavelength. However, this makes them ideal targets for infrared transmission spectroscopy with JWST, where they provide an opportunity to study the cloud formation and chemistry of gas giant planets around a different host stellar types. Initial studies with General Circulation Models (GCMs) suggest that warm Saturns have more uniform temperatures compared to hot Jupiters, with efficient heat circulation along the equator (Christie et al., 2022; Helling et al., 2023; Kataria et al., 2016; Komacek & Showman, 2016). This likely leads to global, mixed composition cloud coverage (Christie et al., 2022; Helling et al., 2023), which impacts atmospheric temperature by scattering incoming radiation from the star, while also creating a greenhouse effect by absorbing and re-emitting thermal radiation from the planet itself (Rowe et al., 2008). Understanding these processes requires 3D modeling of cloud properties and their distribution, as demonstrated previously for hot Jupiters and rocky exoplanets (Lines et al., 2018a; Powell et al., 2019; Parmentier et al., 2021; Lee et al., 2023; Yang et al., 2014; Turbet et al., 2021).

Accurate characterization of cloud properties, gas-phase chemistry, and wind flow in exoplanet atmospheres requires complex cloud models. These models range from simplified cloud descriptions assuming phase equilibrium (Demory et al., 2013; Webber et al., 2015; Crossfield, 2015; Kempton et al., 2017; Roman & Rauscher, 2017; Roman et al., 2021) to fully self-consistent micro-physical theories (Woitke & Helling, 2003; Helling & Woitke, 2006; Helling & Fomins, 2013; Powell et al., 2018; Woitke et al., 2020; Gao et al., 2020). While 1D models are useful for modelling radiative transfer and microphysical cloud formation (Helling et al., 2008a; Witte et al., 2011; Juncher et al., 2017; Gao et al., 2020), they cannot capture the complex atmospheric processes like equatorial wind jets, day-night cold traps, and patchy clouds (e.g. Showman & Guillot, 2002; Parmentier et al., 2013; Pelletier et al., 2023; Perez-Becker & Showman, 2013; Komacek et al., 2017; Helling et al., 2019a; Line & Parmentier, 2016; Tan & Showman, 2021).

To study cloud formation globally we need to combine a 3D GCM with a de-

tailed cloud formation model, which is very computationally intensive if the models are coupled directly (Lee et al., 2016, 2017; Lines et al., 2018a,b). To lower the computational cost we can use a hierarchical approach where the output of GCMs can be used to post-process cloud structures (Helling et al., 2016; Kataria et al., 2016; Parmentier et al., 2016; Helling et al., 2019b, 2021; Robbins-Blanch et al., 2022; Savel et al., 2022; Helling et al., 2023). While this allows for a full modelling of both the global climate and the detailed cloud formation, there is no feedback between the two models so it does not include the interactions between clouds and climate.

HATS-6b was discovered by the HATSouth survey in 2015 and has well-constrained planetary and stellar parameters, as listed in Tab. 4.1. HATS-6b is an interesting case for multiple reasons.

- Warm Saturns around M-dwarfs challenge or theories of planet formation where models predict that gas giants mainly form around massive host stars, since these have more material in their protoplanetary disk (e.g. Pascucci et al., 2016).
- Due to the relative sizes of the planet and star, HATS-6b has one of the deepest transit depths known with $(R_P/R_\star)^2 = 0.0323 \pm 0.0003$ around 600 nm.
- M-dwarfs have a higher magnetic activity than solar-type stars (Mignon et al., 2023), which causes a higher emission of stellar energetic particles (SEPs, e.g. Fraschetti et al., 2019; Rodgers-Lee et al., 2023). HATS-6b therefore presents and opportunity to study the effect of SEP on an observable gas giant.
- The host star, HATS-6, has a J band magnitude of 12.05, making HATS-6b very well suitable for atmospheric characterisation in the infrared. HATS-6b is therefore among eight warm Saturns, that have been selected as targets for two general observer programs for the James Webb Space Telescope (JWST) Cycle 2 (GO 3171 and 3731).

This study has two aims. Firstly, we aim to explore the atmospheric, microphysical cloud and gas-phase structure of the warm Saturn HATS-6b orbiting an M-dwarf. For this, we use a combined model in the form of step-wise iterations between a detailed cloud formation description and `expeRT/MITgcm`, a 3D GCM

Equilibrium temperature, T_{eq}	700 K
Mass, M_P	0.319 ± 0.070 M_J
Radius, R_P	0.998 ± 0.019 R_J
Surface gravity, $\log_{10}(g)$	2.9 [cgs]
Semi major axis, a	0.036 AU
Period, P_{orb}	3.32 days (Tidally locked)
Mean molecular weight, μ	2.35
Element abundances	Solar, scaled to [Fe/H] $= 0.2 \pm 0.09$
Host star type	M1V
Stellar effective temperature, $T_{eff,*}$	3724 K
Stellar mass, M_*	0.57 $M_\odot$
Stellar radius, R_*	0.57 $R_\odot$

Table 4.1: Planetary (top) and stellar (bottom) parameters, and settings for test planet used for all model runs

with full radiative transfer and deep atmosphere extension. Secondly, we aim to demonstrate how the combined modelling approach can help to support the interpretation of the data from space missions (e.g. JWST) for warm Saturn type planets. The step-wise iterative approach between the GCM and cloud structure is described in Sect. 4.2.1. The evaluation of the combined model for the warm Saturn HATS-6b as well as the resulting atmospheric solution and transmission spectra of HATS-6b are presented in Sect. 4.3. The discussion is in Sect. 4.4 and the conclusion in Sect. 4.5.

4.2 Methods

This study constructs a combined 3D cloudy atmosphere model for HATS-6b, by iteratively running a 3D GCM model and a detailed kinetic cloud formation model. After each iteration the disequilibrium gas-phase chemistry is calculated, and synthetic spectra are produced to assess the observable differences from iteration to iteration. The settings used to model HATS-6b and HATS-6 can be seen in Tab. 4.1, and the iterative procedure for running the models can be seen in Fig. 4.1.

4.2.1 Summary of general methods and iterative process

The GCM model used in this study is `expeRT/MITgcm` (Schneider et al., 2022b; Carone et al., 2020), that solves the hydrostatic primitive equations and radiaitve transfer throughout the atmospheric column over a global grid on a rotating sphere. `expeRT/MITgcm` is run based on chemical gas-phase concentrations cal-

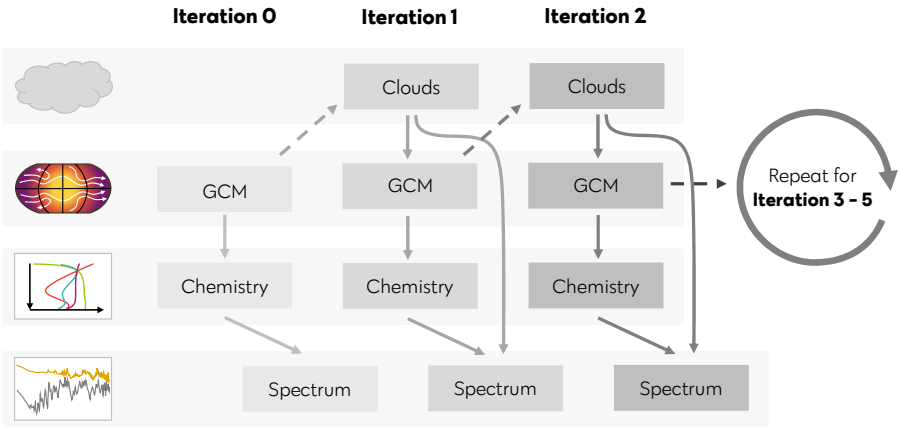

Figure 4.1: Iterative procedure applied in Kiefer et al. (submitted 2024). The four main models participating are illustrated on the left: Kinetic cloud formation model, `expeRT/MITgcm` to run GCMs, `ARGO/STAND2020` to model the disequilibrium chemistry, and `petitRADTRANS` as well as `gcm_toolkit` to produce spectra. to produce spectra. Six iterations were run in total: Iteration 0 without cloud formation, and Iteration 1-5 with clouds.

culated using the chemical equilibirum model `GGchem` (Woitke et al., 2018). After running the GCM for 2000 simulation days, a grid of 1D profiles for pressure, temperature, and vertical velocity are extracted from the GCM output. The profiles are extracted at the following coordinates for longitude: (ϕ = {-135°, -90°, -45°, 0°, 45°, 90°, 135°, 180° }) and latitude: (θ = {0°, 23°, 45°, 68°, 86°}).

The output profiles from `expeRT/MITgcm` are used as inputs for our kinetics cloud formation model. The model calculates the micro-physical cloud formation processes of nucleation, bulk growth, and evaporation, as well as gravitational settling, element depletion, and replenishment. The model considers four nucleating species (TiO_2, SiO, KCl, and NaCl) and 16 condensing species (TiO_2[s], Mg_2SiO_4[s], $MgSiO_3$[s], MgO[s], SiO[s], SiO_2[s], Fe[s], FeO[s], FeS[s], Fe_2O_3[s], Fe_2SiO_4[s], Al_2O_3[s], $CaTiO_3$[s], $CaSiO_3$[s], KCl[s], NaCl[s]). The model calculates the cloud particle composition, average particles size, and cloud particle number density, and these are fed back into `expeRT/MITgcm` as inputs for the opacity calculations.

As illustrated in Fig. 4.1, this approach of passing the outputs of the GCM as inputs to the cloud formation model and vice versa makes up for one iteration in the iterative approach. After each iteration, the disequilibrium chemistry is mod-

elled for eight 1D profiles extracted from the GCM. These methods are described in further detail in the next section.

To study the observable reliability of the iterative approach synthetic spectra are produced and compared. The spectra are produced using and `petitRADTRANS` (Mollière et al., 2019) and `gcm_toolkit` (Schneider et al., 2022a) based on the gas-phase concentrations from `ARGO/STAND2020` and the cloud opacities from the cloud formation model.

As can be seen in Fig. 4.1, a total of six iterations are performed. For Iteration 0, the GCM is run without a cloud formation input, resulting in a cloud-free model. For Iteration 1-5, the cloud formation is calculated based on the previous iteration and the results are implemented into the GCM runs. The iterative process is continued until the difference in the spectra of two consecutive iterations is so small that it would not be observable within the accuracy of the JWST instruments NIRSpec and MIRI LRS, which we will later show happened after 5 iterations in our study.

4.2.2 Methods for disequilibrium gas-phase chemistry

The disequilibrium chemistry for the H/C/N/O complex of HATS-6b is modelled to assess how each iteration affects the atmospheric chemistry, and as a result the transmission spectra. This is done using `ARGO` and `STAND2020` as described in Sec. 3.2.

The inputs for `ARGO` and STAND2020 have been chosen as follows:

1. ($T_{\rm gas}$, $p_{\rm gas}$) profiles and vertical eddy diffusion profile: Eight different 1D profiles are extracted from the output of the `expeRT/MITgcm` by averaging over areas of the 3D grid. The eight profiles are six terminator regions with the longitudes ($\phi = \{90^\circ, 270^\circ\}$) and latitudes ($\theta = \{0^\circ, 23^\circ, 68^\circ\}$), and the sub-stellar and anti-stellar points.

2. Atmospheric element abundances: Solar abundances adapted for metallicity ($[\mathrm{Fe/H}] = 0.2$) in accordance with the initial abundances used for the GCM.

3. Stellar XUV spectrum driving photochemistry: Spectrum obtained from the MUSCLES survey where the M1.5V star, GJ667C, is chosen as a proxy to HATS6 (shown in Fig. 3.2).

4. Cosmic rays: Implemented based on the ionization rate of low energy cosmic rays (LECR) as explained by Rimmer & Helling (2013) and Barth et al. (2021).

5. Stellar energetic particles: The solar SEP event has been scaled based on a X-ray flare intensity of $I_X = 0.1$ W m^{-2} at 1AU, in accordance with the description in Sec. 3.3.2.

As described in Sec. 3.3.4, the different locations on the planet will experience a different influx of stellar radiation and SEPs, and the model inputs are varied accordingly. For the sub-stellar point, both the stellar spectrum and SEPs are included. For the anti-stellar point, neither the stellar spectrum nor SEPs are included. For the terminator coordinates, only SEPs are included. The reasoning behind excluding the stellar spectrum for the terminator regions in this study, is that the shallow angle of incidence for radiation from the host star causes the radiation to pass through so much atmosphere before it reaches the bulk of the 1D simulated atmosphere profile that its influence is negligible. Since XUV radiation is easily scattered by the atmosphere, the stellar spectrum is not included for the terminator regions, whereas SEPs have been shown to penetrate deeper into the atmosphere (Barth et al., 2021) and are therefore included.

The output of STAND2020-ARGO is the relative concentration of more than 511 gas-phase species. Based on these concentrations and the cloud opacities from the cloud formation model, the transmission spectra can be produced.

4.3 Results

In this section I will present a summary of the general results of the study as well as a more detailed description of the results regarding the disequilibrium chemistry.

4.3.1 Summary of general results

The results from the GCM runs can be seen in Fig. 4.2 and 4.3. Fig. 4.2 shows P-T profiles extracted from each of the iterations of the GCM at the substellar, antistellar, morning, and evening terminator. Comparing the profiles for the cloudless model (Iteration 0) we notice that P-T structure is relatively similar across the different coordinates. Introducing clouds into the model (Iteration 1-5) creates a significant variation of the P-T profiles among the coordinates. Most noticeable

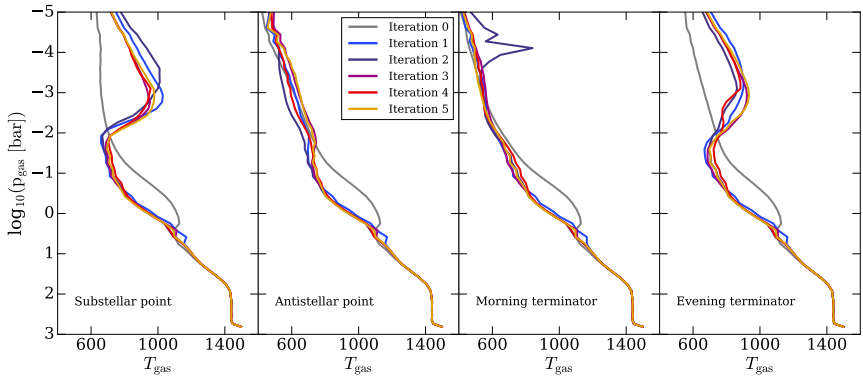

Figure 4.2: ($T_{\rm gas}$, $p_{\rm gas}$)-profiles of the sub-stellar point, anti-stellar point, evening terminator, and morning terminator.

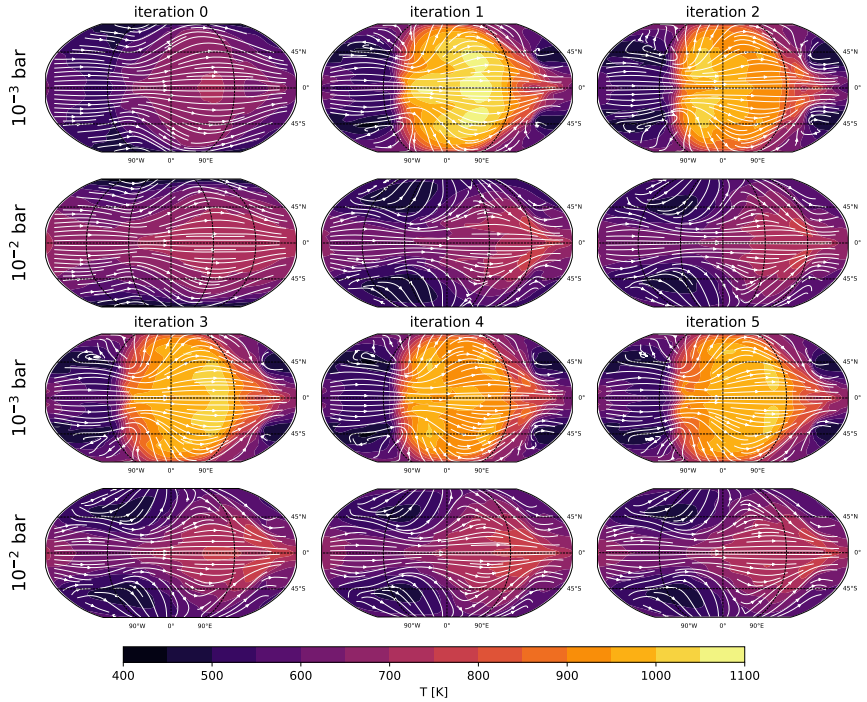

Figure 4.3: Isobaric slices of the `expeRT/MITgcm` runs at t = 2000 simulation days. The white lines indicate the horizontal wind velocity fields.

is a temperature inversion appearing at the substellar point and evening terminator in the upper atmosphere above 10^{-2} bar. Below the temperature inversion (10^{0} to 10^{-2} bar) we see a cooling of the atmosphere for the cloudy (Iteration

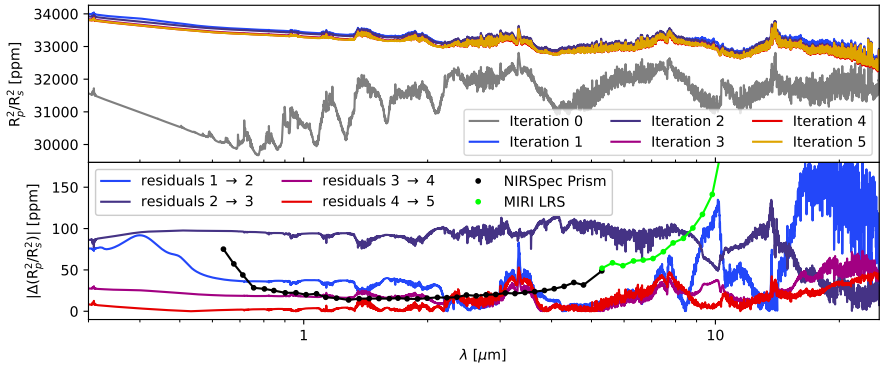

Figure 4.4: Comparison of the transmission spectra for the warm Saturn example HATS-6b for $\lambda = 0.3$ μm to 25 μm **Top:** Transmission spectrum for each iteration. **Bottom:** Absolute residuals between subsequent iterations and the spectral precision for JWST observations with NIRspec Prism and MIRI LRS for ten observed transits.

1-5) compared to the cloudless (Iteration 0) models, which can be explained by an anti-green house effect caused by the clouds. The cloud formation model revealed a significant cloud coverage over the entire exterior of HATS-6b (results can be seen in Kiefer et al. (submitted 2024)). These cloud layers reach into the upper atmospheres (at pressures lower than 10^{-3} bar), at considerable particle number densities and particle sizes. This high cloud deck might lead to scattering and absorption of the incoming radiation, thereby heating the upper atmosphere and preventing the radiation from reaching the lower atmosphere. The result is an anti-green house effect and over-all cooling of the lower atmosphere, in accordance with what we see from Fig. 4.2.

The only outlier among the cloudy models is the morning terminator for iteration 2, where a temperature increase of up to 350 K can be seen around 10^{-4} bar. This increase in temperature reduces the nucleation rate which in turn leads to fewer but larger particles (results can be seen in Kiefer et al. (submitted 2024)). The sudden change in the morning terminator is the result of dynamical instability caused by the cloud structure in this iteration which leads to hot air being advected from the day-side into the morning terminator. The general thermal instabilities of the morning terminator are discussed in more detail in Kiefer et al. (submitted 2024). While an instability is present in all cloudy iterations, it is more pronounced in iteration 2. Since no other iteration shows a similar behaviour, the temperature increase in the morning terminator of iteration 2 is considered an artefact of the specific configurations of the static clouds.

Fig. 4.3 shows isobaric slices over the global temperatures and horizontal wind

velocities from the GCM output. Slices are shown for two pressures (10^{-3} bar and 10^{-2} bar) for each of the six iterations. Looking at the cloudless model (Iteration 0) in the upper left corner we see a very uniform global temperature, with little difference between the two pressure points. For the cloudy models (Iteration 1-5) we see a significant heating on the dayside of the planet for the lower pressure (10^{-3} bar), that is not observed deeper in the atmosphere (10^{-2} bar). This again illustrates the heating of the upper atmosphere caused by the cloud layer. Furthermore, the cloudy models show a stronger and narrower equatorial wind jet than iteration 0 (results can be seen in Kiefer et al. (submitted 2024)). This matches the results of Baeyens et al. (2021), who showed that for the temperature range of warm Saturns (500 K to 1200 K) an increase in equilibrium temperature results in a faster and narrower jet. Furthermore, the weak polar jets of iteration 0 are not observed in the cloudy models.

The cloudy models all show the same general characteristics of: a temperature inversion around 10^{-3} bar, a cooling around 0.1 bar to 1 bar, a narrow equatorial wind jet, and global cloud coverage. However, the temperature between the iterations (Iteration 1-5) still vary by up to $\sim$130 K. Similarly, differences in the temperature structure around 10^{-3} bar can be seen in the isobaric plots (Fig. 4.3) and in the zonal mean winds (results can be seen in Kiefer et al. (submitted 2024)). The cloud particle properties on the other hand vary little between iterations 3, 4, and 5. In particular the nucleation rate between iteration 4 and 5 is close to identical. However, there are still changes in the cloud particle number density and average size between iteration 4 and 5. The observable effects of the changes in the temperature structures and cloud formation are shown in Fig. 4.4.

Transmission spectra were produced using the temperature structure of the GCM, the chemistry of ARGO, and the cloud structures. Spectra for all six iterations are shown in the top panel of Fig. 4.4. The residuals (difference in the relative transit depth) between consecutive iterations are shown in the bottom panel of the same figure. The bottom panel also shows the spectral precision for the JWST instruments NIRSpec Prism (Birkmann et al., 2022; Ferruit et al., 2022) and MIRI LRS (Kendrew et al., 2015, 2016). If we compare the residuals to the spectral precision we can see whether the differences between the iterations are observable: If the residuals are significantly larger than the spectral precision, the differences between the iterations are observable. If the residuals are of the same order or lower, the differences between the iterations will be difficult to observe.

There is a significant difference between the transmission spectra of iteration 0 and 1 due to the introduction of clouds in iteration 1 (top panel of Fig. 4.4). Iteration 1 shows more muted molecular features than iteration 0, especially for wavelengths below 2 μm. An additional increase in the relative transit depth is seen around 10 μm, indicating silicate species within the cloud particles. Both these effects are expected if clouds are present in exoplanet atmospheres (Wakeford & Sing, 2015; Powell et al., 2019; Grant et al., 2023).

The residuals between the cloudy iterations are generally below 100 ppm for wavelengths between 0.7 μm to 10 μm. The residuals can be related to shifts in the cloud top, which is defined as the pressure level at which clouds become optically thick (see e.g. Estrela et al., 2022). A clear CH_4 feature can be seen at 3 μm to 4 μm with a residual depth of around 100 ppm. This indicates that the differences between the ($T_{\rm gas}$, $p_{\rm gas}$) profiles for each iteration are still strong enough to significantly impact the disequilibrium chemistry of the planet, and that CH_4 might be particularly susceptible to these differences.

The residuals between iteration 4 to 5 are around 25 ppm, and consistently below the spectral precision of NIRSpec Prism (illustrated by the black data points). The only exception to this is the CH_4 feature around 3 μm to 4 μm, that still has a residual depth of around 50 ppm. However, even this feature is only slightly above the spectral precision, which will make detections difficult. Since the differences between the transmission spectra of iteration 3, 4, and 5 are close to or below the spectral precision of JWST NIRSpec Prism, we stop our iterative procedure after iteration 5.

4.3.2 Results for disequilibrium Chemistry

To assess the impact of the kinetic gas-phase chemistry and photo-chemistry on the observable atmosphere, and more specifically on the transmission spectra of HATS-6b, the disequilibrium chemistry was modelled. This is done for each iteration at six coordinates along the terminator region (longitudes ($\phi = \{90^\circ, 270^\circ\}$) and latitudes ($\theta = \{0^\circ, 23^\circ, 68^\circ\}$)). The resulting gas concentration profiles were averaged over the six coordinates. The relative number densities ($n_i/n_{\rm gas}$) of H, H_2, CO, CO_2, H_2O, CH_4, HCN, and NH_3 can be seen in Fig. 4.5 (top). These eight molecules have been chosen due to their high concentrations in the atmospheres or because they are some of the more interesting atmospheric species when looking at the effects of external radiation (e.g. Barth et al. (2021); Baeyens et al.

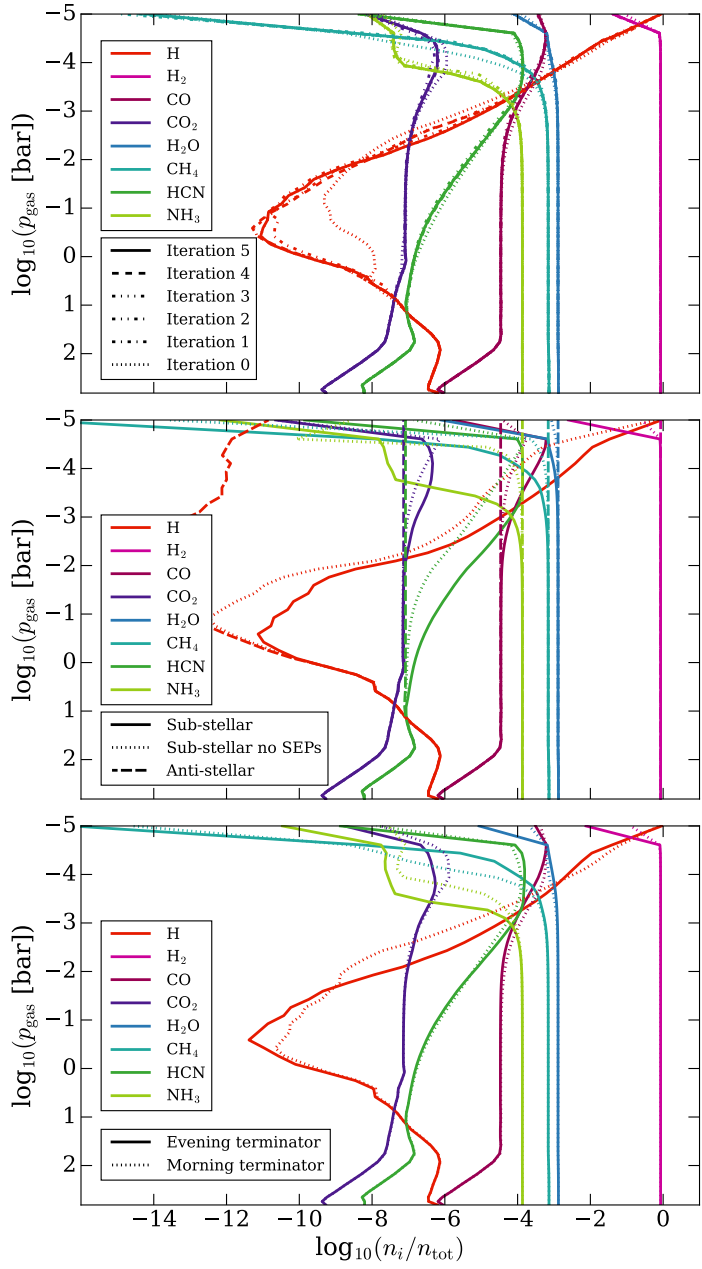

Figure 4.5: Concentrations of non-equilibrium gas species for the warm Saturn example HATS-6b. Top: Complete terminator region (both morning and evening) averaged over all six coordinates for all iterations. Middle: Sub- and anti-stellar point for the final iteration (Iteration 5). Bottom: Morning and evening terminators for the final iteration (Iteration 5).

(2022)). The concentration profiles show very little variation among the five iterations with clouds, whereas the difference between the cloudless (iteration 0) and cloudy iterations (1 - 5) is somewhat larger. The largest differences between the cloudless and cloudy iterations occur between $p_{\rm gas} \sim 10^{-2}$ - 10^{0} bar (Fig. 4.5, top). This pressure range corresponds to the cloud-induced cooling of the lower atmosphere observed in iterations 1 - 5 (as described in Sec. 4.3.1). Some species (e.g. NH_3, CO_2, and CH_4) also show a difference between cloudy and cloudless at lower pressures corresponding to a cloud-induced heating of the upper atmosphere in iterations 1 - 5. The cloud-induced heating in the upper atmosphere in combination with a cooling of the lower atmosphere comprises the temperature inversion (see Fig. 4.2).

The chemical variations along the equator are illustrated in Fig. 4.5 middle (sub-stellar and anti-stellar point) and bottom (morning and evening terminator). Comparing these two figures we notice that the relative number densities of all species show significantly larger differences between the day- and night-side (the solid and the dashed lines in Fig. 4.5, middle) than the differences between the different iterations (all lines in Fig.4.5, top).

The variations along the equator are caused both by differences in the ($T_{\rm gas}$, $p_{\rm gas}$) profiles for the four coordinates, and by differences in the stellar XUV radiation and the SEPs. The sub-stellar point is irradiated both by XUV radiation and SEPs, the terminators are irradiated only by SEPs, and the anti-stellar point is irradiated by neither. Comparing the four cases it can be seen that the sub-stellar point and the two terminators are relatively similar, whereas the anti-stellar point differs significantly from the rest. By comparing the sub- and anti-stellar point, we notice a steep decrease in the concentration of many of the gas species at the sub-stellar point (incl. H_2, CH_4, and NH_3) in the upper atmosphere, indicating a break down of these molecules through photolysis by the XUV radiation or ionisation by the SEPs. Other species (such as H, HCN, and partly CO and CO_2) show an increase in concentration for the sub-stellar point compared to the anti-stellar point as we move further up into the atmosphere, indicating that these are positively influenced by photochemical reactions. Comparing model runs for the sub-stellar point with and without SEPs (Fig. 4.5, middle), we notice a significant contribution by the SEPs on the gas-phase concentrations and that this effect reaches far down into the atmosphere. The middle and bottom plots in Fig. 4.5 show that the sub-stellar point with SEPs bear a strong resemblance to the terminator regions, which could indicate that SEPs can have a larger effect than the XUV radiation on

the concentrations of the gas species, including observationally interesting species such as CH_4 and HCN. The bottom plot Fig. 4.5 shows that the differences between the terminator regions are generally higher at lower pressures, with the exception of H that also show differences deeper into the atmosphere.

As mentioned in Sect. 1.3.1, M-dwarf stars such as HATS-6 are known to have higher magnetic activities compared to more massive stars like the Sun. This increased activity leads to increased amounts of SEPs. As explained in Sect. 1.3.1, the amount of SEPs has been found to scale with the X-ray flare intensity of the star, which for M-dwarf stars has been reported to range from 0.001 to 0.2 Wm^{-2} at 1AU (listed in Tab. 3.4 in Chapter 3). In this study we scale our SEP spectrum based on a X-ray flare intensity of 0.1 Wm^{-2} at 1AU, indicating that the amount of SEPs could be significantly higher than what we show, leading to a greater impact on the disequilibrium gas-phase chemistry.

4.4 Discussion

In this work we combine detailed models for 3D climate simulations, micro-physical cloud formation, and disequilibrium chemistry calculations, and apply them to the warm Saturn HATS-6b. In this section, we will relate some of our findings to precious work regarding the anti-greenhouse effect (Sect. 4.4.1) and the study of warm Saturns (Sect. 4.4.2).

4.4.1 Anti-greenhouse effect

We observe a temperature inversion for HATS-6b when we include cloud formation in our models that is not present in the cloudless model. We find that the clouds in the upper atmosphere of HATS-6b ($P < 10^{-3}$ bar) have considerable cloud particle sizes and number densities. The high cloud deck scatters and absorbs incoming short-wavelength radiation, which cools the layers below the clouds while heating the upper layers. This causes the temperature inversion, also known as the anti-greenhouse effect. An anti-greenhouse effect was first observed on Titan (McKay et al., 1991) and has been predicted for exoplanets with extensive clouds or hazes (Heng et al., 2012; Morley et al., 2012; Steinrueck et al., 2023).

Direct observation of a temperature inversion requires emission from the lower atmosphere to escape into space, but due to the dense cloud layer in between this is most likely impossible. In order to gain information from the cooler lower lay-

ers, we would therefore need an upwelling of material through the cloud deck. Fig. 4.4 shows a CH_4 feature that is visible despite the cloud layer, which indicates that the CH_4 extends into the upper layers of the atmosphere. In the upper atmosphere, CH_4 is exposed to photolysis and high degrees of SEPs, and since CH_4 is very susceptible to photochemical reactions (Moses et al., 2011; Line et al., 2011; Baeyens et al., 2021, 2022; Konings et al., 2022), the molecule cannot be stable above the cloud deck. A visible CH_4 feature could therefore indicate that vertical mixing has connected the observable gas-phase chemistry above the clouds to deeper atmosphere layers, thereby forming a probe through the temperature inversion and into the layers cooled by the anti-greenhouse effect (Agundez et al., 2014; Fortney et al., 2020). This work confirmed the influence of stellar energetic particles (SEP) on the dayside chemistry of a planet around a relatively active star, as was already pointed out by Barth et al. (2021) for HD 189733b.

4.4.2 Comparison to other models

The cloud structure and climate of HATS-6b were simulated as a first example of a warm Saturn around an M-dwarf host star. To extend our findings from HATS-6b to general warm Saturns, the results are compared to other studies focusing on 3D cloud and climate structures of warm Saturn-type exoplanets.

Helling et al. (2023) conducted a grid study of post-processed cloud structures for temperatures between 400 K and 2600 K for F, G, K and M-dwarf stars based on a previous study by Baeyens et al. (2022). For exoplanets with an equilibrium temperature of 700 K around M-dwarf stars (corresponding to HATS-6b), they predict strong uniform cloud coverage. HATS-6b thereby falls into their "class (i)" category of planets, characterized by global, mainly homogenous cloud coverage. Our findings suggest that this cloud coverage might cause an anti-greenhouse effect for these "class (i)" planets around M-dwarf stars.

Christie et al. (2022) studied the impact of clouds on the climate of the warm Neptune, GJ 1214b. They model phase equilibrium clouds with KCl and ZnS as their cloud particle material in line with similar studies of cloud composition of GJ 1214b (Gao & Benneke, 2018; Ormel & Min, 2019). Christie et al. (2022) found that clouds cause cooling in the lower atmosphere, matching our results, but did not observe a significant upper-atmosphere temperature increase.

Another planet similar to HATS-6b, is the Saturn-mass exoplanet WASP-39b that is part of the JWST Early Release Science program (Feinstein et al., 2023;

Ahrer et al., 2023; Rustamkulov et al., 2023; Alderson et al., 2023; JWST Transiting Exoplanet Community Early Release Science-Team et al., 2023). WASP-39b is at the upper limit of the "class (i)" (Helling et al., 2023) with $T_{\rm eq} \sim 1100$ K. Similar to HATS-6b, cloudless GCMs of WASP-39b show small day-night temperature differences, and post-processed cloud modeling predicts global cloud coverage (Carone et al., 2023; Lee et al., 2023). Pre-JWST observations indicated a relatively cloud-free atmosphere (Sing et al., 2016; Nikolov et al., 2016; Fischer et al., 2016; Wakeford et al., 2018), but JWST revised these findings, indicating cloud presence with some models suggesting inhomogeneous cloud coverage (Feinstein et al., 2023). JWST observations could reveal cloud asymmetries between the morning and evening terminator, as predicted by Carone et al. (2023), in line with our findings in this study.

4.5 Summary

In this study we explore the global climate, cloud formation, and gas-phase chemistry of the warm Saturn HATS-6b orbiting an M-dwarf star. This is done using a combined model in the form of step-wise iterations between a 3D GCM with full radiative transfer and deep atmosphere extension (`expeRT/MITgcm`) and a detailed cloud formation description. At the end of each iteration the resulting atmosphere profiles are used to calculate the disequilibrium chemical composition using a kinetics chemical network, `ARGO/STAND2020`. We demonstrate how the combined modelling approach can help to interpret the data from space missions, such as JWST, for warm Saturn type planets.

Our findings relating to the case study of HATS-6b are as follows:

- We find a global cloud coverage on HATS-6b, which is to be expected for temperature range (500 K < T < 1200 K) of warm Saturn type exoplanets.
- We find that cloud formation causes a temperature inversion in the upper atmosphere ($p < 10^{-2}$ bar) at the substellar point and evening terminator. Cloud particles in the upper atmosphere cause a cooling of the lower atmosphere (10^{-2} bar $< p <$ 1 bar) consistent with an anti-greenhouse effect.
- We find that cloud formation leads to a stronger and narrower equatorial jet.
- We find that cloud formation leads to a characteristically flat transmission

spectrum in the optical, while there are molecular absorption features for CO_2CH_4 and H_2O in the infrared.

- We find a silicate cloud feature in the transmission spectra around 10 μm.
- We find that concentration of many gas-phase molecules is affected by photochemistry in the upper atmosphere.
- We find that stellar energetic particles affect the concentration of many gas-phase molecules, including observationally interesting species such as CH_4 and HCN, and that this effect reaches deep into the atmosphere.

The small radii of M-dwarf stars compared to more massive stars lead the to a 'magnifying effect' of spectral features within transmission spectra. This makes planets like HATS-6b prime targets for deciphering gas chemistry and cloud compositions for warm Saturn type exoplanets. For wavelengths up to 8 μm, it may even be possible to identify morning and evening terminator differences with the CH_4 feature around 3 μm.

Our findings relating the iterative modelling approach are as follows:

- We find that it takes five iterations between the GCM and the cloud model, before the differences in the atmospheric structure of HATS-6b drop below the observational accuracy of the JWST NIRSpec Prism and MIRI LRS.
- We find that the difference between the synthetic spectrum of the first iteration (GCM → Clouds → GCM) and the fifth iteration differs by less than 200ppm.
- We find that the differences between the spectra of the morning and evening terminators are larger than the differences between each iteration.
- We find a greater variation in chemical composition between the day- and night side of the planet, than between the different cloudy iterations.

We propose that a combined model that enables the full complexity of all modelling components (here 3D GCM, cloud formation, and disequilibrium chemistry) can be useful for the interpretation of observational data for exoplanets to be studied with CHEOPS, JWST, and also ELT, PLATO, and Ariel in the future.

Due to their expected cloud coverage and deep transits, warm Saturns are prime candidates for studying cloud particle composition and cloud-induced thermal inversions. Limb asymmetry studies could be particularly useful for examining the feedback of clouds on the atmospheric structure, and the resulting effect on the gas-phase chemistry and cloud top. By combining models iteratively allows us to gain the full physical complexity of each model in a computationally feasible manner that enables a detailed interpretation of observational data within the accuracy of JWST NIRSpec and MIRI LRS.

5

Summary & Outlook

5.1 Summary

This thesis has explored some of the effects of high-energy radiation on exoplanet atmospheres. We have done this on through two approaches: experiments on cloud particles, and modelling of atmospheric chemistry. In this section I would like to summarize our work as well as the main conclusions.

Chapter 2 - High-energy radiation and mineral cloud particles

This chapter investigated the effect of gamma radiation on mineral cloud particles in an atmosphere chamber. Gamma radiation is one of the main products in the interaction between high-energy particles and the atmosphere, and the mineral particles investigated were SiO_2 particles that are known as a cloud species on gaseous exoplanets and act as cloud condensation nuclei here on Earth.

We found that the SiO_2 particles naturally cluster to form aggregates, and that this aggregation was inhibited by gamma radiation. Gamma radiation was also found to charge the particles negatively.
Our findings suggest that high-energy radiation might favour the formation of a high number of small rather than a lower number of large particles.

Chapter 3 - High-energy radiative environments and atmospheric chemistry

This chapter investigated the effect of different types of high-energy radiation on atmospheric chemistry. We focused on XUV radiation and stellar energetic particles (SEP) from the host stars, as well as galactic cosmic rays (GCR) from outside the system.
We found that all three types of high-energy radiation can affect the concentration of key molecular species in the atmosphere, but that XUV is generally the most impactful. Our findings suggest that SEP might especially affect the carbon chemistry of the atmosphere, while GCR mainly affect the concentration of ions.

Chapter 4 - Cloud formation on warm Saturn around M-dwarf star

This chapter investigated an iterative approach to combine a cloud formation model with a 3D general circulation model (GCM). For each iteration the disequilibrium chemistry of the atmosphere was modelled and synthetic spectra were produced. This study was done on the warm-Saturn planet, HAST-6b, that orbits an M-dwarf star. HATS-6b is an interesting case since its size and type of host star makes it a great target for studying the effect of stellar activity on exoplanet atmospheres through both models and observations.
We found that after five iterations between the cloud model and GCM, the changes in the spectra are no longer observable within JWST accuracy. Additionally, the chemical variations across the planet are larger than the variations between the different iterations. We found that the chemical composition of the atmosphere is significantly affected by photochemistry and that SEP affect the concentration of observationally interesting species.
We propose that a combined modelling approach can allow the full complexity of each model, while yielding results that are accurate within the limits of state-of-the-art telescopes.

5.2 Outlook

The time frame of a PhD project is surprisingly short, and while a lot of work has been done there is still much left to do. In this section, we would like to describe the next natural steps in our work, as well as potential projects that could be done in the future.

Identifying molecular tracers for high-energy radiation

As mentioned in Chapter 3, the work presented there in an ongoing study, and our next planned step is to identify observable molecular tracers. As described in Sec. 3.4.2 we determine which species are most affected by the different types of high-energy radiation by calculating the differences in the concentration of each species between models with and without the radiative input. In these calculations, we have a cutoff where we exclude species with a maximum relative concentration change of less than 10^{-30}, since these concentrations are too low to be observed. However, despite this cutoff, we still see a lot of species with very low concentrations, and many of the species showcased throughout the chapter will probably not be observable. Next, we plan to increase the cut-off concentration, and systematically go through the species to identify the ones that are most affected by the radiation while having the highest chances of being observable according to existing literature. The observability of these species can be tested using similar methods to the ones by Kiefer et al. (2024) explained in Chapter 4. Here synthetic spectra were produced from different models, and it was tested if changes between models are observable within e.g. the accuracy of JWST instruments. This will allow us to identify tracer molecules that can be used by observation studies to accurately interpret their data or give indications about the radiative environment of the planets.

Accurately calculating ionization in different environments

In Chapter 3 we investigated the effect of different types of high-energy radiation by scaling ionization profiles calculated by other studies (e.g. Rimmer & Helling (2013) and Rab et al. (2017)). This allowed us to explore the parameter space for the radiation, but did not provide a fully accurate representation of the radiative environment within each type of system. As discussed in Sec. 3.5, we believe it might be beneficial for a future study to fully model the expected ionization profiles for atmospheres in different systems. To do this one would have to account

for e.g. 1) Variations in GCR spectrum for different galactic environments. 2) Modulation of energetic particles (stellar or cosmic) through the astrosphere (e.g. Rodgers-Lee et al. (2021a)). 3) Modulation of energetic particles through the planetary magnetic field (e.g. Grießmeier et al. (2015)). 4) Propagation and ionization by energetic particles through the atmosphere (e.g. Rimmer & Helling (2013)).

Exploring the full range of SEP intensities

In Chapter 3 we studied the effect of SEP for three different host star types, M-, K-, and G-type. The ionization caused by SEP was calculated based on proton densities scaled from observed X-ray flare luminosities, in accordance with the methods by Rab et al. (2017) and Barth et al. (2021). Each host stellar type was represented by one X-ray flare luminosity, as indicated in Tab. 3.3. However, stars within the same stellar type can have a wide range of stellar activity, as illustrated by the X-ray flares measures for M-dwarfs and listed in Tab. 3.4. In addition to this some F- and A-type stars have also been known to have flare-like activity (e.g. Balona (2012)), but since this is not believed to be a regular occurrence we did not include SEP for these stellar types in the study. We believe it could be beneficial for a future study to look into the effect of the full range of SEP intensities by scaling the SEP ionization based on all measured X-ray flare intensities for as many stellar types as possible.

Expanding the aggregation and charging study to other mineral species

In Chapter 2 we studied the aggregation and charging of SiO_2 particles as representative of mineral cloud particles. However, a number of other mineral particles are expected to form clouds in exoplanet atmospheres, including TiO_2, SiO, and NaCl (e.g. Bromley et al. (2016); Sindel et al. (2022); Helling (2022)). Due to a time constraint, we did not have time to test the behaviour of these other mineral particles, but we believe it could be beneficial for other studies to do so. By repeating the experiments with other cloud species we would be able to recognize if the observed trends are general for mineral particles or specific for SiO_2.

Bibliography

2024, Athena X-ray observatory - Athena X-ray observatory |. https://www.the-athena-x-ray-observatory.eu/en

Abedini, A., Daud, A. R., Abdul Hamid, M. A., Kamil Othman, N., & Saion, E. 2013, Nanoscale Research Letters, 8, 474, doi: 10.1186/1556-276X-8-474

Acero, F., Ackermann, M., Ajello, M., et al. 2016, The Astrophysical Journal Supplement Series, 223, 26, doi: 10.3847/0067-0049/223/2/26

Adriani, O., Barbarino, G. C., Bazilevskaya, G. A., et al. 2013, The Astrophysical Journal, 765, 91, doi: 10.1088/0004-637X/765/2/91

Aguirre, F. C., France, K., Nell, N., et al. 2023, The Radiation Environments of Middle-Aged F-Type Stars, arXiv, doi: 10.48550/arXiv.2308.04980

Agundez, M., Parmentier, V., Venot, O., Hersant, F., & Selsis, F. 2014, A&A, 564, A73, doi: 10.1051/0004-6361/201322895

Aharonian, F., Peron, G., Yang, R., Casanova, S., & Zanin, R. 2020, Physical Review D, 101, 083018, doi: 10.1103/PhysRevD.101.083018

Ahrer, E.-M., Stevenson, K. B., Mansfield, M., et al. 2023, Nature, 614, 653, doi: 10.1038/s41586-022-05590-4

Airapetian, V. S., Barnes, R., Cohen, O., et al. 2020, International Journal of Astrobiology, 19, 136, doi: 10.1017/S1473550419000132

Alderson, L., Wakeford, H. R., Alam, M. K., et al. 2023, Nature, 614, 664, doi: 10.1038/s41586-022-05591-3

Alfvén, H. 1942, Nature, 150, 405, doi: 10.1038/150405d0

Allard, F. 2016

Armillotta, L., Ostriker, E. C., & Jiang, Y.-F. 2022, The Astrophysical Journal, 929, 170, doi: 10.3847/1538-4357/ac5fa9

Asay, D. B., & Kim, S. H. 2005, The Journal of Physical Chemistry B, 109, 16760, doi: 10.1021/jp053042o

Astudillo-Defru, N., Delfosse, X., Bonfils, X., et al. 2017, Astronomy and Astrophysics, 600, A13, doi: 10.1051/0004-6361/201527078

Bach-Møller, N., Helling, C., Jørgensen, U. G., & Enghoff, M. B. 2024, The Astrophysical Journal, 962, 87, doi: 10.3847/1538-4357/ad13ef

Bach-Møller, N., & Jørgensen, U. G. 2020, Monthly Notices of the Royal Astronomical Society, 500, 1313, doi: 10.1093/mnras/staa3321

Baeyens, R., Decin, L., Carone, L., et al. 2021, Monthly Notices of the Royal Astronomical Society, 505, 5603, doi: 10.1093/mnras/stab1310

Baeyens, R., Konings, T., Venot, O., Carone, L., & Decin, L. 2022, Monthly Notices of the Royal Astronomical Society, 512, 4877, doi: 10.1093/mnras/stac809

Baines, K. H., Delitsky, M. L., Momary, T. W., et al. 2009, Planetary and Space Science, 57, 1650, doi: 10.1016/j.pss.2009.06.025

Baker, D. N., Mason, G. M., & Mazur, J. E. 2012, Eos, Transactions American Geophysical Union, 93, 325, doi: 10.1029/2012EO340001

Balona, L. A. 2012, Monthly Notices of the Royal Astronomical Society, 423, 3420, doi: 10.1111/j.1365-2966.2012.21135.x

Barth, P., Helling, C., Stüeken, E. E., et al. 2021, Monthly Notices of the Royal Astronomical Society, 502, 6201, doi: 10.1093/mnras/staa3989

Bazilevskaya, G. A., Usoskin, I. G., Flückiger, E. O., et al. 2008, Space Science Reviews, 137, 149, doi: 10.1007/s11214-008-9339-y

Bean, J. L., Raymond, S. N., & Owen, J. E. 2021, Journal of Geophysical Research: Planets, 126, e2020JE006639, doi: 10.1029/2020JE006639

Bean, J. L., Stevenson, K. B., Batalha, N. M., et al. 2018, Publications of the Astronomical Society of the Pacific, 130, 114402, doi: 10.1088/1538-3873/aadbf3

Belov, A., Garcia, H., Kurt, V., & Mavromichalaki, E. 2005, Cosmic Research, 43, 165, doi: 10.1007/s10604-005-0031-7

Berdyugina, S. V. 2005, Living Reviews in Solar Physics, 2, 8, doi: 10.12942/lrsp-2005-8

Birkmann, S. M., Ferruit, P., Giardino, G., et al. 2022, A&A, 661, A83, doi: 10.1051/0004-6361/202142592

Bisschoff, D., Potgieter, M. S., & Aslam, O. P. M. 2019, The Astrophysical Journal, 878, 59, doi: 10.3847/1538-4357/ab1e4a

Bohn, H. U. 1984, Astronomy and Astrophysics, 136, 338. https://ui.adsabs.harvard.edu/abs/1984A&A...136..338B

Bourrier, V., Wheatley, P. J., Lecavelier des Etangs, A., et al. 2020, Monthly Notices of the Royal Astronomical Society, 493, 559, doi: 10.1093/mnras/staa256

Bouvier, J., Matt, S. P., Mohanty, S., et al. 2014, Protostars and planets VI, 433, 94

Branduardi-Raymont, G., Sciortino, S., Dennerl, K., et al. 2013, The Hot and Energetic Universe: Solar system and exoplanets, arXiv, doi: 10.48550/arXiv.1306.2332

Brasseur, G. P., & Solomon, S. 2005, Aeronomy of the middle atmosphere: Chemistry and physics of the stratosphere and mesosphere, Vol. 32 (Springer Science & Business Media)

Bromley, S. T., Martín, J. C. G., & Plane, J. M. C. 2016, Physical Chemistry Chemical Physics, 18, 26913, doi: 10.1039/C6CP03629E

Brooke, T., Knacke, R., Encrenaz, T., et al. 1998, Icarus, 136, 1

Brown, M. E., Bouchez, A. H., & Griffith, C. A. 2002, Nature, 420, 795

Buchhave, L. A., Bitsch, B., Johansen, A., et al. 2018, The Astrophysical Journal, 856, 37, doi: 10.3847/1538-4357/aaafca

Burcat, A., & Ruscic, B. 2005, doi: 10.2172/925269

Carone, L., Lewis, D. A., Samra, D., Schneider, A. D., & Helling, C. 2023, WASP-39b: exo-Saturn with patchy cloud composition, moderate metallicity, and underdepleted S/O, arXiv. http://arxiv.org/abs/2301.08492

Carone, L., Baeyens, R., Mollière, P., et al. 2020, MNRAS, 496, 3582, doi: 10.1093/mnras/staa1733

Carone, L., Mollière, P., Zhou, Y., et al. 2021, Astronomy & Astrophysics, 646, A168, doi: 10.1051/0004-6361/202038620

Castelli, F., & Kurucz, R. L. 2003, 210, A20, doi: 10.48550/arXiv.astro-ph/0405087

Cañas, C. I., Kanodia, S., Bender, C. F., et al. 2022, The Astronomical Journal, 164, 50, doi: 10.3847/1538-3881/ac7804

Chadney, J. M., Koskinen, T. T., Galand, M., Unruh, Y. C., & Sanz-Forcada, J. 2017, Astronomy & Astrophysics, 608, A75, doi: 10.1051/0004-6361/201731129

Chapman, S., & Cowling, T. G. 1990, The Mathematical Theory of Non-uniform Gases: An Account of the Kinetic Theory of Viscosity, Thermal Conduction and Diffusion in Gases (Cambridge University Press)

Chien, C.-H., Cheng, M.-D., Im, P., et al. 2022, International Communications in Heat and Mass Transfer, 130, 105745, doi: 10.1016/j.icheatmasstransfer.2021.105745

Christensen-Dalsgaard, J., & Aguirre, V. S. 2018, 1679–1696, doi: 10.1007/978-3-319-55333-7_184

Christie, D. A., Mayne, N. J., Gillard, R. M., et al. 2022, MNRAS, 517, 1407, doi: 10.1093/mnras/stac2763

Crossfield, I. J. M. 2015, PASP, 127, 941, doi: 10.1086/683115

Cummings, A. C., Stone, E. C., Heikkila, B. C., et al. 2016, The Astrophysical Journal, 831, 18, doi: 10.3847/0004-637X/831/1/18

Dawson, R. I., & Johnson, J. A. 2018, Annual Review of Astronomy and Astrophysics, 56, 175, doi: 10.1146/annurev-astro-081817-051853

Dean, A., Fan, L., & Byard. 1988

Demory, B.-O., Wit, J. d., Lewis, N., et al. 2013, ApJL, 776, L25, doi: 10.1088/2041-8205/776/2/L25

Deng, J., Du, Z., Karki, B. B., Ghosh, D. B., & Lee, K. K. M. 2020, Nature Communications, 11, 2007, doi: 10.1038/s41467-020-15757-0

Dickinson, R. E. 1975, Bulletin of the American Meteorological Society, 56, 1240, doi: 10.1175/1520-0477(1975)056<1240:SVATLA>2.0.CO;2

Doyle, L., Ramsay, G., Doyle, J. G., Wu, K., & Scullion, E. 2018, Monthly Notices of the Royal Astronomical Society, 480, 2153, doi: 10.1093/mnras/sty1963

Duvvuri, G. M., Pineda, J. S., Berta-Thompson, Z. K., et al. 2021, arXiv:2102.08493 [astro-ph]. http://arxiv.org/abs/2102.08493

Dyrek, A., Min, M., Decin, L., et al. 2023, SO2, silicate clouds, but no CH4 detected in a warm Neptune with JWST MIRI, doi: 10.21203/rs.3.rs-3101058/v1

Engelbrecht, N. E., Herbst, K., Strauss, R. D. T., et al. 2024, The Astrophysical Journal, 964, 89, doi: 10.3847/1538-4357/ad2ade

Enghoff, M. B., Pedersen, J. O. P., Uggerhøj, U. I., Paling, S. M., & Svensmark, H. 2011, Geophysical Research Letters, 38, doi: 10.1029/2011GL047036

Enghoff, M. B., & Svensmark, J. 2017, Journal of Aerosol Science, 114, 13, doi: 10.1016/j.jaerosci.2017.08.009

Enskog, D. 1917, Kinetische Theorie der Vorgaenge in maessig verduennten Gasen. I. Allgemeiner Teil. https://ui.adsabs.harvard.edu/abs/1917ktvm.book.....E

Estrela, R., Swain, M. R., & Roudier, G. M. 2022, ApJL, 941, L5, doi: 10.3847/2041-8213/aca2aa

Fan, J., Rosenfeld, D., Zhang, Y., et al. 2018, Science, 359, 411, doi: 10.1126/science.aan8461

Fares, R., Bourrier, V., Vidotto, A. A., et al. 2017, Monthly Notices of the Royal Astronomical Society, 471, 1246, doi: 10.1093/mnras/stx1581

Feinstein, A. D., Radica, M., Welbanks, L., et al. 2023, Nature, 614, 670, doi: 10.1038/s41586-022-05674-1

Ferreira, S. E. S., & Potgieter, M. S. 2004, Advances in Space Research, 34, 115, doi: 10.1016/j.asr.2003.02.057

Ferruit, P., Jakobsen, P., Giardino, G., et al. 2022, A&A, 661, A81, doi: 10.1051/0004-6361/202142673

Firoz, K. A., Gan, W. Q., Li, Y. P., Rodríguez-Pacheco, J., & Dorman, L. I. 2022, Solar Physics, 297, 71, doi: 10.1007/s11207-022-01994-7

Fischer, P. D., Knutson, H. A., Sing, D. K., et al. 2016, ApJ, 827, 19, doi: 10.3847/0004-637X/827/1/19

Fortney, J. J., Visscher, C., Marley, M. S., et al. 2020, AJ, 160, 288, doi: 10.3847/1538-3881/abc5bd

Fossati, L., Koskinen, T., Lothringer, J. D., et al. 2018, The Astrophysical Journal, 868, L30, doi: 10.3847/2041-8213/aaf0a5

France, K., Loyd, R. O. P., Youngblood, A., et al. 2016, The Astrophysical Journal, 820, 89, doi: 10.3847/0004-637X/820/2/89

Fraschetti, F., Drake, J. J., Alvarado-Gómez, J. D., et al. 2019, The Astrophysical Journal, 874, 21, doi: 10.3847/1538-4357/ab05e4

Fuchs, N. A., Daisley, R. E., Fuchs, M., Davies, C. N., & Straumanis, M. E. 1965, Physics Today, 18, 73, doi: 10.1063/1.3047354

Fujimoto, T., Yamanaka, S., & Kuga, Y. 2021, MATEC Web of Conferences, 333, 02012, doi: 10.1051/matecconf/202133302012

Gao, P., & Benneke, B. 2018, ApJ, 863, 165, doi: 10.3847/1538-4357/aad461

Gao, P., & Powell, D. 2021, The Astrophysical Journal Letters, 918, L7, doi: 10.3847/2041-8213/ac139f

Gao, P., Wakeford, H. R., Moran, S. E., & Parmentier, V. 2021, Journal of Geophysical Research: Planets, 126, e2020JE006655, doi: 10.1029/2020JE006655

Gao, P., Thorngren, D. P., Lee, E. K. H., et al. 2020, Nat. Astron., 4, 951, doi: 10.1038/s41550-020-1114-3

García Muñoz, A. 2007, Planetary and Space Science, 55, 1426, doi: 10.1016/j.pss.2007.03.007

Giacobbe, P., Brogi, M., Gandhi, S., et al. 2021, Nature, 592, 205, doi: 10.1038/s41586-021-03381-x

Goldberg, M., & Batygin, K. 2022, The Astronomical Journal, 163, 201, doi: 10.3847/1538-3881/ac5961

Grant, D., Lewis, N. K., Wakeford, H. R., et al. 2023, ApJL, 956, L29, doi: 10.3847/2041-8213/acfc3b

Grießmeier, J.-M., Stadelmann, A., Motschmann, U., et al. 2005, Astrobiology, 5, 587, doi: 10.1089/ast.2005.5.587

Grießmeier, J.-M., Tabataba-Vakili, F., Stadelmann, A., Grenfell, J. L., & Atri, D. 2015, Astronomy & Astrophysics, 581, A44, doi: 10.1051/0004-6361/201425451

Grün, E., Fechtig, H., Hanner, M. S., et al. 1992, Space Science Reviews, 60, 317, doi: 10.1007/BF00216860

Guinan, E. F., Engle, S. G., & Durbin, A. 2016, The Astrophysical Journal, 821, 81, doi: 10.3847/0004-637X/821/2/81

Guo, Y.-Q., & Yuan, Q. 2018, Physical Review D, 97, 063008, doi: 10.1103/PhysRevD.97.063008

Gustafsson, B., Edvardsson, B., Eriksson, K., et al. 2008, Astronomy & Astrophysics, 486, 951, doi: 10.1051/0004-6361:200809724

Hainich, R., Ramachandran, V., Shenar, T., et al. 2019, Astronomy and Astrophysics, 621, A85, doi: 10.1051/0004-6361/201833787

Harada, N., Herbst, E., & Wakelam, V. 2010, The Astrophysical Journal, 721, 1570, doi: 10.1088/0004-637X/721/2/1570

Harnden, Jr., F. R., Branduardi, G., Elvis, M., et al. 1979, The Astrophysical Journal, 234, L51, doi: 10.1086/183107

Harrison, R. G., & Carslaw, K. S. 2003, Reviews of Geophysics, 41, doi: 10.1029/2002RG000114

Hartman, J. D., Bayliss, D., Brahm, R., et al. 2015, The Astronomical Journal, 149, 166, doi: 10.1088/0004-6256/149/5/166

He, Y., Gu, Z., Lu, W., et al. 2019, Atmospheric Environment, 197, 141, doi: 10.1016/j.atmosenv.2018.10.035

—. 2020, Particuology, 52, 1, doi: 10.1016/j.partic.2019.12.007

Heintzenberg, J. 1994, Aerosol Science and Technology, 21, 46, doi: 10.1080/02786829408959695

Helling, C. 2019, Annual Review of Earth and Planetary Sciences, 47, 583, doi: 10.1146/annurev-earth-053018-060401

—. 2020, arXiv:2011.03302 [astro-ph, physics:physics]. http://arxiv.org/abs/2011.03302

—. 2022, Cloud formation in Exoplanetary Atmospheres, Tech. Rep. arXiv:2205.00454, arXiv. http://arxiv.org/abs/2205.00454

Helling, C., Dehn, M., Woitke, P., & Hauschildt, P. H. 2008a, ApJ, 675, L105, doi: 10.1086/533462

Helling, C., & Fomins, A. 2013, Phil. Trans. R. Soc. A, 371, 20110581, doi: 10.1098/rsta.2011.0581

Helling, C., Gourbin, P., Woitke, P., & Parmentier, V. 2019a, Astronomy & Astrophysics, 626, A133, doi: 10.1051/0004-6361/201834085

Helling, C., Thi, W.-F., Woitke, P., & Fridlund, M. 2006, Astronomy & Astrophysics, 451, L9, doi: 10.1051/0004-6361:20064944

Helling, C., & Woitke, P. 2006, A&A, 455, 325, doi: 10.1051/0004-6361:20054598

Helling, C., Woitke, P., & Thi, W. F. 2008b, Astronomy and Astrophysics, 485, 547, doi: 10.1051/0004-6361:20078220

Helling, C., Ackerman, A., Allard, F., et al. 2008c, Monthly Notices of the Royal Astronomical Society, 391, 1854, doi: 10.1111/j.1365-2966.2008.13991.x

Helling, C., Lee, E., Dobbs-Dixon, I., et al. 2016, MNRAS, 460, 855, doi: 10.1093/mnras/stw662

Helling, C., Iro, N., Corrales, L., et al. 2019b, Astronomy & Astrophysics, 631, A79, doi: 10.1051/0004-6361/201935771

Helling, C., Lewis, D., Samra, D., et al. 2021, A&A, 649, A44, doi: 10.1051/0004-6361/202039911

Helling, C., Samra, D., Lewis, D., et al. 2023, Astronomy and Astrophysics, 671, A122, doi: 10.1051/0004-6361/202243956

Heng, K., Hayek, W., Pont, F., & Sing, D. K. 2012, MNRAS, 420, 20, doi: 10.1111/j.1365-2966.2011.19943.x

Herbst, K., Papaioannou, A., Banjac, S., & Heber, B. 2019a, Astronomy & Astrophysics, 621, A67, doi: 10.1051/0004-6361/201832789

Herbst, K., Grenfell, J. L., Sinnhuber, M., et al. 2019b, Astronomy and Astrophysics, 631, A101, doi: 10.1051/0004-6361/201935888

Herbst, K., Scherer, K., Ferreira, S. E. S., et al. 2020, The Astrophysical Journal Letters, 897, L27, doi: 10.3847/2041-8213/ab9df3

Herbst, K., Baalmann, L. R., Bykov, A., et al. 2022, Space Science Reviews, 218, 29, doi: 10.1007/s11214-022-00894-3

Herbst, K., Bartenschlager, A., Grenfell, J. L., et al. 2023, Impact of Cosmic Rays on Atmospheric Ion Chemistry and Spectral Transmission Features of TRAPPIST-1e, arXiv. http://arxiv.org/abs/2311.04684

Hobbs, R., Rimmer, P. B., Shorttle, O., & Madhusudhan, N. 2021, Monthly Notices of the Royal Astronomical Society, 506, 3186, doi: 10.1093/mnras/stab1839

Hobbs, R., Shorttle, O., Madhusudhan, N., & Rimmer, P. 2019, Monthly Notices of the Royal Astronomical Society, 487, 2242, doi: 10.1093/mnras/stz1333

Hudson, H. S. 1978, Solar Physics, 57, 237, doi: 10.1007/BF00152057

Husser, T. O., Wende-von Berg, S., Dreizler, S., et al. 2013, Astronomy and Astrophysics, 553, A6, doi: 10.1051/0004-6361/201219058

Hõrrak, U., Salm, J., & Tammet, H. 1998, Journal of Geophysical Research: Atmospheres, 103, 13909, doi: 10.1029/97JD01570

Hünsch, M., Weidner, C., & Schmitt, J. H. M. M. 2003, Astronomy & Astrophysics, 402, 571, doi: 10.1051/0004-6361:20030268

Ikezoe, Y., Matsuoka, S., & Takebe, M. 1987, Gas phase ion-molecule reaction rate constants through 1986 (Ion reaction research group of the Mass spectroscopy society of Japan)

Indriolo, N., Fields, B. D., & McCall, B. J. 2009, The Astrophysical Journal, 694, 257, doi: 10.1088/0004-637X/694/1/257

Indriolo, N., Geballe, T. R., Oka, T., & McCall, B. J. 2007, The Astrophysical Journal, 671, 1736, doi: 10.1086/523036

Janson, M., Squicciarini, V., Delorme, P., et al. 2021, Astronomy & Astrophysics, 646, A164, doi: 10.1051/0004-6361/202039683

Jasinski, J. M., Nordheim, T. A., Hasegawa, Y., & Murphy, N. 2020, The Astrophysical Journal Letters, 899, L18, doi: 10.3847/2041-8213/aba7c8

Johnstone, C. P. 2016, Proceedings of the International Astronomical Union, 12, 168, doi: 10.1017/S1743921317003775

Jokinen, T., Sipilä, M., Kontkanen, J., et al. 2018, Science Advances, 4, eaat9744, doi: 10.1126/sciadv.aat9744

Jokipii, J. R. 1971, Reviews of Geophysics, 9, 27, doi: 10.1029/RG009i001p00027

Jorgensen, J. L., Benn, M., Connerney, J. E. P., et al. 2021, Journal of Geophysical Research (Planets), 126, e06509, doi: 10.1029/2020JE006509

Juncher, D., Jørgensen, U. G., & Helling, C. 2017, A&A, 608, A70, doi: 10.1051/0004-6361/201629977

Jurić, M., & Tremaine, S. 2008, The Astrophysical Journal, 686, 603, doi: 10.1086/590047

JWST Transiting Exoplanet Community Early Release Science-Team, Ahrer, E.-M., Alderson, L., et al. 2023, Nature, 614, 649, doi: 10.1038/s41586-022-05269-w

Kallenrode, M. B. 2003, Journal of Physics G Nuclear Physics, 29, 965, doi: 10.1088/0954-3899/29/5/316

Kasting, J. F., Whitmire, D. P., & Reynolds, R. T. 1993, Icarus, 101, 108, doi: 10.1006/icar.1993.1010

Kataria, T., Sing, D. K., Lewis, N. K., et al. 2016, The Astrophysical Journal, 821, 9, doi: 10.3847/0004-637X/821/1/9

Kempton, E. M.-R., Bean, J. L., & Parmentier, V. 2017, ApJL, 845, L20, doi: 10.3847/2041-8213/aa84ac

Kendrew, S., Scheithauer, S., Bouchet, P., et al. 2015, PASP, 127, 623, doi: 10.1086/682255

—. 2016, Proceedings of the SPIE, 9904, 990443, doi: 10.1117/12.2232887

Kiefer, S., Lecoq-Molinos, H., Helling, C., Bangera, N., & Decin, L. 2024, Astronomy & Astrophysics, 682, A150, doi: 10.1051/0004-6361/202347441

Kiefer, S., Bach-Møller, N., Samra, D., et al. submitted 2024, Astronomy & Astrophysics

Knutson, E. O., & Whitby, K. T. 1975, Journal of Aerosol Science, 6, 443, doi: 10.1016/0021-8502(75)90060-9

Kohn, C., Helling, C., Bodker Enghoff, M., et al. 2021, ASTRONOMY & ASTROPHYSICS, 654, A120, doi: 10.1051/0004-6361/202140378

Komacek, T. D., Fauchez, T. J., Wolf, E. T., & Abbot, D. S. 2020, The Astrophysical Journal Letters, 888, L20, doi: 10.3847/2041-8213/ab6200

Komacek, T. D., & Showman, A. P. 2016, The Astrophysical Journal, 821, 16, doi: 10.3847/0004-637X/821/1/16

Komacek, T. D., Showman, A. P., & Tan, X. 2017, ApJ, 835, 198, doi: 10.3847/1538-4357/835/2/198

Konings, T., Baeyens, R., & Decin, L. 2022, Astronomy and Astrophysics, 667, A15, doi: 10.1051/0004-6361/202243436

Kopparapu, R. K., Ramirez, R., Kasting, J. F., et al. 2013, The Astrophysical Journal, 765, 131, doi: 10.1088/0004-637X/765/2/131

Kowalski, A. F. 2024, Living Reviews in Solar Physics, 21, 1, doi: 10.1007/s41116-024-00039-4

Kreidberg, L., Line, M. R., Thorngren, D., Morley, C. V., & Stevenson, K. B. 2018, The Astrophysical Journal Letters, 858, L6, doi: 10.3847/2041-8213/aabfce

Kupka, F., & Montgomery, M. H. 2002, Monthly Notices of the Royal Astronomical Society, 330, L6, doi: 10.1046/j.1365-8711.2002.05268.x

Laakso, L., Gagne, S., Petaja, T., et al. 2007, Atmos. Chem. Phys., 13

Lecoq-Molinos, H., Gobrecht, D., Sindel, J. P., Helling, C., & Decin, L. 2024, Vanadium oxide clusters in substellar atmospheres: A quantum chemical study, arXiv. http://arxiv.org/abs/2401.02784

Lee, E. K. H., Tsai, S.-M., Hammond, M., & Tan, X. 2023, Astronomy & Astrophysics, 672, A110, doi: 10.1051/0004-6361/202245473

Lee, E. K. H., Wood, K., Dobbs-Dixon, I., Rice, A., & Helling, C. 2017, A&A, 601, A22, doi: 10.1051/0004-6361/201629804

Lee, G., Dobbs-Dixon, I., Helling, C., Bognar, K., & Woitke, P. 2016, Astronomy & Astrophysics, 594, A48, doi: 10.1051/0004-6361/201628606

Lee, S.-H., Gordon, H., Yu, H., et al. 2019, Journal of Geophysical Research: Atmospheres, 124, 7098, doi: 10.1029/2018JD029356

Li, G., Qin, G., Hu, Q., & Miao, B. 2012, Advances in Space Research, 49, 1327, doi: 10.1016/j.asr.2012.02.008

Lin, A. S. J., Libby-Roberts, J. E., Alvarado-Montes, J. A., et al. 2023, The Astronomical Journal, 166, 90, doi: 10.3847/1538-3881/ace1ef

Line, M. R., & Parmentier, V. 2016, ApJ, 820, 78, doi: 10.3847/0004-637X/820/1/78

Line, M. R., Vasisht, G., Chen, P., Angerhausen, D., & Yung, Y. L. 2011, ApJ, 738, 32, doi: 10.1088/0004-637X/738/1/32

Lines, S., Mayne, N. J., Boutle, I. A., et al. 2018a, Astronomy & Astrophysics, 615, A97, doi: 10.1051/0004-6361/201732278

Lines, S., Manners, J., Mayne, N. J., et al. 2018b, MNRAS, 481, 194, doi: 10.1093/mnras/sty2275

Linsky, J. L. 2014, Challenges, 5, 351, doi: 10.3390/challe5020351

Linsky, J. L., Fontenla, J., & France, K. 2014, The Astrophysical Journal, 780, 61, doi: 10.1088/0004-637X/780/1/61

Loyd, R. O. P., France, K., Youngblood, A., et al. 2016, The Astrophysical Journal, 824, 102, doi: 10.3847/0004-637X/824/2/102

—. 2018, The Astrophysical Journal, 867, 71, doi: 10.3847/1538-4357/aae2bd

Lunine, J. I., Hubbard, W. B., & Marley, M. S. 1986, The Astrophysical Journal, 310, 238, doi: 10.1086/164678

Maciel, W. J. 2016, Introduction to Stellar Structure, doi: 10.1007/978-3-319-16142-6

Manion, J. A., Huie, R. E., Levin, R. D., et al. 2013, NIST Standard Reference Database 17

Maor, E. 2013, To Infinity and Beyond: A Cultural History of the Infinite (Springer Science & Business Media)

Marley, M. S., Gelino, C., Stephens, D., Lunine, J. I., & Freedman, R. 1999, The Astrophysical Journal, 513, 879

Marsh, N. D., & Svensmark, H. 2000, Physical Review Letters, 85, 5004, doi: 10.1103/PhysRevLett.85.5004

Massoudifarid, M., Piri, A., & Hwang, J. 2022, Scientific Reports, 12, 6546, doi: 10.1038/s41598-022-10440-4

Maurchev, E. A., Shlyk, N. S., Dmitriev, A. V., et al. 2024, Atmosphere, 15, 151, doi: 10.3390/atmos15020151

Mayne, N. J., Baraffe, I., Acreman, D. M., et al. 2014, Astronomy & Astrophysics, 561, A1, doi: 10.1051/0004-6361/201322174

Mazziotta, M., Luque, P. D. L. T., Di Venere, L., et al. 2020, Physical Review D, 101, 083011, doi: 10.1103/PhysRevD.101.083011

McKay, C. P., Pollack, J. B., & Courtin, R. 1991, Science, 253, 1118, doi: 10.1126/science.11538492

Meidinger, N. 2018, Contributions of the Astronomical Observatory Skalnate Pleso, 48, 498, doi: 10.48550/arXiv.1702.01079

Merikanto, J., Spracklen, D. V., Mann, G. W., Pickering, S. J., & Carslaw, K. S. 2009, Atmospheric Chemistry and Physics, 9, 8601, doi: 10.5194/acp-9-8601-2009

Mesquita, A. L., Rodgers-Lee, D., & Vidotto, A. A. 2021a, Monthly Notices of the Royal Astronomical Society, 505, 1817, doi: 10.1093/mnras/stab1483

Mesquita, A. L., Rodgers-Lee, D., Vidotto, A. A., Atri, D., & Wood, B. E. 2021b, Monthly Notices of the Royal Astronomical Society, 509, 2091, doi: 10.1093/mnras/stab3131

Mignon, L., Meunier, N., Delfosse, X., et al. 2023, Characterisation of stellar activity of M dwarfs. I. Long-timescale variability in a large sample and detection of new cycles, arXiv, doi: 10.48550/arXiv.2303.03998

Miguel, Y., & Kaltenegger, L. 2013, The Astrophysical Journal, 780, doi: 10.1088/0004-637X/780/2/166

Mironova, I. A., Aplin, K. L., Arnold, F., et al. 2015, Space Science Reviews, 194, 1, doi: 10.1007/s11214-015-0185-4

Mishra, L., Alibert, Y., Leleu, A., et al. 2021, Astronomy and Astrophysics, 656, A74, doi: 10.1051/0004-6361/202140761

Mishra, L., Alibert, Y., Udry, S., & Mordasini, C. 2023a, Astronomy & Astrophysics, 670, A69, doi: 10.1051/0004-6361/202244705

—. 2023b, Astronomy & Astrophysics, 670, A68, doi: 10.1051/0004-6361/202243751

Mitra-Kraev, U., Harra, L. K., Guedel, M., et al. 2004, arXiv:astro-ph/0410592, doi: 10.1051/0004-6361:20041201

Mollière, P., Wardenier, J. P., Boekel, R. v., et al. 2019, Astronomy & Astrophysics, 627, A67, doi: 10.1051/0004-6361/201935470

Mori, M. 1997, The Astrophysical Journal, 478, 225, doi: 10.1086/303785

Morley, C. V., Fortney, J. J., Marley, M. S., et al. 2012, ApJ, 756, 172, doi: 10.1088/0004-637X/756/2/172

Moses, J. I., Visscher, C., Fortney, J. J., et al. 2011, The Astrophysical Journal, 737, 15, doi: 10.1088/0004-637X/737/1/15

Motzkus, C., Vaslin-Reimann, S., Mace, T., et al. 2013, Journal of Nanoparticle Research, 15, 1919, doi: 10.1007/s11051-013-1919-4

Murray-Clay, R. A., Chiang, E. I., & Murray, N. 2009, The Astrophysical Journal, 693, 23, doi: 10.1088/0004-637X/693/1/23

Nandra, K., Barret, D., Barcons, X., et al. 2013, The Hot and Energetic Universe: A White Paper presenting the science theme motivating the Athena+ mission, doi: 10.48550/arXiv.1306.2307

Nandy, D., Martens, P. C. H., Obridko, V., Dash, S., & Georgieva, K. 2021, Progress in Earth and Planetary Science, 8, 40, doi: 10.1186/s40645-021-00430-x

Nikolov, N., Sing, D. K., Gibson, N. P., et al. 2016, ApJ, 832, 191, doi: 10.3847/0004-637X/832/2/191

Obridko, V. N., Ragulskaya, M. V., & Khramova, E. G. 2020, Journal of Atmospheric and Solar-Terrestrial Physics, 208, 105395, doi: 10.1016/j.jastp.2020.105395

Ohno, K., Zhang, X., Tazaki, R., & Okuzumi, S. 2021, The Astrophysical Journal, 912, 37

Ormel, C. W., & Min, M. 2019, A&A, 622, A121, doi: 10.1051/0004-6361/201833678

Ortenzi, G., Noack, L., Sohl, F., et al. 2020, Scientific Reports, 10, 10907, doi: 10.1038/s41598-020-67751-7

Oskinova, L. M. 2016, Advances in Space Research, 58, 739, doi: 10.1016/j.asr.2016.06.030

Oskinova, L. M., Feldmeier, A., & Hamann, W.-R. 2006, Monthly Notices of the Royal Astronomical Society, 372, 313, doi: 10.1111/j.1365-2966.2006.10858.x

Parker, E. N. 1965, Planetary and Space Science, 13, 9, doi: 10.1016/0032-0633(65)90131-5

Parmentier, V., Fortney, J. J., Showman, A. P., Morley, C., & Marley, M. S. 2016, ApJ, 828, 22, doi: 10.3847/0004-637X/828/1/22

Parmentier, V., Showman, A. P., & Fortney, J. J. 2021, MNRAS, 501, 78, doi: 10.1093/mnras/staa3418

Parmentier, V., Showman, A. P., & Lian, Y. 2013, A&A, 558, A91, doi: 10.1051/0004-6361/201321132

Pascucci, I., Testi, L., Herczeg, G. J., et al. 2016, ApJ, 831, 125, doi: 10.3847/0004-637X/831/2/125

Patrignani, C., Agashe, K., Aielli, G., et al. 2016, Chinese Physics C, 40, doi: 10.1088/1674-1137/40/10/100001

Pelletier, S., Benneke, B., Ali-Dib, M., et al. 2023, Nature, 1, doi: 10.1038/s41586-023-06134-0

Perez-Becker, D., & Showman, A. P. 2013, The Astrophysical Journal, 776, 134, doi: 10.1088/0004-637X/776/2/134

Peron, G., Aharonian, F., Casanova, S., Yang, R., & Zanin, R. 2021, The Astrophysical Journal Letters, 907, L11, doi: 10.3847/2041-8213/abcaa9

Pontoppidan, K. M., Barrientes, J., Blome, C., et al. 2022, The Astrophysical Journal Letters, 936, L14, doi: 10.3847/2041-8213/ac8a4e

Potgieter, M. S. 2013, Living Reviews in Solar Physics, 10, 3, doi: 10.12942/lrsp-2013-3

Powell, D., Louden, T., Kreidberg, L., et al. 2019, ApJ, 887, 170, doi: 10.3847/1538-4357/ab55d9

Powell, D., Zhang, X., Gao, P., & Parmentier, V. 2018, ApJ, 860, 18, doi: 10.3847/1538-4357/aac215

Rab, C., Güdel, M., Padovani, M., et al. 2017, Astronomy & Astrophysics, 603, A96, doi: 10.1051/0004-6361/201630241

Rages, K., & Pollack, J. B. 1992, Icarus, 99, 289

Reames, D. 2020, Solar Energetic Particles (Second Edition)

Reames, D. V. 2013, Space Science Reviews, 175, 53

Reep, J. W., & Knizhnik, K. J. 2019, The Astrophysical Journal, 874, 157, doi: 10.3847/1538-4357/ab0ae7

Ridgway, R. J., Zamyatina, M., Mayne, N. J., et al. 2023, Monthly Notices of the Royal Astronomical Society, 518, 2472, doi: 10.1093/mnras/stac3105

Rimmer, P. B., & Helling, C. 2013, The Astrophysical Journal, 774, 108, doi: 10.1088/0004-637X/774/2/108

—. 2016a, The Astrophysical Journal Supplement Series, 224, 9, doi: 10.3847/0067-0049/224/1/9

—. 2016b, The Astrophysical Journal Supplement Series, 224, 9, doi: 10.3847/0067-0049/224/1/9

Rimmer, P. B., Herbst, E., Morata, O., & Roueff, E. 2012, Astronomy & Astrophysics, 537, A7, doi: 10.1051/0004-6361/201117048

Rimmer, P. B., & Rugheimer, S. 2019, Icarus, 329, 124, doi: 10.1016/j.icarus.2019.02.020

Robbins-Blanch, N., Kataria, T., Batalha, N. E., & Adams, D. J. 2022, ApJ, 930, 93, doi: 10.3847/1538-4357/ac658c

Rodgers-Lee, D., Taylor, A. M., Vidotto, A. A., & Downes, T. P. 2021a, Monthly Notices of the Royal Astronomical Society, 504, 1519, doi: 10.1093/mnras/stab935

Rodgers-Lee, D., Vidotto, A. A., & Mesquita, A. L. 2021b, Monthly Notices of the Royal Astronomical Society, 508, 4696, doi: 10.1093/mnras/stab2788

Rodgers-Lee, D., Vidotto, A. A., Taylor, A. M., Rimmer, P. B., & Downes, T. P. 2020, Monthly Notices of the Royal Astronomical Society, 499, 2124, doi: 10.1093/mnras/staa2737

Rodgers-Lee, D., Rimmer, P. B., Vidotto, A. A., et al. 2023, Monthly Notices of the Royal Astronomical Society, 521, 5880, doi: 10.1093/mnras/stad900

Rodríguez-Barrera, M. I., Helling, C., & Wood, K. 2018, Astronomy & Astrophysics, 618, A107, doi: 10.1051/0004-6361/201832685

Roman, M., & Rauscher, E. 2017, ApJ, 850, 17, doi: 10.3847/1538-4357/aa8ee4

Roman, M. T., Kempton, E. M.-R., Rauscher, E., et al. 2021, ApJ, 908, 101, doi: 10.3847/1538-4357/abd549

Romani, P. N., & Atreya, S. K. 1988, Icarus, 74, 424

Rowe, J. F., Matthews, J. M., Seager, S., et al. 2008, The Astrophysical Journal, 689, 1345, doi: 10.1086/591835

Rustamkulov, Z., Sing, D. K., Mukherjee, S., et al. 2023, Nature, 614, 659, doi: 10.1038/s41586-022-05677-y

Rycroft, M. J., & Harrison, R. G. 2012, Space Science Reviews, 168, 363, doi: 10.1007/s11214-011-9830-8

Sacchi, M., & Tamtögl, A. 2023, Advances in Physics: X, 8, 2134051, doi: 10.1080/23746149.2022.2134051

Sadovski, A. M., Struminsky, A. B., & Belov, A. 2018, Astronomy Letters, 44, 324, doi: 10.1134/S1063773718040072

Sagan, C., Thompson, W. R., & Khare, B. N. 1992, Accounts of Chemical Research, 25, 286

Samra, D., Helling, C., Chubb, K., et al. 2023, Astronomy & Astrophysics, 669, A142, doi: 10.1051/0004-6361/202244939

Sander, S., Abbatt, J., Barker, J., et al. 2011, Chemical Kinetics and Photochemical Data for Use in Atmospheric Studies, Evaluation No. 17

Sarangi, B., Aggarwal, S. G., & Gupta, P. K. 2015, Aerosol and Air Quality Research, 15, 166, doi: 10.4209/aaqr.2013.12.0350

Savel, A. B., Kempton, E. M.-R., Malik, M., et al. 2022, ApJ, 926, 85, doi: 10.3847/1538-4357/ac423f

Scalo, J., Kaltenegger, L., Segura, A. G., et al. 2007, Astrobiology, 7, 85, doi: 10.1089/ast.2006.0125

Scherer, K., van der Schyff, A., Bomans, D., et al. 2015, Astronomy & Astrophysics, 576, A97, doi: 10.1051/0004-6361/201425091

Scheucher, M., Herbst, K., Schmidt, V., et al. 2020, The Astrophysical Journal, 893, 12, doi: 10.3847/1538-4357/ab7b74

Schneider, A. D., Baeyens, R., & Kiefer, S. 2022a, gcm_toolkit, Zenodo, doi: 10.5281/zenodo.7116787

Schneider, A. D., Carone, L., Decin, L., et al. 2022b, A&A, 664, A56, doi: 10.1051/0004-6361/202142728

Seager, S., & Sasselov, D. 2000, The Astrophysical Journal, 537, 916

Segura, A., Walkowicz, L. M., Meadows, V., Kasting, J., & Hawley, S. 2010, Astrobiology, 10, 751, doi: 10.1089/ast.2009.0376

Selsis, F., Kasting, J. F., Levrard, B., et al. 2007, Astronomy and Astrophysics, 476, 1373, doi: 10.1051/0004-6361:20078091

Seward, F. D., Forman, W. R., Giacconi, R., et al. 1979, The Astrophysical Journal, 234, L55, doi: 10.1086/183108

Showman, A. P., Fortney, J. J., Lian, Y., et al. 2009, The Astrophysical Journal, 699, 564, doi: 10.1088/0004-637X/699/1/564

Showman, A. P., & Guillot, T. 2002, A&A, 385, 166, doi: 10.1051/0004-6361:20020101

Shulyak, D., Lara, L. M., Rengel, M., & Nèmec, N.-E. 2020, Astronomy & Astrophysics, 639, A48, doi: 10.1051/0004-6361/201937210

Sindel, J. P., Gobrecht, D., Helling, C., & Decin, L. 2022, Astronomy & Astrophysics, 668, A35, doi: 10.1051/0004-6361/202243306

Sing, D. K., Fortney, J. J., Nikolov, N., et al. 2016, Nature, 529, 59, doi: 10.1038/nature16068

Sinnhuber, M., Nieder, H., & Wieters, N. 2012, Surveys in Geophysics, 33, 1281, doi: 10.1007/s10712-012-9201-3

Skumanich, A. 1972, Astrophysical Journal, vol. 171, p. 565, 171, 565

Smith, R. K., Brickhouse, N. S., Liedahl, D. A., & Raymond, J. C. 2001, The Astrophysical Journal, 556, L91, doi: 10.1086/322992

Snodgrass, C., & Jones, G. H. 2019, Nature Communications, 10, 5418, doi: 10.1038/s41467-019-13470-1

Sromovsky, L., Fry, P., & Kim, J. H. 2011, Icarus, 215, 292

Steinrueck, M. E., Koskinen, T., Lavvas, P., et al. 2023, ApJ, 951, 117, doi: 10.3847/1538-4357/acd4bb

Stevenson, K. B., Lewis, N. K., Bean, J. L., et al. 2016, Publications of the Astronomical Society of the Pacific, 128, 094401, doi: 10.1088/1538-3873/128/967/094401

Strong, A. W., Moskalenko, I. V., & Ptuskin, V. S. 2007, Annual Review of Nuclear and Particle Science, 57, 285, doi: 10.1146/annurev.nucl.57.090506.123011

Svensmark, H. 2006, Astronomische Nachrichten, 327, 871, doi: 10.1002/asna.200610651

Svensmark, H., Enghoff, M. B., & Pedersen, J. O. P. 2013, Physics Letters A, 377, 2343, doi: 10.1016/j.physleta.2013.07.004

Svensmark, H., Enghoff, M. B., Shaviv, N. J., & Svensmark, J. 2017, Nature Communications, 8, 2199, doi: 10.1038/s41467-017-02082-2

Svensmark, H., & Friis-Christensen, E. 1997, Journal of Atmospheric and Solar-Terrestrial Physics, 59, 1225, doi: 10.1016/S1364-6826(97)00001-1

Svensmark, H., Svensmark, J., Enghoff, M. B., & Shaviv, N. J. 2021, Scientific Reports, 11, 19668, doi: 10.1038/s41598-021-99033-1

Svensmark, J., Shaviv, N. J., Enghoff, M. B., & Svensmark, H. 2020, Earth and Space Science, 7, e2020EA001142, doi: 10.1029/2020EA001142

Tan, X., & Showman, A. P. 2021, MNRAS, 502, 2198, doi: 10.1093/mnras/stab097

Tilley, M. A., Segura, A., Meadows, V., Hawley, S., & Davenport, J. 2019, Astrobiology, 19, 64, doi: 10.1089/ast.2017.1794

Tsai, S.-M., Lyons, J. R., Grosheintz, L., et al. 2017, The Astrophysical Journal Supplement Series, 228, 20, doi: 10.3847/1538-4365/228/2/20

Tsai, S.-M., Lee, E. K. H., Powell, D., et al. 2023, Nature, 617, 483, doi: 10.1038/s41586-023-05902-2

TSI Incorporated. 2005, Model 3076 Constant output atomizer instruction manual, TSI Incorporated Shoreview, MN, USA

—. 2009, Model 3080 Electrostatic Classifiers Operations and service manual, TSI Incorporated Shoreview, MN, USA

—. 2012, Aerosol statistics lognormal distributions and dN/DlogDp, https://tsi.com/getmedia/1621329b-f410-4dce-992b-e21e1584481a/PR-001-RevA_Aerosol-Statistics-AppNote?ext=.pdf.

Turbet, M., Bolmont, E., Chaverot, G., et al. 2021, Nature, 598, 276, doi: 10.1038/s41586-021-03873-w

Venot, O., Rocchetto, M., Carl, S., Hashim, A. R., & Decin, L. 2016, The Astrophysical Journal, 830, 77, doi: 10.3847/0004-637X/830/2/77

Vida, K., Kővári, Z., Pál, A., Oláh, K., & Kriskovics, L. 2017, Frequent flaring in the TRAPPIST-1 system - unsuited for life?, doi: 10.3847/1538-4357/aa6f05

Vidotto, A. A., Gregory, S. G., Jardine, M., et al. 2014, Monthly Notices of the Royal Astronomical Society, 441, 2361, doi: 10.1093/mnras/stu728

Wagner, R., Yan, C., Lehtipalo, K., et al. 2017, Atmospheric Chemistry and Physics, 17, 15181, doi: 10.5194/acp-17-15181-2017

Wakeford, H. R., & Sing, D. K. 2015, A&A, 573, A122, doi: 10.1051/0004-6361/201424207

Wakeford, H. R., Sing, D. K., Deming, D., et al. 2018, ApJ, 155, 29, doi: 10.3847/1538-3881/aa9e4e

Wakelam, V., Herbst, E., Loison, J. C., et al. 2012, The Astrophysical Journal Supplement Series, 199, 21, doi: 10.1088/0067-0049/199/1/21

Webber, M. W., Lewis, N. K., Marley, M., et al. 2015, ApJ, 804, 94, doi: 10.1088/0004-637X/804/2/94

Weiss, L. M., Millholland, S. C., Petigura, E. A., et al. 2022, Architectures of Compact Multi-planet Systems: Diversity and Uniformity, arXiv, doi: 10.48550/arXiv.2203.10076

West, A. A., Hawley, S. L., Walkowicz, L. M., et al. 2004, The Astronomical Journal, 128, 426, doi: 10.1086/421364

Wiedensohler, A. 1988, Journal of Aerosol Science, 19, 387, doi: 10.1016/0021-8502(88)90278-9

Wiedensohler, A., Lütkemeier, E., Feldpausch, M., & Helsper, C. 1986, Journal of Aerosol Science, 17, 413, doi: 10.1016/0021-8502(86)90118-7

Wild, J., Smerd, S., & Weiss, A. 1963, Annual Review of Astronomy and Astrophysics, 1, 291

Witte, S., Helling, C., Barman, T., Heidrich, N., & Hauschildt, P. H. 2011, A&A, 529, A44, doi: 10.1051/0004-6361/201014105

Woitke, P., & Helling, C. 2003, Astronomy and Astrophysics, 399, 297, doi: 10.1051/0004-6361:20021734

Woitke, P., Helling, C., & Gunn, O. 2020, A&A, 634, A23, doi: 10.1051/0004-6361/201936281

Woitke, P., Helling, C., Hunter, G. H., et al. 2018, A&A, 614, A1, doi: 10.1051/0004-6361/201732193

Wolf, E., Kopparapu, R., Airapetian, V., et al. 2019, Astro2020: Decadal Survey on Astronomy and Astrophysics, 2020, 177, doi: 10.48550/arXiv.1903.05012

Wong, I., Chachan, Y., Knutson, H. A., et al. 2022, The Astronomical Journal, 164, 30, doi: 10.3847/1538-3881/ac7234

Wong, M. L., Fan, S., Gao, P., et al. 2017, Icarus, 287, 110

Yang, J., Boué, G., Fabrycky, D. C., & Abbot, D. S. 2014, The Astrophysical Journal Letters, 787, L2, doi: 10.1088/2041-8205/787/1/L2

Yee, S. W., Winn, J. N., & Hartman, J. D. 2021, The Astronomical Journal, 162, 240, doi: 10.3847/1538-3881/ac2958

Yelle, R. V. 2004, Icarus, 170, 167, doi: 10.1016/j.icarus.2004.02.008

Youngblood, A., France, K., Loyd, R. O. P., et al. 2016, The Astrophysical Journal, 824, 101, doi: 10.3847/0004-637X/824/2/101

—. 2017, The Astrophysical Journal, 843, 31, doi: 10.3847/1538-4357/aa76dd

Zank, G. P., Rice, W. K. M., & Wu, C. C. 2000, Journal of Geophysical Research, 105, 25079, doi: 10.1029/1999JA000455

Zhou, G., & Huang, L. 2021, Molecular Simulation, 47, 925, doi: 10.1080/08927022.2020.1786086

"*Good job, me!*"
– Nanna Bach-Møller, 2024